

UNIVERSITÉ DU QUÉBEC

**MÉMOIRE
PRÉSENTÉ À
L'UNIVERSITÉ DU QUÉBEC À CHICOUTIMI
COMME EXIGENCE PARTIELLE
DE LA MAÎTRISE EN INGÉNIERIE**

**Par
FARANAK ARIANPOUR**

**Water and ice-repellent properties of nanocomposite coatings
based on silicone rubber**

**Propriétés hydrophobes et glaciophobes de revêtements
nanocomposites à base de silicone**

December 2010

Abstract

In cold-climate countries such as Canada, Norway, Russia, Finland, the USA, China and Japan, ice accumulation on power network equipment may cause serious problems resulting in power outages with socioeconomical consequences. This situation is caused roughly by mechanical line failures or insulator flashovers, involving several complex phenomena.

Coating the surface of structures exposed to atmospheric icing with anti-icing materials can be an effective way to protect them against ice and snow adhesion and accretion. Coatings with water contact angle greater than 150° have been the subject of great interest during recent years. Such surfaces are called super-hydrophobic and are prepared by combining appropriate surface roughness with low surface energy.

In the present work, flat and micro-/nano-rough water-repellent coatings based on silicone rubber incorporated with nanopowders of carbon-black, titania and ceria as dopants have been prepared and investigated. Such water-repellent coatings are potential candidates for protecting high-voltage equipment such as conductors and insulators.

The water-repellent properties of the coatings were evaluated showing good incorporation of the dopant particles into silicone rubber. The anti-icing behaviour of the different coatings was studied under atmospheric icing conditions. Rough super-hydrophobic coatings prepared with TiO_2 and CeO_2 nanoparticles of different dielectric constants (TiO_2 : ~ 80 , CeO_2 : ~ 60) resulted in reducing the ice adhesion strength of at least ~ 7 times compared to a mirror-polished aluminum sample and ~ 9 times compared to an as-received aluminum sample.

Freezing behaviour of small water droplets was investigated on such nanostructured composite surfaces and compared with that on flat surfaces. At $-15\text{ }^{\circ}\text{C}$, small water droplets were observed to freeze on polished Al after approximately 5 s, while their freezing was delayed to $\sim 12\text{-}13$ min on super-hydrophobic nanocomposite surfaces. This is explained by the insulating properties of the rough surfaces which entrap a significant amount of air into their structure. Therefore, the coatings prepared show promise for industrial applications on high-voltage equipment, including insulators, since they can reduce ice accumulation, while also reducing the risk of flashover on overhead high-tension insulators.

Résumé

Dans les pays à climat froid comme le Canada, la Norvège, la Russie, la Finlande, les États-Unis, la Chine et le Japon, l'accumulation de glace sur les équipements des réseaux électriques peut causer de sérieux problèmes résultant en des pannes d'électricité avec des conséquences socioéconomiques parfois désastreuses.

Le revêtement de la surface des structures exposées au givrage atmosphérique avec des matériaux antigivre peut être un moyen efficace de les protéger contre l'adhésion et l'accumulation de glace ou de neige. Les revêtements ayant un angle de contact de l'eau supérieur à 150° ont fait l'objet de nombreuses études au cours de ces dernières années. Ces surfaces sont appelées superhydrophobe et sont préparées en combinant une rugosité de surface appropriée avec une faible énergie de surface.

Dans ce travail de recherche, on a élaboré et étudié des revêtements hydrophobes plats et avec une micro-/nano-rugosité à base de caoutchouc de silicone où de la nanopoudre de noir de carbone, de dioxyde de titane et d'oxyde de cérium (« dopants ») avait été intégrée. Ces revêtements hydrophobes sont des candidats potentiels pour la protection d'équipements haute tension tels que les conducteurs et les isolants, contre les accumulations de glace ou de neige.

Les propriétés hydrophobes des revêtements ont été évaluées et montrent une bonne incorporation des particules ajoutées au caoutchouc de silicone. Le comportement antigivre des différents revêtements a été étudié dans des conditions de givrage atmosphérique. Les revêtements superhydrophobes préparés avec des nanoparticules de TiO_2 et CeO_2 de constantes diélectriques différentes (TiO_2 : ~ 80 , CeO_2 : ~ 60) ont permis de réduire la force d'adhérence de la glace par au moins sept fois par rapport à un

échantillon d'aluminium poli miroir et environ neuf fois par rapport à un échantillon d'aluminium brut.

Le comportement de petites gouttelettes d'eau au cours de leur congélation a été étudié sur des surfaces nanostructurées composites et sur des surfaces planes. À environ -15 °C, de petites gouttelettes d'eau ont gelé sur de l'Al poli après environ cinq secondes, ce qui a pris ~12-13 minutes sur des surfaces nanocomposite superhydrophobes. Cela s'explique par les propriétés isolantes des surfaces rugueuses qui piègent une quantité importante d'air dans leur structure. Par conséquent, les revêtements ainsi préparés sont prometteurs pour des applications industrielles sur des équipements haute tension, y compris les isolateurs, car ils peuvent en réduire l'accumulation de glace tout en diminuant le risque de leur contournement électrique.

Acknowledgments

This Masters' research was carried out within the framework of the Industrial Chair on Atmospheric Icing of Power Network Equipment (CIGELE) and the Canada Research Chair on Engineering of Power Network Atmospheric Icing (INGIVRE) at University of Quebec in Chicoutimi (UQAC).

I would like to use this window of occasion to thank those who helped me to complete this thesis. In the first place, I would like to thank wholeheartedly, my Director, **Prof. M. Farzaneh**, for his support, supervision, guidance, encouragement and patience, as well as deepest appreciation to Prof. Farzaneh's family for their warm welcome and kind hospitality in Chicoutimi. He behaved with me like father. It is an honor for me to earn my graduation under his supervision. Prof. Farzaneh is, without question, an expert in his field and his duty. I would also like to express my deepest gratitude to my co-director, Dr. Sergei Kulinich, for his excellent guidance and help during my project. Thank you to my colleagues, technicians and professionals, Pierre Camirand, Denis Masson and Xavier Bouchard, in CIGELE for their constant companionship and assistance.

I would like to express my warmest and deepest appreciation to my dear parents, sister and brothers who helped and encouraged me during in my studies, especially my father and my brother *Dr. G. Aryanpour* for teaching me determination. They have always stood by me and showed me how to reach my aims. I owe them everything. Last but not least, I would like to express my most profound gratitude to my

beloved husband, Shahram, for his true love and patience. His valuable and precious advice was most important to complete my thesis. I wish the best you and look forward to more great moments in the future with you.

Table of Contents

Abstract.....	ii
Résumé	iv
Acknowledgments	vi
Table of Contents	viii
List of Figures.....	xi
List of Tables	xiv
List of Symbols and Abbreviations	xv
CHAPTER 1 INTRODUCTION.....	1
1.1 The Problem of Icing -----	2
1.2 Current Solutions-----	3
1.3 Main Objectives -----	4
1.4 Methodology-----	6
1.5 Statement of Originality-----	8
1.6 The Outline of Thesis-----	9
CHAPTER 2 BACKGROUND AND LITERATURE REVIEW.....	12
2.1 Atmospheric Icing and Types of Ice-----	14
2.2 Ice Adhesion Mechanisms -----	19
2.3 Brief Review on Hydrophobic and Super-hydrophobic Properties-----	23

2.3.1 Hydrophobicity and Contact Angle	23
2.3.2 Super-hydrophobicity and Roughness	26
2.4 Review of Nanoparticles incorporated in Silicone Rubber	34

CHAPTER 3 EXPERIMENTAL SETUP AND TEST PROCEDURES39

3.1 Process of Coatings' Preparation	40
3.1.1 Substrate Cleaning	41
3.1.2 Producing Micro-/Nano-Rough Substrates.....	42
3.1.3 Preparation of Solution	43
3.1.4 Coating of the Samples	43
3.2 Sample Analysis and Characterization	45
3.2.1 Morphological Characterization	45
3.2.2 Wettability Tests	47
3.2.2.1 Contact Angle Measurement at Room Temperature	47
3.2.2.2 Contact Angle (CA) Measurement at Low Temperature.....	49
3.2.2.3 Ice Adhesion Test	50

CHAPTER 4 EXPERIMENTAL RESULTS AND DISCUSSION: HYDROPHOBIC AND SUPER-HYDROPHOBIC PROPERTIES OF FLAT AND ROUGH SAMPLES WITH COATINGS ALUMINUM SUBSTRATE53

4.1 Water Droplet Contact Angle on Flat Al Substrates	54
4.1.1 Carbon-Black Nanoparticle-Incorporated RTV SR Coatings	54
4.1.2 TiO ₂ Nanoparticles-Incorporated RTV SR Coatings.....	57
4.2 Water Droplet Contact Angle on Rough Aluminum Substrates	58
4.2.1 TiO ₂ Nanoparticles-Incorporated RTV SR Coatings.....	59
4.2.2 Carbon-Black Nanoparticles-Incorporated RTV SR Coatings	61
4.2.3 TiO ₂ Nanoparticles-Incorporated RTV SR Coatings	63
4.2.4 CeO ₂ Nanoparticles-Incorporated RTV SR Coatings	65

4.3 Surface Characterization-----	67
4.3.1 Scanning Electron Microscopy (SEM)	67
4.4 Summary and Conclusions -----	72
CHAPTER 5 EXPERIMENTAL RESULTS AND DISCUSSION: ICE ADHESION STRENGTH ON SAMPLE SURFACE	73
5.1 Ice Adhesion Strength of Flat Aluminum Substrate Coated with RTV SR Incorporated with Carbon-Black (CB) Nanoparticles -----	74
5.2 Ice Adhesion Strength on Rough Al Substrate Coated with RTV SR Incorporated with TiO ₂ or CeO ₂ Nanoparticles-----	76
5.3 Adhesion Reduction Factor (<i>ARF</i>) Values of the Coated Samples -----	78
5.4 Contact Angle as a Function of Icing/de-Icing Cycles -----	82
5.5 Summary and Conclusions-----	84
CHAPTER 6 EXPERIMENTAL RESULTS AND DISCUSSION: STABILITY OF SAMPLES IMMERSSED IN DI- WATER AND FREEZING OF WATER DROPLETS ON SAMPLE SURFACES	86
6.1 Stability of Samples Immersed in DI Water -----	87
6.2 Freezing of Water Droplets on Sample Surfaces-----	90
6.3 Summary and Conclusions-----	95
CHAPTER 7 CONCLUSIONS AND RECOMMENDATION FOR FUTURE WORKS	97
7.1 Conclusions -----	98
7.2 Recommendations for Future Work-----	101
References	103

List of Figures

Figure 2.1: (a) Soft rime, (b) hard rime ice on ridge-top vegetation, Sierra Nevada crest, (c) glaze.....	17
Figure 2.2: Schematic of liquid droplet in contact with a smooth solid surface (contact angle, θ_0).....	24
Figure 2.3: A schematic diagram of hydrophobic surface (left), and hydrophilic surface (right).....	26
Figure 2.4: Montage of some examples from nature: (a) Lotus effect [33], and (b) pond skater walking on water [54].....	27
Figure 2.5: SEM micrographs (shown at three magnifications) of Lotus (<i>Nelumbo nucifera</i>) leaf surface which consists of microstructure formed by papillose epidermal cells covered with 3-D epicuticular wax tubules on surface, which create nanostructure [45].....	28
Figure 2.6: Schematic and wetting of the four different surfaces. The largest contact area between the droplet and the surface is given in flat and microstructured surfaces, but is reduced in nanostructured surfaces and is minimized in hierarchical structured surfaces.....	29
Figure 2.7: (a) Contact angle for rough surface (θ) (Wenzel regime) as a function of the roughness factor (R_f) for various contact angles of the smooth surface (θ_0), and (b) schematic of square-based hemispherically-topped pyramidal asperities with complete packing.....	31
Figure 2.8: Schematics of configurations described by the (a) Wenzel equation for the homogeneous interface (Eq. (6)), (b) Cassie–Baxter equation for the composite interface with air pockets (Eq. (9)), and (c) the Cassie equation for the homogeneous interface (Eq. (10)).....	33
Figure 3.1: (a) The spin-coater (model WS-400B-6NPP, Laurell Technologies Corporation), (b) steps of coating preparation, (1) deposit solution, (2) spreading (low speed spin), (3) high speed spin.....	44
Figure 3.2: Scheme of preparation of nano-powder incorporated RTV SR coatings on rough substrates.....	45
Figure 3.3: Kruss DSA100 contact-angle goniometer.....	48
Figure 3.4: Measuring the advancing and receding contact angles on a sample with (a) a low hysteresis (static CA), and (b) a high hysteresis (advancing (θ_A) and receding (θ_R) CAs.....	48
Figure 3.5: Contact-angle goniometer and cooling unit for measuring CA at low temperature (centre), enlarged Peltier device (left) and cooling/heating system (right).....	49
Figure 3.6: (a) Centrifuge system. (b) sample with coating (1) in centrifuge set-up evaluating ice adhesion strength. (1) sample, (2) aluminum beam, (3) counter-weight.	51
Figure 3.7: (a) Top view of atmospheric icing wind tunnel used and (b) a view of ice accumulation procedure on coated samples in wind tunnel (b).....	52

Figure 4.1: (a) Water drop on pure (non-doped) RTV SR coating, (b) water drop on RTV SR coating with 6 vol. % of carbon-black nanoparticles incorporated, (c) contact angle vs. vol. % of carbon-black incorporated into coatings	55
Figure 4.2: AFM surface images of RTV SR coatings doped with 0 (a), 6 (b), 12 (c), and 18 vol. % (d) of carbon-black. Root-mean-square roughness (R_q) values are 128.2 (a), 178.11 (b), 261.93 (c), and 295.81 nm (d).....	56
Figure 4.3: Contact angle (white) and CAH (black) as a function of TiO_2 concentration in coatings prepared by spin-coatings RTV SR/hexane ratio (1:3 v/v) suspension on flat aluminum.....	58
Figure 4.4: Contact angle of samples prepared by spin-coating RTV SR/hexane (1:1 v/v) suspension with 2 wt. % of TiO_2 nanoparticles incorporated as a function of etching time of the substrate used.....	60
Figure 4.5: Contact angle hysteresis of coatings prepared (1:1 v/v) RTV SR/hexane solution with 2 wt. % of TiO_2 nanoparticles incorporated as a function of etching time of the substrate (Al alloy in diluted HCl).....	60
Figure 4.6: (a) Water contact angle (CA) and (b) water contact angle hysteresis (CAH) of coating prepared by spin-coating hexane dilution of RTV SR (1:4) with 3 wt.% carbon black nanoparticles incorporated, (c) contact angle (white) and CAH (black) as a function of different concentration of RTV SR with 3 wt.% of carbon black nanoparticles incorporated.....	61
Figure 4.7: (a) Water contact angle (CA) and (b) water contact angle hysteresis (CAH) of coating spin-coated from hexane dilution of RTV SR (1:4) with 1.5 wt.% carbon black nanoparticles incorporated, (c) contact angle (white) and CAH (gray) as a function of hexane dilution of RTV SR with 1.5 wt.% of carbon black nanoparticles incorporated.....	62
Figure 4.8: (a) Water contact angle (CA) and (b) water contact angle hysteresis (CAH) of coating prepared by spin-coating hexane dilution of RTV SR (1:4) with 1 wt.% TiO_2 nanoparticles incorporated, (c) contact angle (white) and CAH (gray) as a function of RTV SR/hexane ratio with 1 wt.% of TiO_2 nanoparticles.....	63
Figure 4.9: Contact angle (white) and CAH (gray) as a function RTV SR/hexane volume ratio with 2 wt. % of TiO_2 nanoparticles incorporated.....	64
Figure 4.10: (a) Water contact angle (CA) and (b) water contact angle hysteresis (CAH) of coating prepared by spin-coating hexane-diluted RTV SR mixture (1:4) with 1 wt.% CeO_2 nanoparticles incorporated, (c) contact angle (white) and CAH (black) as a function of RTV SR/hexane ratio with 1 wt.% of CeO_2 nanoparticles incorporated.....	65
Figure 4.11: Contact angle (white) and CAH (gray) as a function of RTV SR/hexane volume ratio with 2 wt. % CeO_2 nanoparticles incorporated.....	66
Figure 4.12: SEM surface image and EDS spectrum of etched Al sample.....	68
Figure 4.13: SEM surface image and EDS spectrum of Al sample coated with RTV (1:4 v/v) / CeO_2 (2 wt. %).....	68
Figure 4.14: SEM surface image and EDS spectrum of aluminum sample coated with RTV (1:4 v/v) / TiO_2 (2 wt. %).....	69
Figure 4.15: SEM surface image of flat Al sample coated with RTV (1:4 v/v).....	70

Figure 4.16: SEM surface image of etched Al sample coated with RTV (1:4 v/v).....	71
Figure 4.17: SEM surface image of as-received Al sample.....	71
Figure 5.1: Shear stress of ice detachment (kPa) vs. vol % of carbon-black nanoparticles incorporated in RTV SR coated samples. Dashed line presents shear stress on mirror-polished aluminum.....	75
Figure 5.2: Shear stress of ice detachment vs. icing/de-icing cycle number for coatings spin-coated from RTV SR/hexane solutions (1:4 v/v) with (1, 2 wt. %) TiO ₂ and (1, 2 wt. %) CeO ₂ nanoparticles incorporated, respectively.....	76
Figure 5.3: Shear stress of ice detachment vs. icing/de-icing cycle number for coatings spin-coated from RTV SR/hexane solutions (1:4 v/v) with (1, 2 wt. %) TiO ₂ and (1, 2 wt. %) CeO ₂ nanoparticles incorporated, respectively.....	77
Figure 5.4: Ice adhesion reduction factor (<i>ARF</i>) as a function of icing/de-icing cycles on mirror-polished Al and a coating prepared from RTV SR/hexane (1:4 v/v) solution with 1 wt. % of CeO ₂ nanoparticle incorporated.....	79
Figure 5.5: Ice adhesion reduction factor (<i>ARF</i>) as a function of icing/de-icing cycles on mirror-polished Al and a coating prepared from RTV SR/hexane solution (1:4 v/v) with 2 wt. % of CeO ₂ nanoparticle incorporated.....	80
Figure 5.6: Ice adhesion reduction factor (<i>ARF</i>) as a function of icing/de-icing cycles on mirror-polished Al and RTV SR coating with 1 wt. % of TiO ₂ nanoparticles incorporated.....	81
Figure 5.7: Ice adhesion reduction factor (<i>ARF</i>) as a function of icing/de-icing cycles on mirror-polished Al and RTV SR coating with 2 wt. % of TiO ₂ nanoparticles incorporated.....	81
Figure 5.8: Contact angle vs. icing/de-icing cycles number for RTV SR/TiO ₂ (1 and 2 wt. %) coated Al samples.....	82
Figure 5.9: Contact angle vs. icing/de-icing cycles number for RTV/CeO ₂ (1 and 2 wt. %) coated Al samples.....	83
Figure 6.1: Contact angle vs. immersion time in de-ionized water for RTV SR/CB (3 wt. % of carbon-black) coating.....	88
Figure 6.2: Contact angle vs. immersion time in de-ionized water for Al sample coated with RTV (1:4)/TiO ₂ (2 wt. %)......	89
Figure 6.3: Contact angle vs. immersion time in de-ionized water for Al sample coated with RTV (1:4)/CeO ₂ (2 wt. %)......	90
Figure 6.4: Images of small water droplets on cold (-15 °C) surfaces: (a) flat Al, (b) rough super-hydrophobic RTV/CeO ₂ surface.....	91
Figure 6.5: Water droplet freezing time versus contact angle hysteresis of coated samples. Data for uncoated flat Al are also given. The lines are simply guide to the eye.....	92
Figure 6.6: Water drop on a super-hydrophobic surface. Heat transfer at surface/ water drop interface is shown by short arrows.....	94

List of Tables

Table 2.1. Summary of some field observations of natural icing.....	19
Table 6.1. CA, CAH and freezing times of different samples.....	93
Table 6.2. Thermal conductivity values of different material.....	94

List of Symbols and Abbreviations

θ_A	Advancing contact angle ($^{\circ}$)
θ, CA	Contact angle on surfaces ($^{\circ}$)
ρ	Density of drop ($\text{g}\cdot\text{cm}^{-3}$)
ε	Dielectric constant
θ_R	Receding contact angle ($^{\circ}$)
ω	Rotation speed of the beam (angular acceleration, $\text{rad}\cdot\text{s}^{-1}$)
τ	Shear stress of ice ($\text{N}\cdot\text{m}^{-2}$)
γ	Surface tension of a liquid
γ_{SV}	Surface tension of solid-vapor interface ($\text{mN}\cdot\text{m}^{-1}$)
γ_{SL}	Surface tension of solid-liquid interface ($\text{mN}\cdot\text{m}^{-1}$)
γ_{LV}	Surface tension of liquid-vapor interface ($\text{mN}\cdot\text{m}^{-1}$)
A	Apparent de-iced area of the sample surface (m^2)
A_{SL}	Contact areas of liquid-solid interface (m^2)
A_{LA}	Contact areas of liquid-air interface (m^2)
A_F	Flat projected area (m^2)
E_{tot}	Total surface free energy
F	Adhesion force (N)
f_{LA}	Area fraction of liquid–air interface
f_{SL}	Area fraction of solid–liquid interface
f	Fraction of solid surface area wet by the liquid
m	Mass of accumulated ice on Al surfaces (g)
q	Charge on ice surface (C)
q'	Induced image charge (C)
R_q	Root-mean-square
R_f	Roughness factor in Wenzel equation

<i>r</i>	Beam radius (m)
W_A	Work of adhesion ($\text{mN}\cdot\text{m}^{-1}$)
ATH	Alumina tri-hydrate
APTS	3-amino-propyl-triethoxysilane
AC	Alternating current
AFM	Atomic force microscope
<i>F</i>	Adhesion force (N)
<i>ARF</i>	Adhesion reduction factor
CB	Carbon black
CAH	Contact angle hysteresis ($^{\circ}$)
DC	Direct current
EDS	Energy-Dispersive X-ray Spectroscopy
EG	Ethylene glycol
FTIR	Fourier transform infrared spectroscopy
INAAT	Isopropyl tris-(N-amino-ethyl aminoethyl) titanate
ODTS	Octadecyltrichlorosilane
PMMA	Polymethyl methacrylate
PVDF	Polyvinylidene fluoride
PEN	Polyarylene ether nitriles
PECVD	Plasma-enhanced chemical vapor deposition
QLL	Quasiliquid layer
RTV SR	Room-temperature vulcanized silicone rubber
SPAI	Siloxane-modified polyamideimide
SEM	Scanning electron microscope
XPS	X-ray photoelectron spectroscopy

CHAPTER 1

INTRODUCTION

CHAPTER 1

INTRODUCTION

1.1 The Problem of Icing

Atmospheric ice is formed on overhead transmission and distribution lines when they are exposed to supercooled water droplets or snow particles. This may lead to serious risk to the security of overhead networks [1-4]. Atmospheric icing occurs in different forms, including hoar frost which is caused by condensation of vapor, in-cloud icing involving the freezing of supercooled water droplets in clouds or fog, and finally, precipitation icing resulting from freezing rain, drizzle, wet snow or dry snow [1-4]. Flashover on ice-covered overhead insulators is another problem closely related to ice accretion, which causes damage to such insulators and reduces their life-time [4, 5]. Ice accretion, together with superimposed contamination, is well-known to often cause a decrease in the flashover voltage of outdoor insulators, resulting in occasional outages [2].

Ice or wet-snow can cause severe trouble due to their high adherence to both metallic and insulating surfaces. Prevention of ice accretion on surfaces requires reduction of ice adhesion strength. Thus, various anti-icing and de-icing techniques, e.g. chemical, thermal or mechanical removal of ice build-ups, have been developed for decades. Although the majority of the techniques currently in use are called active de-

icing techniques, all of them are employed where ice accumulations are already considerable. Developing passive anti-icing or ice-phobic coatings is gaining in popularity. These kinds of coatings prevent or hinder ice and wet-snow accumulation on such surfaces and are believed to provide reduced ice adhesion [2]. Some of these coatings have been tested by several groups, which will be discussed in the next chapter.

1.2 Current Solutions

The need for reliable electrical transmission and distribution networks under the most severe icing conditions in cold climate regions highlights the importance of ice adhesion studies for reducing ice accretion. Currently, de-icing techniques such as chemical, thermal and mechanical and thermal de-icing are applied extensively. However, these methods are not always advantageous due to their reduced efficiency when it concerns time and cost as well as their limited application which is not general. All these de-icing techniques are used where ice is already accreted and a critical thickness has been reached. Moreover, mechanical de-icing methods using scraping or vibration can damage the target equipment, and sometimes result in gradual degradation of the system itself. An alternative way to prevent ice accretion on the surface of high-voltage equipment would be to apply coatings with reduced ice adhesion properties [3, 7, 8]. Recently, several coatings for ice-phobic application have been tested and reported but the best results belonged to greases and lubricants and not to solid coatings [9]. These ice-phobic coatings must necessarily fulfill both of the

following requirements for a true solution: first, they must efficiently reduce snow or ice adhesion, and second, they must have a reasonably long service-life or durability. In this regards, polymers with low critical surface tension such as organopolysiloxane and tetrafluoroethylene (Teflon®) were examined. Those coatings exhibited satisfactory traction on wet roads; they produced very low run off water contamination and thus demonstrated a significant reduction in ice adhesion [10]. An additional series of investigation revealed that fluorinated and polysiloxane coated surfaces had the poorest wetting by water and are good candidates for ice-phobic coatings [10]. Although de-icing fluids can be applied to ice-covered structures to eliminate such ice build-ups, these substances can have significant negative environmental impacts and thus can only be used as impermanent solutions [11]. In fact, the protection time of anti-icing fluids depends on precipitation conditions and on properties of the fluids. In addition, it should be considered that they need frequent applications in large quantities, which makes them time-consuming and expensive methods. Heating the surface (Joule effect or high frequency current) to melt the ice is another effective method which unfortunately requires a large supply of energy. Electrolysis is another approach found to be effective for removing ice from certain surfaces; however, it is not still a practical method [12].

1.3 Main Objectives

This research work was primarily motivated by: (i) increasing use of silicone rubber-based coatings with the aim to improve the existing high-voltage insulators, (ii)

extensive research on nanopowder-incorporated polymer (and silicone rubber) coatings and their potential need for wide industrial applications (including those on various high-voltage equipment), **(iii)** lack of knowledge in the literature on how such doped silicone-rubber coatings interact with water and, in particular, behave at subzero temperatures.

The main goal of this research work is to study the possibility of preventing or reducing ice accretion on the surface of high-voltage equipment, particularly insulators, by applying super-hydrophobic coatings for reducing ice and snow accumulation. For this purpose, the project is focused on preparation of thin films of appropriate materials with such properties. More specifically, the objectives of this research are the following:

(i) Preparation of nanocomposite coatings based on silicone rubber incorporated with carbon black and certain oxide nanopowders with different dielectric constants.

(ii) Study of hydrophobic and ice-repellent behaviour of the prepared coatings as a function of the added nanopowder (dopant) nature and concentration; comparison with non-doped coatings, as well as study of the effect, if any, of different dopant (with different electrical properties) incorporated into the coatings on their wetting and/or ice-releasing properties.

(iii) Preparation of rough super-hydrophobic coatings, study of their hydrophobic properties and ice-releasing performance; comparison with flat surfaces. Comparative study of water freezing behaviour on different samples.

(iv) Study of stability of the coatings in water and during icing/de-icing cycles, as well as their surface topography, their structural, chemical properties, in order to determine their potential for applications to high-voltage equipment (such as conductors and insulators).

1.4 Methodology

Regarding the above objectives, the following experimental methodology has been used on aluminum alloy surfaces. After the aluminum samples were cleaned and then (if necessary) polished or etched, they were coated with silicone rubber with different dopants, while applying a variety of experimental parameters or different pre/post treatments as summarized below:

(i) As-received carbon-black nanoparticles (from Columbian Chemicals, specification Conductex 7055 Ultra, with the average size of 42 nm and the surface area of $55 \text{ m}^2 \cdot \text{g}^{-1}$) were used as dopant. A commercial-grade alumina-filled room temperature vulcanized silicone rubber (RTV SR) purchased from Dow Corning (DOW CORNING® HVIC 1547) was used as a hydrophobic material. According to the manufacturer, it consists of alumina hydrate, hydrotreated light petroleum, stoddard solvent, methyl tri (ethylmethylketoxime)silane, di (ethylmethylketoxime)methoxymethylsilane, and xylene. Carbon-black nanoparticles were mixed in different volume ratios with the RTV silicone rubber in a beaker under vigorous magnetic stirring. Similarly, TiO_2 and CeO_2 nanopowders (from Sigma-

Aldrich, particle size below 100 and 25 nm, respectively) were also used as dopants in RTV SR coatings. Such mixed solutions (particle suspension in liquid) were used to prepare nanocomposite coatings on aluminum substrates for wetting and structural characterizations. It should be noted that the RTV SR product (used as-supplied from the manufacturer) had alumina micro- particles (average size $\sim 3 \mu\text{m}$) as a filler improving its mechanical properties. However, since the concentration of such alumina particles was constant, their contribution to the properties of the tested samples was same for both non-doped and doped (with CB, TiO_2 or CeO_2 powders) coatings. Therefore, adding different amounts of the above dopant nanopowders allowed us to elucidate their effect on the hydrophobic and ice-releasing properties of doped coatings in comparison with their non-doped counterparts. The coatings were prepared using a spin-coater from Laurel (WS-400B-6NPP) followed by curing in a conventional oven in air. The choice of metal substrates was mainly dictated by the necessity to use some samples for icing/de-icing experiments in a centrifuge. Aluminum alloy (AA6061) was used as substrate. The influence of different parameters on the formation and properties of such layers has been analyzed in order to optimize the coating process.

(ii) The wetting behaviour of the coatings, sessile water contact angle and wetting hysteresis was evaluated on a Kruss DSA100 goniometer. The ice adhesion strength was evaluated in a house-made centrifuge apparatus (centrifuge adhesion testing machine) placed in a cold room at subzero temperature. The type of ice used was glaze, prepared by spraying supercooled micrometer-sized water droplets ($\sim 80 \mu\text{m}$) in a wind tunnel at -10°C , wind speed $11 \text{ m}\cdot\text{s}^{-1}$ and water feed rate of $2.5 \text{ g}\cdot\text{m}^{-3}$.

(iii) Both flat and rough coatings were prepared on flat as well as rough substrates by means of spin-coating. Their wetting behaviour at room temperature, low temperature as well as their ice-releasing properties was compared with those on flat samples. Ice adhesion experiments were carried out on such coatings in order to find out what parameters govern this property of the coating.

(iv) Scanning Electron Microscopy (SEM) and Atomic Force Microscopy (AFM) were used for surface imaging.

(v) Chemical analysis of prepared coated surfaces was carried out using energy-dispersive X-ray spectroscopy (EDS) during SEM.

1.5 Statement of Originality

As will be expressed broadly in Chapter 2, the previous efforts were mostly concentrated on the electrical and mechanical properties of nanoparticle-incorporated RTV SR coatings. However, information on their water-repellent and ice-releasing properties is scarce. In this research work, thus, we considered the behaviour of RTV SR coatings incorporated with nanoparticles at subzero temperatures (-10 to -15 °C), and the opportunity of preparing super-hydrophobic coatings to reduce ice accumulation. Such coatings could further decrease ice and wet-snow accumulation and adhesion on the surface of exposed equipment. Freezing of water droplets on various coated surfaces was also studied as compared with that of flat coated and uncoated aluminum surfaces, behaviour at subzero temperatures. Evaluating ice adhesion strength

considering the effect of all possible conditions on coating properties were investigated by means of the facilities provided at the CIGELE (the Industrial Chair on Atmospheric Icing of Power Network Equipment) and INGIVRE (the Canada Research Chair on Engineering of Power Network Atmospheric Icing) laboratories at UQAC.

1.6 The Outline of Thesis

The thesis is organized in the seven chapters as follows:

- Chapter 1 presents a summary of icing related issues, a short introduction to the current solutions as well as a general introduction of this research work including the research objectives, methodology, motivation for this work, the thesis organization, etc.
- Chapter 2 provides a review of the available literature and background studies on hydrophobicity, super-hydrophobicity, icephobicity and nanoparticles. The concepts and explanations provided in this chapter make it possible to understand the principles of the tests and the reasons for choosing the coatings used in this research. This chapter also summarizes previous studies and results obtained related to the topic which should be of help to the reader.

- Chapter 3 explains the experimental procedures for preparing the nanoparticle-silicone rubber suspensions, coating preparations and characterization methods. It also provides a description of the facilities and techniques used for characterizing the prepared coatings, e.g. Contact Angle Goniometer, Spin-Coater, Atomic Force Microscope (AFM), Cold Climatic Chamber (cold room), wind tunnel, Centrifuge Adhesion Test Machine, Scanning Electron Microscope (SEM), Energy-Dispersive X-ray Spectroscopy (EDS), etc.
- Chapter 4 presents the results of the water-droplet behaviour study for the nanoparticle-incorporated RTV SR coatings on flat or rough aluminum substrate.
- Chapter 5 provides the experimental results obtained on the prepared coatings in terms of hydrophobic and super-hydrophobic properties, ice-phobicity and surface characterizations, e.g. morphological and chemical analyses. The obtained ice adhesion test results as well as the contact angle values as function of icing/de-icing number after each icing/de-icing cycle on the coated samples are also discussed in detail in this chapter. These sets of experiments were conducted to trace any possible effect of ice detachment on the coating performance during icing/de-icing events.

- Chapter 6 describes the results obtained concerning the freezing of water droplets on coated and non-coated sample surfaces and the stability of prepared coated samples immersed in de-ionized (DI) water.
- Chapter 7 includes general conclusions and recommendations for future studies based on this research work including the obtained results and their discussion.
- Finally, the references which were cited in this thesis are presented at the end of this thesis.

An exhaustive survey of the literature related to the concept of wettability, hydrophobicity and super-hydrophobicity, nanoparticles and ice-phobic properties is presented in the following chapter.

CHAPTER 2

BACKGROUND AND LITERATURE REVIEW

CHAPTER 2

BACKGROUND AND LITERATURE REVIEW

Superstructure icing from atmospheric icing on the equipments may impact their operations and can reduce their safety, operational tempo, and productivity. A number of new technologies and modern versions of old technologies used successfully in aviation, the electric power industry, and ground transportation systems. Making a surface where ice would not stick to it would be an ideal and economical solution to eliminate application of de-icing techniques. Such a surface is defined as “ice-phobic” surface. Creating an ice-phobic surface is possible through knowledge of the physics of ice and ice accretion processes and methods for prediction of icing events. These ice-repellent surfaces can be created by applying an appropriate morphological surface modification followed by the use of a coating. This coating should have chemical components with a weak chemical interaction with ice or snow.

In this chapter, we will briefly review atmospheric icing followed by a brief review of the mechanisms of ice adhesion and a discussion of hydrophobicity and superhydrophobicity.

2.1 Atmospheric Icing and Types of Ice

Atmospheric icing occurs when water droplets in the atmosphere freeze on objects they contact. Water drops can be cooled down much below bulk water freezing point (0 °C) on which tiny water drops may remain in liquid state below freezing point. For a supercooled droplet, the liquid state is thermodynamically unstable and indeed the most stable state for supercooled droplet is the solid state. This is very dangerous on aircrafts. For power transmission lines going through mountains, for instance, the built-up ice changes the aerodynamics of the flight surfaces, which can increase the risk of a subsequent stalling of the airfoil, mechanical and electrical damages of the power transmission lines or flashover on the insulators. Atmospheric icing combined with wind is a main factor for power line design and reliability. The freezing process of water droplet may be accelerated by presence of any substance that can act as a freezing nucleus, which makes possible the growth of an ice crystal on itself.

Ice accretion can be defined as any process of ice build-up and snow accretion on the surface of an object exposed to the atmosphere. Types of accreted ice depend on wind speed, supercooled water droplet size, compressive strength, air temperature and properties of the objects being hit by droplets [13]. However, two sources of atmospheric ice accretion are recognized regarding to their methods of deposition and characteristics of deposits:

(1) In-cloud icing happens where supercooled water droplets are sufficiently small to remain suspended and contact with surface results from air movement. This category generally includes hard rime, soft rime, but sometimes glaze. In-cloud icing

usually happens in the aircraft flying through clouds or on the equipment installed in high altitude [14]. When the flux of water droplets towards an object is less than the freezing rate, each droplet freezes before the next droplet impinges on the same spot. Such kind of ice growth is called dry icing. When the water flux increases, the droplets do not have the required time to freeze before the next impinges, hence the ice growth will tend to be wet. Dry icing usually results in different types of rime containing air bubbles, while wet icing always forms glaze ice which is solid and clear. In fact, the physical properties and the appearance of the accreted ice vary widely according to the variations of the meteorological conditions during the ice growth. The maximum amount of accreted ice on an object depends on several factors. The most important factors are air temperature, relative humidity, and the duration of ice accretion. However, a major precondition for significant ice accretion is the dimensions of the object exposed and its orientation to the direction of the icing wind.

(2) Precipitation icing occurs when the droplets are massive enough to fall from the atmosphere onto an accreting surface. In other words, precipitation icing may happen when a warm layer of air with the temperature of $> 0\text{ }^{\circ}\text{C}$ is trapped between two layers of cold air with the temperature of $< 0\text{ }^{\circ}\text{C}$) during freezing rain. Precipitation icing can occur everywhere regardless of altitude. This type includes freezing precipitation and wet snow. Precipitacional icing generally gives rise to glaze ice accumulations.

Glaze ice forms when droplets striking a surface have sufficient time prior to freezing to flow in a continuous film (Fig. 2.1c). Glaze is caused by freezing rain, freezing drizzle or wet in-cloud icing and usually causes smooth evenly distributed ice

accretion. The accretion rate mainly varies with the rate of precipitation, wind speed and also air temperature. This condition is most common when air temperatures are just below freezing and rain is the dominant precipitation form. Glaze often forms a hard, nearly homogeneous ice layer having the highest density approaching 0.917 g cm^{-3} , that of bubble-free ice [15]. Glaze can also result in formation of icicles with the more asymmetric shape [16, 17, 18]. The surface temperature of accreted ice is near freezing point, and thus water may flow around the object and freeze on the leeward side. As mentioned, glaze ice is denser and applies larger static or dynamic forces to the instruments. In addition, it conducts the electricity easier, and therefore is more risky for the performance of the electric networks.

Rime forms tiny coatings on snow crystals or enormous accumulations up to several meters thick on terrestrial objects and is the most common type of in-cloud icing. When supercooled water droplets hit a dry cold surface, they freeze as soon as the latent heat of fusion is dissipated and rime ice accumulates. Lower temperatures usually create hard rime or soft rime that will be explained later (Fig. 2.1). Depending on meteorological conditions, rime accretions can be dense, compact masses, feathery surfaces, or slender, needle-like spikes. Close examination often reveals a fine grained, granular structure without any recognizable crystalline pattern. Rime grows into the prevailing wind and is a reliable indicator of wind direction during icing events [19]. The liquid water content of the air becomes so small at temperatures below $\sim -20 \text{ }^\circ\text{C}$ that practically no in-cloud icing occurs. It results in an ice accretion more or less cylindrical around the objects. The most severe rime icing occurs on freely exposed mountains, coastal or inland, or where mountain valleys force moist air to pass around,

as a result, both lifts the air and increases wind speed over the pass. The accretion rate for rime varies on dimensions of the exposed object, wind speed, liquid water content in the air, water drop size and air temperature.

Soft rime forms when the supercooled droplets freeze quickly upon deposition (Fig. 2.1a). The dissipation of latent heat is rapid; no flow occurs and large amounts of air are entrapped. The deposit often has an opaque-white, porous, and fluffy appearance. Soft rime has a density of less than 0.6 g cm^{-3} [20].

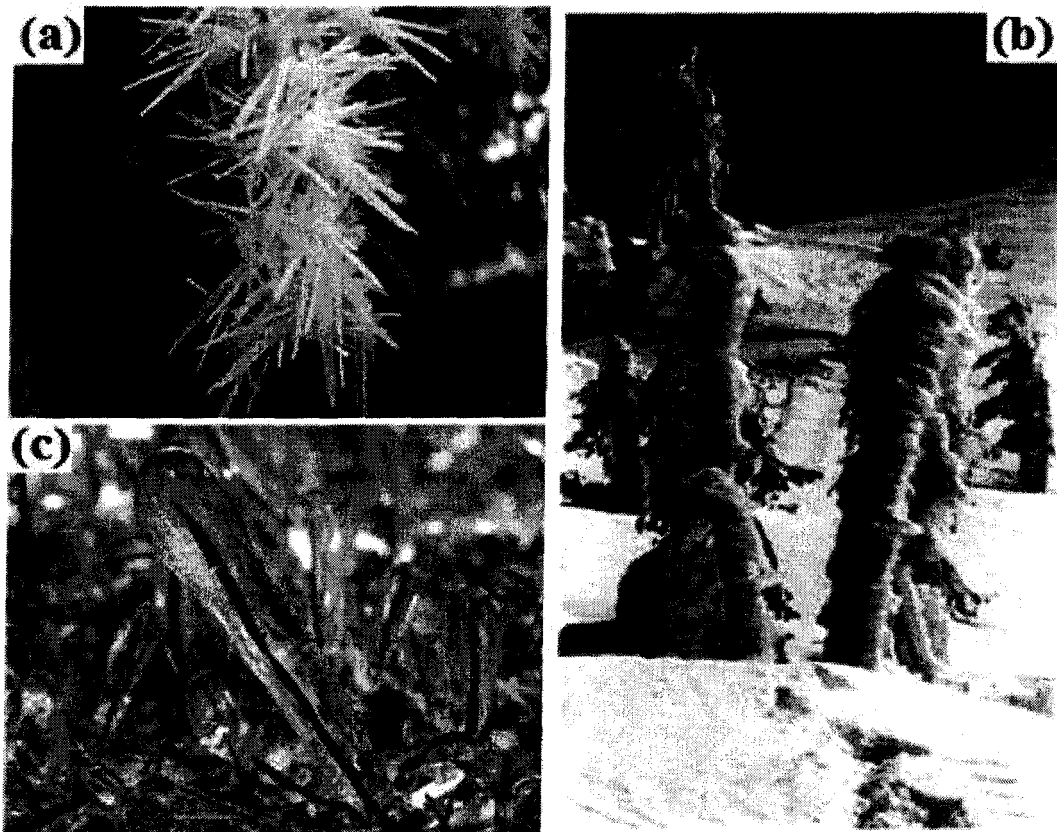


Fig. 2.1. (a) Soft rime, (b) hard rime ice on ridge-top vegetation, Sierra Nevada crest, (c), glaze ice.

“Hard” rime forms when the rate of latent heat loss is relatively low, allowing “wet growth” whereby some flow of the droplets occurs before complete freezing (Fig.

2.1b). Hard rime is generally milky or translucent in appearance, depending upon the amount of air trapped within the ice structure. Its density ranges from 0.6 to 0.9 g cm⁻³. The third condition is known as “frost” [20]. Frost or “hoarfrost” forms under still air conditions by deposition of water directly from the vapour phase to a cold surface. Since water vapour amounts are minimal at subfreezing temperatures, and still air conditions are infrequent at mountainous sites, at high elevations frost is much less frequent than other types of ice accretions [21].

Although meteorological conditions associated with the formation of glaze and rime have been investigated, due to the complexity of the phenomenon, geographic differences and monitoring disparities, a wide range in conditions has been reported (Table 2.1). This is particularly the case in field situations due to the complexity of mountain weather. In general, soft rime, at one end of the spectrum, is favoured by conditions that promote a high degree of droplet super-cooling and rapid dissipation of the latent heat of fusion (low air temperatures and low wind speeds). At the other end of the spectrum, glaze is formed under the opposite of these conditions. Hard rime is an inter-mediate form of these two extremes.

Many combinations of droplet size, liquid water content, air temperature, wind speed, etc., are capable of producing the thermo-dynamics necessary such that an individual parameter may fall outside of its generally stated range. The most dangerous ice accretions are glaze, hard rime, wet snow and mixtures.

Table 2.1. Summary of some field observations of natural icing [22, 26].

Meteorological variable and/or range	Ice condition
Air temperature - 5 to - 14 °C	Rime most frequent
Air temperature 0 to - 4 °C	Observer-reported icing most frequent
Air temperature blow 1°C with low wind	Hard rime common
Air temperature ≤ 5 °C and wind ≥ 5 ms ⁻¹	Soft rime common
Wind speed and event duration	Positively correlated with amount of ice
Air temperature - 2 to - 3 °C	Optimum for hard rime
Air temperature - 14 to - 15 °C	Optimum for soft rime
Air temperature 0 to - 6 °C	Accretion rates greatest
Air temperature - 2 to - 3 °C	Intensity of Accretion greatest
Air temperature - 3 to - 6 °C	Frequency of rime events greatest
Wind speed	Rime growth intensity increases with wind velocity
Wind speed 1 to 10 ms ⁻¹ and air temperature - 1 to 10 °C	Soft rime
Wind speed 3 to 15 ms ⁻¹ , air temperature - 2 to - 8 °C	Hard rime
Wind speed 2 to 20 ms ⁻¹ , air temperature 0 to - 3 °C	Glaze
I=product of wind speed (ms ⁻¹) and the constant 0.011	Rime formation rate, I (g cm ⁻² h ⁻¹)

2.2 Ice Adhesion Mechanisms

As previously discussed in chapter 1, ice and snow adhesion and accumulation bring dangerous and costly problems into our everyday lives. Ice is responsible for significant and serious problems on different structures. Generally, atmospheric icing is

the deposition of frozen water on surfaces at or below freezing which may result of rain, freezing rain, wet snow, fog, supercooled clouds or vapour, or from spray or splashing water. Ice adhesion produces numerous troubles in many areas of human activity such as transportation, power transmission and distribution, aircraft, wind turbine blades, ships, and bridges [27]. Icing of power transmission lines during winter storms is a persistent problem that causes outages and costs millions of dollars in repair expenses [28]. Control of icing by physical removal such as applying heating or chemicals may be possible but is costly and not generally practicable. The development of materials with low adhesion to ice is a very important problem [29].

Its solution requires a fundamental understanding of the physical mechanisms of bonding between ice and other solids. In particular, it needs to know the nature and strength of molecular bonding between ice and various solids. Why does ice adhere to any solid, even to hydrophobic materials? What changes occur over time in ice adhesion? Fundamental and theoretical studies are needed, for the first step, to provide answers to these questions which will be explained in details as objectives of this chapter.

The required force to ice detachment from the surface is typically termed as ice adhesion force. Many parameters can influence the adhesion of ice to a surface, e.g. substrate surface properties, conditions of ice formation, air temperature, freezing rate, water contact area, droplet momentum and etc. Though, the fundamental physics of ice adhesion is not well-known up to now [30], three major components of ice adhesion to surface of materials are involved: hydrogen bonds, dispersion or Lifshitz-van der Waals forces, and electrostatic interactions contribute to ice/solid interfacial energy. Their

relative importance depends on the nature of the material to which ice adheres. Adhesion of ice to a particular substrate is also affected by a quasiliquid layer (QLL) on the interface and by the substrate surface roughness [31]. Adhesion of ice is usually a property of the ice/solid interface that can act via strong interaction between ice molecules and solid surface. In ideal case, all three types of interaction must be eliminated to have zero or reduced ice adhesion. Chemical bonding involves a chemical reaction between the molecules on opposite sides of the interface and will be specific to the nature of the materials concerned.

The role of chemical bonding in ice adhesion has not been sufficiently studied yet. Van Oss *et al.* determined the surface energy of ice within the context of modern surface chemistry. They separated the surface free energies of ice into Lifshitz-van der Waals and Lewis acid-base components, using measurements of the contact angles of various liquids on ice and experiments to observe the exclusion or incorporation of various colloidal particles in an advancing freezing interface. They finally concluded that at 0 °C only 26.9 mJ m⁻² of the total surface energy of 69.2 mJ m⁻² arises from the Lifshitzvan der Waals interaction [32]. Van der Waals forces are of longer range than hydrogen bonding and are always present at the interface. The Lifshitz-van der Waals forces between ice and several metals and insulators were calculated by Wilen *et al.* who concluded that these are not the dominant source of ice adhesion. They also concluded that electrostatic interaction may play a more important role in ice adhesion rather than Lifshitz-van der Waals forces [32].

Electrostatic interactions occur between non-compensated spatial distributions of charge on opposite sides of the interface at greater than intermolecular distances and

contribute significantly to ice adhesion with interaction energy of up to 500 mJ m⁻² [29]. So the electrostatic forces of attraction between charges on ice and induced image charges are considered to play a significant role in ice adhesion, although the fundamental physics of ice adhesion is yet to be fully explored. However, it is a well-known fact that ice adheres to any surface. Exerting an external force on the ice-solid interface can lead to cohesive rupture (breaks that happen within the ice) or adhesive rupture (breaks that happen at the ice-solid interface and occur when the strength of adhesion is lower than the strength of ice) [33]. The electrostatic interaction energy between ice and metals has been found to be significantly higher than the hydrogen bonding and Van der Waals forces at greater than intermolecular distances [29]. Charges on ice induce smaller charges on dielectrics, the reduction being related to the dielectric constant by the equation (1):

$$q' = q \frac{\varepsilon - 1}{\varepsilon + 1} \quad (1)$$

Where q' is the image charge produced by a charge q on the ice surface and ε is the dielectric constant of the insulating substrate. According to the above equation, materials with a very low dielectric constant would significantly reduce the adhesion of ice by reducing the electrostatic interaction (whose force $F \propto \frac{qq'}{r^2}$, where r is the distance between q and q').

It should be noted that experimental conditions to measure ice adhesion must be carefully defined; otherwise it is difficult to correlate basic or experimental adhesion with practical adhesion because of:

i) An adhesive layer will rupture in the bulk adhesive rather than at the interface and thus it can affect on the reproducibility of the experimental results.

ii) Difficulty to measure and quantify intermolecular forces, presence or absence weak boundary layers, the mode of applying stress, intrinsic stresses and the failure mode on adhesion of ice [34].

2.3 Brief Review on Hydrophobic and Super-hydrophobic Properties

2.3.1 Hydrophobicity and Contact Angle

Hydrophobicity of any material is its resistance to flow of water on its surface. A surface is termed as highly hydrophobic if it resists to flowing water dropped on it and is least hydrophobic surface if water droplets flow in form of tracks on its surface. The hydrophobic surface is water repellent, in contrast with a hydrophilic surface that is easily wetted. From the point of insulators, hydrophobicity is treated as a resistance to the formation of conducting water tracks that increase leakage current, chances of flashover, and other deterioration effects [35]. Coating any surface with anti-icing materials can be an effective way of reducing/preventing ice accretion. For ice to adhere to a surface, it is necessary for water to “wet” the surface which means replacing the substrate-air interface with a substrate/water interface. This tendency to wet the surface can be determined by measuring the angle the surface of a liquid drop makes with the solid surface [36]. Young and Laplace found out that each surface has a

specific energy because the surface atoms or molecules of liquids or solids have fewer bonds with neighbouring atoms, and therefore, they have higher energy than similar atoms and molecules in the interior. This additional energy is characterized quantitatively by the surface tension or free surface energy γ , which is equal to the work that is required to create a unit area of the surface at a constant pressure and temperature. The unit of γ is J m^{-2} or N m^{-1} and it can be interpreted either as energy per unit surface area or as tension force per unit length of a line at the surface. When a solid is in contact with a liquid, the molecular attraction will reduce the energy of the system below that for the two separated surfaces. This is expressed by the Dupré equation:

$$W_{SL} = \gamma_{SA} + \gamma_{LA} - \gamma_{SL} \quad (1)$$

Where W_{SL} is the work of adhesion per unit area, γ_{SA} and γ_{SL} are the surface energies of the solid against air and liquid, and γ_{LA} is the surface energy of liquid against air [37, 39]. If a liquid droplet is placed on a solid surface, the liquid and solid surfaces come together under equilibrium at a characteristic angle called the static contact angle θ_0 (Fig.2.2).

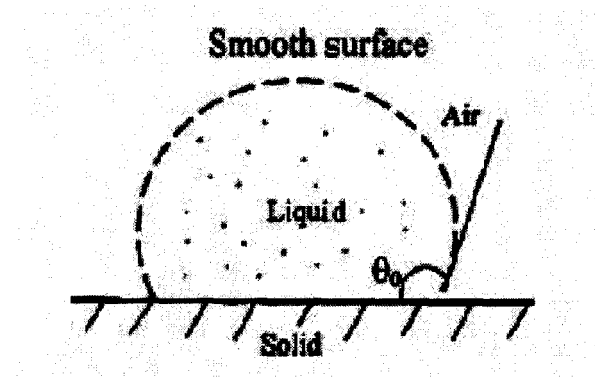


Fig. 2.2. Schematic of liquid droplet in contact with a smooth solid surface (contact angle, θ_0).

This contact angle can be determined by minimizing the net surface free energy of the system [37, 39]. The total energy E_{tot} is given by [40, 41].

$$E_{\text{tot}} = \gamma_{LA} (A_{LA} + A_{SL}) - W_{SL} A_{SL} \quad (2)$$

Where A_{SL} and A_{LA} are the contact areas of the liquid with the solid and air, respectively. It is assumed that the droplet of density ρ is smaller than the capillary length, $(\gamma_{LA}/\rho g)^{1/2}$, so that the gravitational potential energy can be neglected. It is also assumed that the volume and pressure are constant, so that the volumetric energy does not change. At the equilibrium $dE_{\text{tot}} = 0$, which yields:

$$\gamma_{LA} (dA_{LA} + dA_{SL}) - W_{SL} dA_{SL} = 0 \quad (3)$$

For a droplet of constant volume, it is easy to show using geometrical considerations, that:

$$dA_{LA}/dA_{SL} = \cos \theta_0 \quad (4)$$

Combining Eqs. (1), (3), and (4), the well-known Young equation for the contact angle is obtained:

$$\cos \theta_0 = (\gamma_{SA} - \gamma_{SL}) / \gamma_{LA} \quad (5)$$

The contact angle (CA, θ_0) is the macroscopic indicator of the surface energy balance and the equilibrium of surface energy can determine the entire shape of a droplet on a solid, provided that the drop is small enough. Wetting phenomenon is normally described as a contact angle (θ_0) of the specific surface, i.e., $\theta_0 > 90^\circ$ as

hydrophobic surface; $\theta_0 < 90^\circ$ as hydrophilic surface (Fig. 2.3). The greater contact angle, preferably $>150^\circ$, the better water-repellency and self-cleaning abilities can be achieved [42]. The maximum CA that already obtained on a flat surface with regularly aligned closest-hexagonal-packed CF_3 groups equals about 120° with extreme value of surface energy [43].

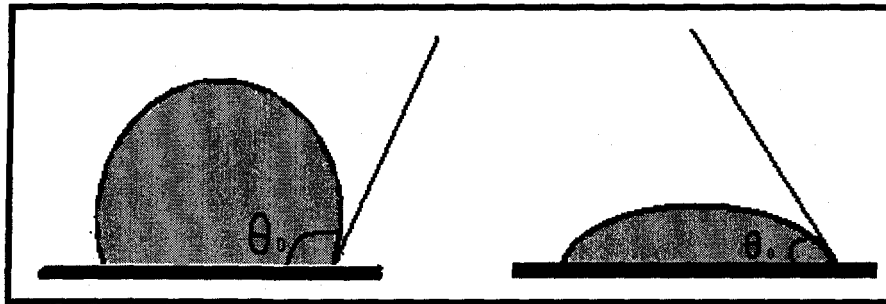


Fig. 2.3. A schematic diagram of hydrophobic surface (left), and hydrophilic surface (right).

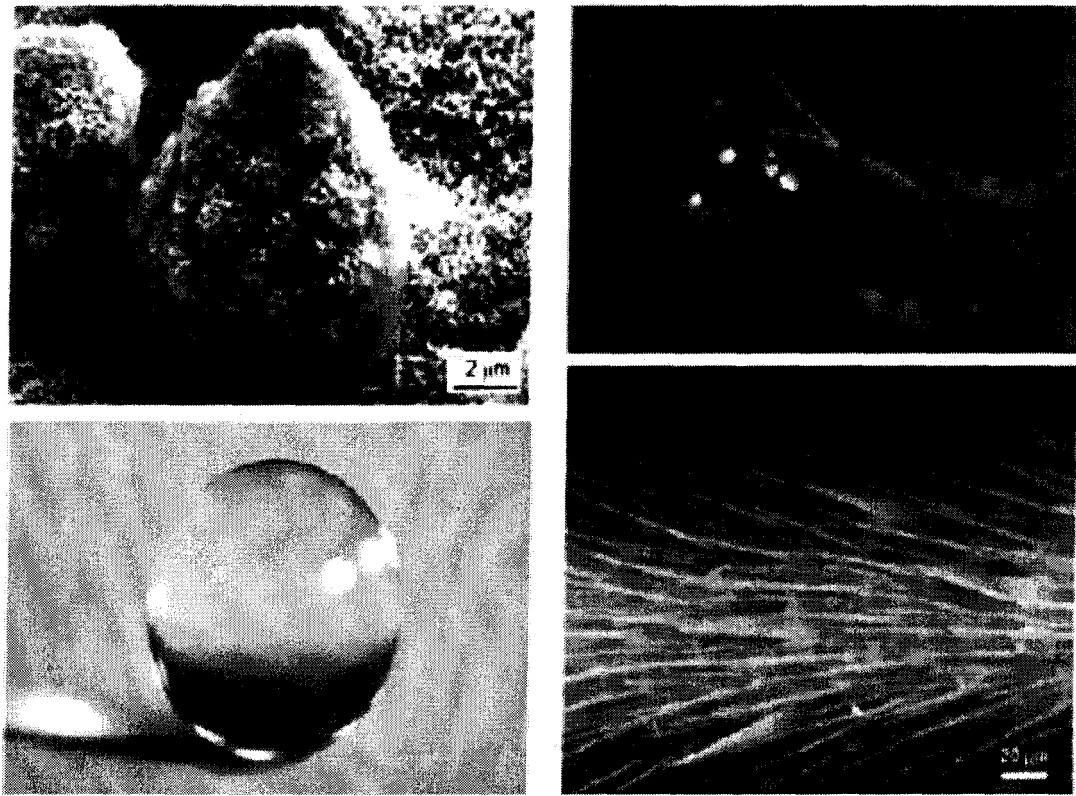
2.3.2 Super-hydrophobicity and Roughness

A) Super-hydrophobicity in Nature

There are a large number of objects, including bacteria, plants, land and aquatic animals, and seashells, with properties of commercial interest. Fig. 2.4 shows a montage of some examples from nature [44]. Some leaves of water-repellent plants, such as *Nelumbo nucifera* (Lotus), are known to be super-hydrophobic and self-cleaning due to hierarchical roughness (microbumps superimposed with a nanostructure) and the presence of a hydrophobic wax coating (Fig. 2.5). Static contact

angle of a Lotus leaf are about 164° [45, 46]. The water droplets on the leaves remove any contaminant particles from their surfaces when they roll off, leading to self-cleaning [44, 47-53]. Water droplets on these surfaces readily sit on the apex of nanostructures because air bubbles fill in the valleys of the structure under the droplet. Therefore, these leaves exhibit considerable super-hydrophobicity (Fig. 2.4a).

Pond skaters (*Gerris remigis*) have the ability to stand and walk upon a water surface without getting wet (Fig. 2.4b). Even the impact of rain droplets with a size greater than the pond skater's size does not make it immerse in the water.



(a)

(b)

Fig. 2.4. Montage of some examples from nature: (a) Lotus effect [33], and (b) pond skater walking on water [54].

Gao and Jiang [54] showed that the special hierarchical structure of the pond skater's legs, which are covered by large numbers of oriented tiny hairs (micro setae) with fine nanogrooves and covered with cuticle wax, makes the leg surfaces super-hydrophobic, is responsible for the water resistance, and enables them to stand and walk quickly on the water surface. Research on super-hydrophobic surfaces has limited attention before the mid-1990s. In fact, all studies were focused to find out the relation between contact angles and surface geometry of super-hydrophobic phenomena observed on the "triticum aestivum" plant leaves and insect cuticles [55-57]. It was mentioned that previous studies approved that the combination of suitable surface roughness and low-surface-energy materials is responsible for super-hydrophobicity. This line of research becomes reactivated because Neinhuis and Barthlott explained the origin and universal principle of the "lotus effect" in nature in 1997 (Fig. 2.5).



Fig. 2.5. SEM micrographs (shown at three magnifications) of Lotus (*Nelumbo nucifera*) leaf surface which consists of microstructure formed by papillose epidermal cells covered with 3-D epicuticular wax tubules on surface, which create nanostructure [45].

They have shown that lotus effect is due to the presence of a rough micro-nanostructure surface covered with epicuticular wax crystalloids that result in a surface with water contact angle greater than 150° [58]. This special surface roughness along

with covering by low-surface-energy materials is responsible for their self-cleaning properties. Surfaces with a contact angle of less than 10° are called super-hydrophilic, while surfaces with a contact angle between 150° and 180° are called super-hydrophobic surfaces. The schematic illustration and wetting behaviour of four different surfaces is presented in Fig. 2.6. As it is evident in this figure, the largest contact area between the droplet and the surface is related to the flat and microstructured surfaces; however the contact area is reduced in nanostructured surfaces and is minimized in hierarchical structured surfaces.

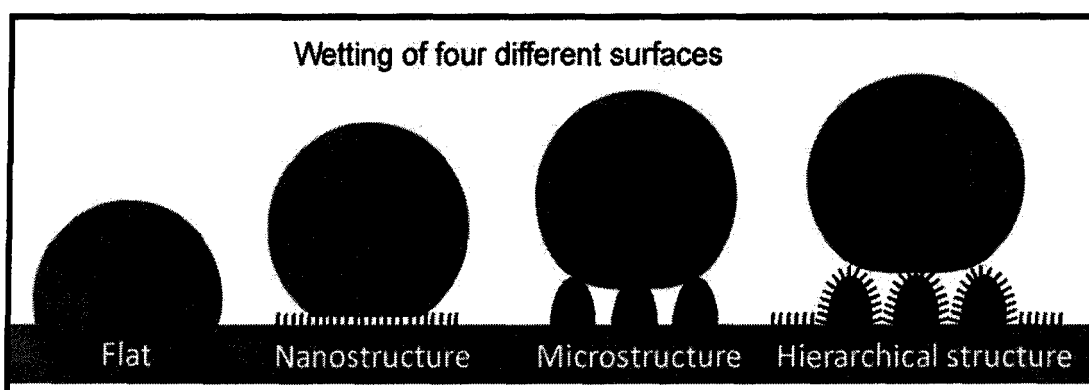


Fig. 2.6 Schematic and wetting of the four different surfaces. The largest contact area between the droplet and the surface is given in flat and microstructured surfaces, but is reduced in nanostructured surfaces and is minimized in hierarchical structured surfaces.

B) Roughness-Induced Super-Hydrophobicity, Self-Cleaning and Low Adhesion

One of the ways to increase the hydrophobic or hydrophilic properties of a surface is to increase surface roughness, so roughness-induced hydrophobicity or

hydrophilicity has become the subject of extensive investigations. Wenzel [59] suggested a simple model predicting that the contact angle of a liquid with a rough surface is different from that with a smooth surface. Cassie and Baxter [60] showed that a gaseous phase including water vapour, commonly referred to as “air” in the literature, may be trapped in the cavities of a rough surface, resulting in a composite solid–liquid–air interface, as opposed to the homogeneous solid–liquid interface. These two models describe two possible wetting regimes or states on rough surfaces: the homogeneous (Wenzel) and the composite (Cassie–Baxter) regimes. Johnson and Dettre [61] showed that the homogeneous and composite interfaces correspond to the two equilibrium states of a droplet.

In this section, numerical models which provide relationships between roughness and contact angle and contact angle hysteresis, as well as the Cassie–Baxter and Wenzel regime transition, are discussed. A water droplet on a rough surface with a homogeneous interface, the interface area increases with respect to that for a smooth surface. Using the surface force balance and empirical considerations, the contact angle of a water droplet upon a rough solid surface, θ , is related to that upon a smooth surface, θ_0 for a homogeneous interface (Fig. 2.7a), through the non-dimensional surface roughness factor, $R_f > 1$, equal to the ratio of the surface area, A_{SL} , to its flat projected area, A_F [59].

$$\cos \theta = (d A_{LA}) / (d A_F) = (A_{SL} / A_F) \times (d A_{LA} / A_{SL}) = R_f \cos \theta_0 \quad (6)$$

Where,

$$R_f = A_{SL} / A_F \quad (7)$$

This is called the Wenzel equation. The dependence of the contact angle on the roughness factor is presented in Fig. 2.8a for different values of θ_0 . The Wenzel model predicts that a hydrophobic surface ($\theta_0 > 90^\circ$) becomes more hydrophobic with an increase in R_f , while a hydrophilic surface ($\theta_0 < 90^\circ$) becomes more hydrophilic with an increase in R_f [40, 62].

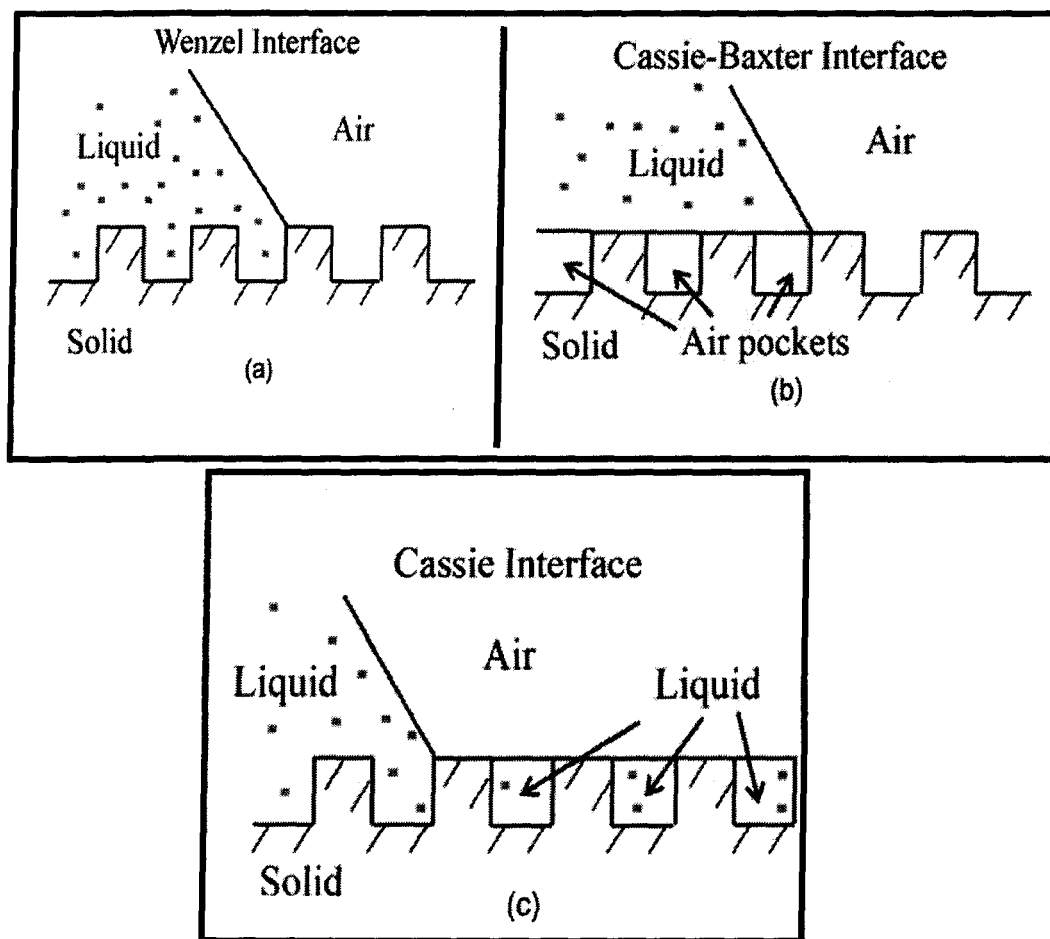


Fig. 2.7. Schematics of configurations described by the (a) Wenzel equation for the homogeneous interface (Eq. (6)), (b) Cassie-Baxter equation for the composite interface with air pockets (Eq. (9)), and (c) the Cassie equation for the homogeneous interface (Eq. (10)) [63].

As an example, Fig. 2.8b shows geometry with square-based hemispherically-topped pyramidal asperities with a rounded top, which has complete packing. The size and shape of the asperities can be optimized for a desired roughness factor. In a similar manner, for a surface composed of two fractions, one with the fractional area f_1 and the contact angle θ_1 and the other with f_2 and θ_2 , respectively (so that $f_1 + f_2 = 1$).

$$\cos \theta = f_1 \cos \theta_1 + f_2 \cos \theta_2 \quad (8)$$

For the case of a composite interface (see Fig. 2.7b), consisting of a solid–liquid fraction ($f_1 = f_{SL}$, $\theta_1 = \theta_o$) and liquid–air fraction ($f_2 = f_{LA} = 1 - f_{SL}$, $\cos \theta_2 = -1$), combining Eqs. (7) and (8) yields the Cassie–Baxter equation [60]:

$$\begin{aligned} \cos \theta &= R_f f_{SL} \cos \theta_o - 1 + f_{SL} \\ \cos \theta &= R_f \cos \theta_o - f_{LA} (R_f \cos \theta_o + 1) \end{aligned} \quad (9)$$

The opposite limiting case of $\cos \theta_2 = 1$ ($\theta_2 = 0^\circ$ corresponds to the water-on-water contact) yields the Cassie equation [41, 63]:

$$\cos \theta = 1 + f_{SL} (\cos \theta_o - 1) \quad (10)$$

Eq. (10) is used sometimes for the homogeneous interface instead of Eq. (6), if the rough surface is covered by holes filled with water [64] (Fig. 2.7c).

Two situations in wetting of a rough surface should be distinguished: the homogeneous interface without any air pockets was shown in Fig. 2.7a (called the Wenzel interface, since the contact angle is given by the Wenzel equation or Eq. (6)),

and the composite interface with air pockets trapped between through details as shown in Fig. 2.7b (called the Cassie or Cassie–Baxter interface, since the contact angle is given by Eq. (9)).

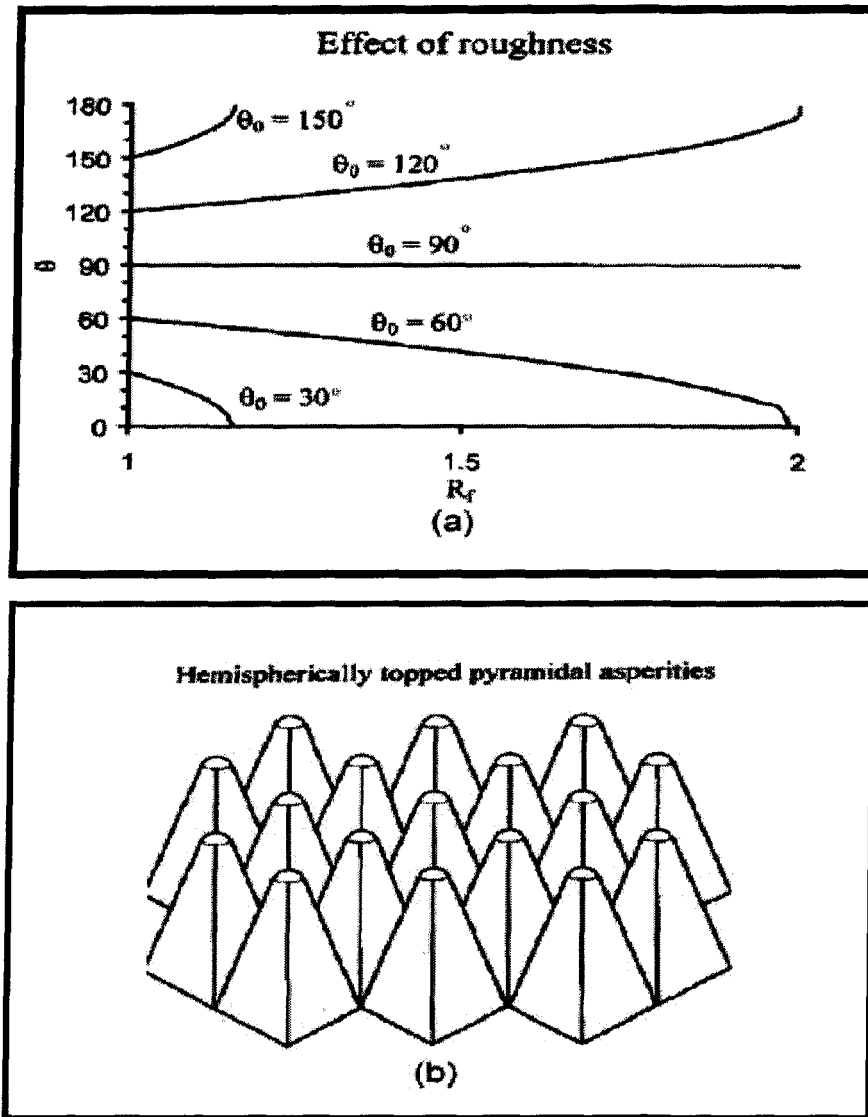


Fig. 2.8. (a) Contact angle for rough surface (θ) (Wenzel regime) as a function of the roughness factor (R_f) for various contact angles of the smooth surface (θ_0), and (b) schematic of square-based hemispherically-topped pyramidal asperities with complete packing [40].

Numerous super-hydrophobic materials have been produced using a range of chemical and physical methods on rough surfaces, e.g. CA of 174° using n-alkylketene dimer [65], CA of 160° using PECVD of fluoroalkylsilanes on aluminum surface [66] and CA of 162° and CAH less than 2° after being modified with octadecyltrichlorosilane (ODTS) [67]. Quéré states that a water drop can slide off a surface even if the CA is very low, say less than 20° , provided that the CAH is less than $4\text{-}5^\circ$. CAH is defined as the difference between the advancing and receding CAs of water obtained on a surface during the motion of a water drop in one direction [42].

2.4 Review of Nanoparticles incorporated in Silicone Rubber

Silicone rubber high-voltage insulators are superior materials compared to conventional porcelain-based insulators because of their surface hydrophobic properties, light weight and easy handling. That is why they are good candidates to be used under pollution conditions [68] because of their hydrophobic properties which prevent formation of a continuous water film. In the recent years, nanoparticles incorporated polymer nanocomposites have been widely studied for their potential applications in improving the electrical performance of outdoor insulators [68-73]. Silicone rubber has good water repellence characteristics, so insulators made from silicone rubber are able to suppress leakage current. Therefore they have high flashover voltage.

Fillers have gained considerable importance in the polymer industry. They are used to achieve requirements such as higher temperature, and reduced cost. In outdoor insulation applications, fillers such as fumed silica and quartz are used to give silicone rubber good mechanical properties (elasticity, tensile strength, tear strength). Alumina tri-hydrate (ATH) fillers are mainly used to impart the tracking and erosion resistance of silicone rubber [74]. The advantages of nanoparticles incorporation into polymer coatings are obtaining controlled structural properties, increased dielectric constant and improved mechanical properties. Several studies on the structural properties of nanoparticles-incorporated polymers for different applications were reported in the literature [75, 76]. Previous studies indicated that gold nanoparticles incorporated in polymethyl methacrylate (PMMA) can improve the conductivity of the polymer [69]. Similarly, silver nanoparticles along with carbon nanotubes have been added in the polymer to study the effective conductivities of those systems [70]. On the other hand, several other studies are reported in the literature on the dielectric fillers-incorporated polymers [71-73].

One of the commonly used dielectric fillers is barium titanate (BaTiO_3). Choi *et al.* [71] mixed BaTiO_3 nanoparticles (70 nm) in polyimide polymer using two coupling agents between BaTiO_3 nanoparticles and the polyimide, namely, INAAT (isopropyl tris-(N-amino-ethyl aminoethyl) titanate, KR 44) and APTS (3-amino-propyl-triethoxysilane). The authors have shown that the dielectric constant of the BaTiO_3 nanoparticles-polyimide systems increased from 6 to 14 with the increase of BaTiO_3 nanoparticles from 10 to 50 (vol. %) using APTS as a coupling agent. With similar variation of volume proportion of the BaTiO_3 nanoparticles, an increase in dielectric

constant from 7 to 19 has been demonstrated when INAAT was used as a coupling agent. Scanning electron microscopy (SEM) analysis revealed that the distribution of the nanoparticles was uniform when INAAT was used, which was considered as the cause of the increased dielectric constant compared to APTS coupling agent. Similarly, Kobayashi et al. [72] have prepared dielectric thin films of polymer-based materials by incorporating nanometer-sized BaTiO₃ particles in polyvinylidene fluoride (PVDF) and siloxane-modified polyamideimide (SPAI). They found that BaTiO₃ nanoparticles were dispersed more homogeneously in the PVDF film than in the SPAI film. An increase in the BaTiO₃ nanoparticle size from 10.5 to 34.6 nm in the PVDF film at a particle volume fraction of 30 % increased the dielectric constant of the film from 20.1 to 31.8. In their study, the authors reported that the BaTiO₃-PVDF composite film attained high dielectric constant that had more than twice the dielectric constant of the BaTiO₃-SPAI composite film [72]. More work was reported in the literature on controlling the electrical properties of the nanocomposites based on TiO₂ nanoparticles. As an example, Li et al. [74] prepared TiO₂ nanoparticles-incorporated polyarylene ether nitriles (PEN) nanodielectric and found that the dielectric constant (at 1 kHz) of the composite films increased from 4 to 6. However, the electrical breakdown field (E_b) was reduced from 2160 to 1700 kV.cm⁻¹ with the increase of TiO₂ content from 5 wt. % to 20 wt. %. These authors also used FTIR, XRD, XPS, SEM, and other techniques for the structural and chemical characterization of their coatings.

In light of heavy industrial application of nanodielectrics on high-voltage electrical insulators, silicone rubber coatings doped with such powders as carbon black, titania and ceria look very attractive. Silicone rubber based high-voltage insulators are

already in the market, often being already loaded by alumina filler (to improve their mechanical properties and durability) [68, 77, 78]. Doping with carbon black nanopowder is expected to increase surface conductivity of RTV SR-coated insulators, which must lead to higher withstand voltage levels on such modified surfaces. Meanwhile, ceria and titania dopant can improve electrical field distribution along the insulator because these materials possess higher permittivity compared to RTV SR and Al_2O_3 . In parallel, mechanical properties of such nanopowder incorporated RTV SR coatings are also expected to be further improved.

However, new-generation insulators require the improvements of the existing insulator with higher mechanical strength and better electrical performance. Nanoparticles are routinely used as dopants in silicone to improve its mechanical strength. Influence of carbon nanoparticles (100 nm) on both AC and DC conductivity of the epoxy resin has been reported recently [78]. The authors showed that conductivities (AC and DC) increased with the increase in the amount of carbon nanoparticles in the epoxy resin. Carbon nanoparticles-incorporated silicone rubber was used to coat high-voltage porcelain insulator for the flashover study of the ice-covered silicone coated insulators [78]. The coatings behaved as semiconducting glaze and increased the flashover voltage compared to the uncoated porcelain insulators [77]. However, the authors did not provide any information regarding the size of the particles and their dispersion in the polymer.

Although the research on particle-doped RTV silicone rubber coatings is quite extensive [68, 72, 77-79], the information on their water-repellent and ice-releasing properties is very scarce. While RTV silicone rubber (RTV SR) coatings have been

reported to reduce ice accumulation compared to uncoated insulators [77], previous work was mainly focused on electrical and mechanical properties of nanoparticle-incorporated RTV SR coatings. Therefore, in this research work, we aim at studying and better understanding of water and ice-repellent properties of such coatings doped with different nanoparticles.

CHAPTER 3

**EXPERIMENTAL SETUP AND TEST
PROCEDURES**

CHAPTER 3

EXPERIMENTAL SETUP AND TEST PROCEDURES

In this chapter, the methods for preparation of the coatings and the successive characterization involved in this study will be described in detail along with the experimental procedures used. On the basis of the specialized literature on ice adhesion, testing and in order to achieve the objectives, a set of experiments were systematically conducted on the ice-phobic, hydro-phobic and stability of prepared coated aluminum substrates. The coating morphology and performance were also analyzed via applying a set of surface analysis and characterization techniques which are explained in this chapter. This chapter consists of two sub-chapters: sample preparation procedures and sample analysis and characterization including facilities and their principles along with corresponding explanations.

3.1 Process of Coatings' Preparation

Hydrophobic and super-hydrophobic aluminum surfaces were prepared using three following steps:

- (i) Cleaning flat aluminum substrates and producing nano-roughness surfaces;

- (ii) Coating of the cleaned flat as well as nano-rough surfaces with different chemicals; and
- (iii) Characterizing the prepared coated flat and nano-rough aluminum surfaces.

The substrates used were panels of aluminum alloy 6061 (Al 97.9 wt. %, Mg 1.0 wt. %, Si 0.60 wt. %, Cu 0.28 wt. %, Cr 0.20 wt. %) with dimensions of 1.5×1.5 and 5.1×3.2 cm² and with the thickness of ~ 2.5 mm. Prior to coating, they were mechanically polished using first 600-grit sand paper and then consecutively finer SiC abrasive papers lubricated with water, and finally using aqueous 1.0 μ m alumina slurry to have mirror-polished surfaces. The bigger aluminum substrates were used for icing tests (evaluating their ice-repellent performance), while the smaller ones were used to investigate the super-hydrophobic properties of the same coatings. The polished aluminum plates were then cleaned and degreased consequently in different organic solvents ultrasonically that will be discussed in the next below.

3.1.1 Substrate Cleaning

As explained before, prior to coating, the aluminum substrates were washed and degreased in a soap solution, and then were ultrasonically rinsed with methanol (99.8 %, MAT) for 5 minutes and then with acetone (99.5 %, EMD), 5 Minutes, to remove dirt, oil and organic materials. Sample cleaning procedure was followed by

ultrasonication in de-ionized water for 5-10 minutes. Finally, they were blow-dried in a N₂ gas flow follow by drying in an oven at 70 °C for 6 hours to get rid of any water.

3.1.2 Producing Micro-/Nano-Rough Substrates

Surface roughness plays a very important role in attain super-hydrophobic properties. It was explained that the combination of suitable surface roughness and low-surface-energy materials is responsible for super-hydrophobic properties and therefore can result in ice-phobicity. In general, two main approaches have been developed to generate super-hydrophobic surfaces; one is to increase directly the surface roughness of the low-surface-energy materials and the second is fabricating a suitable surface roughness with certain materials or methods (e.g. etching, using nano-particles, etc.) and then to modify the as-prepared surface with low-surface-energy materials. Therefore, substrate chemical etching was used herein to generate micro-/nano-rough substrates.

In this work, a number of well-cleaned and unpolished aluminum panels were immersed in ~ 14.7 wt % aqueous acid hydrochloric (HCl) solution at room temperature for ~1, 2, 3, 4, 5 min to produce rough aluminum surfaces. A chemical reaction between HCl and aluminum can remove some material from the aluminum surface leading to a micro-/nano-rough structure on the surface. After etching, the substrates were rinsed and washed ultrasonically in de-ionized water to remove any remains or loose particles on surface resulting from etching. The etched samples were

dried in a N₂ flow and were dried at 70 °C in an oven and then placed in corresponding solutions.

3.1.3 Preparation of Solution

For this aim, carbon-black nanoparticles (with an average size of 42 nm and surface area of 55 m². g⁻¹), TiO₂ and CeO₂ nanopowders with particle size below 100-150 nm and 25 nm, respectively, were used. The RTV SR was mixed with n-hexane (1:1, 1:2, 1:3, and 1:4 v/v), and then the carbon-black (1.5 and 3 wt. %), TiO₂ (1 and 2 wt. %) or CeO₂ (1 and 2 wt. %) nanoparticles were added under vigorous magnetic agitation. Upon carefully stirring following 10 minutes stirring ultrasonically to facilitate the preparation of homogeneous mixtures, the suspensions were used to prepare several series of nanoparticle-incorporated coatings on either polished (flat) or etched aluminum metal.

3.1.4 Coating of the Samples

The cleaned flat and micro-/nano-rough aluminum samples were coated by using a spin-coater. Spin coating is a commonly used technique for preparing uniform thin films on flat substrates which involves the controlled precipitation from solution of a compound on a suitable substrate while spinning with specific parameters. The spinning rate was set at 500 rpm (5 s) and 3000 rpm (20 s) for the first and second

stages, respectively. Upon coating, all samples were heat-treated at 70 °C in air overnight to remove residual solvents.

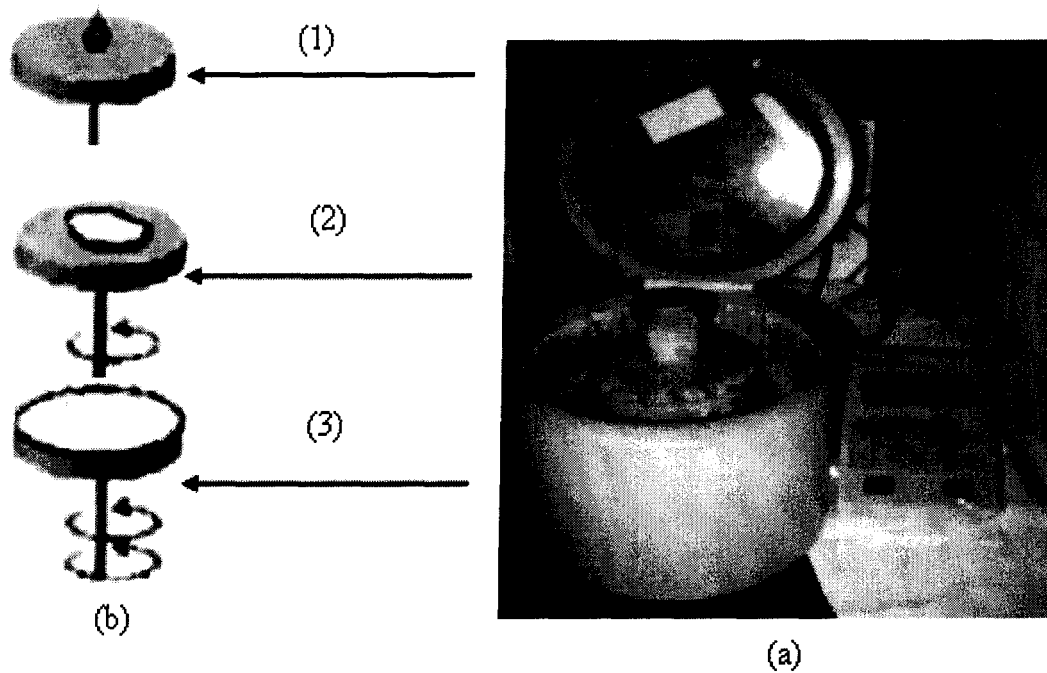


Fig. 3.1. (a) The spin-coater (model WS-400B-6NPP, Laurell Technologies Corporation), (b) steps of coating preparation, (1) deposit solution, (2) spreading (low speed spin), (3) high speed spin.

Figure 3.2 is a general schematic presentation of sample preparation procedure used in this research work. Among several methods available to coat cleaned flat and micro-/nano-rough aluminum alloy substrates, cast films using spin coating was selected in this work as the main coating method for bringing the coating's solutions including nanoparticles on the substrate surfaces. All these steps can be observed in details in this flowchart.

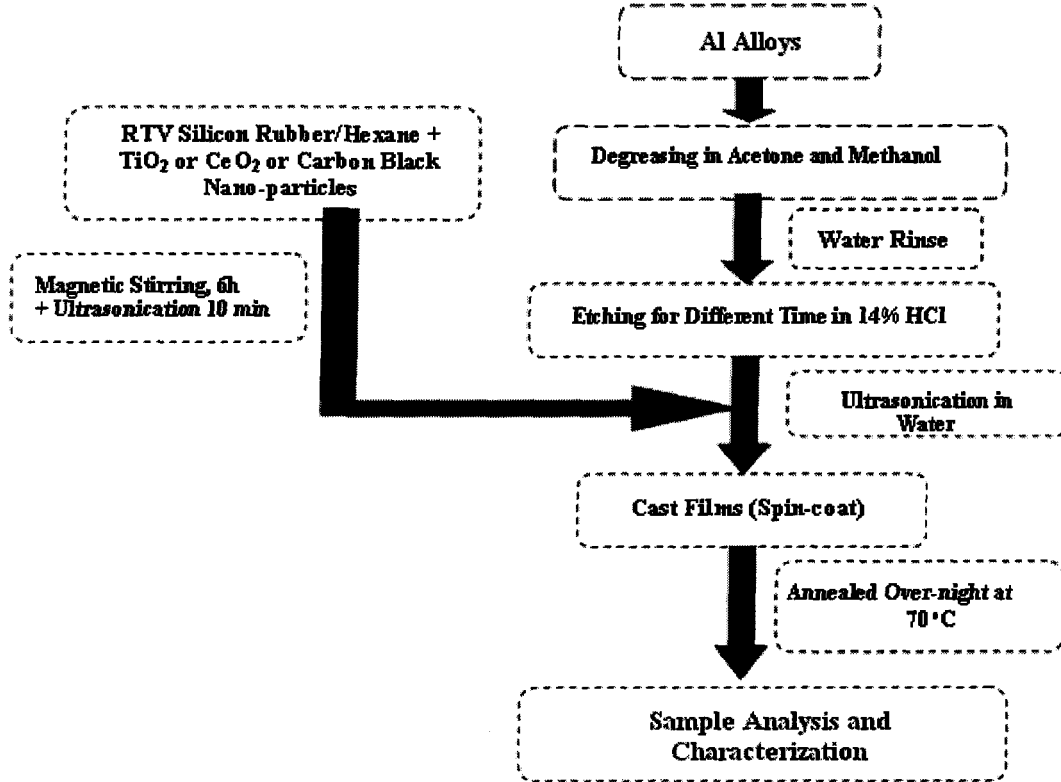


Fig. 3.2. Scheme of preparation of nano-powder incorporated RTV SR coatings on rough substrates.

3.2 Sample Analysis and Characterization

3.2.1 Morphological Characterization

In this research, morphological characterizations and analysis were carried out using an atomic force microscope (AFM, Escope, Veeco) and a scanning electron microscope with energy-dispersive X-ray spectroscopy (SEM/EDX) (Hitachi S-4700 Field-Emission SEM with accelerating voltages from 500 V to 25 kV).

1) Atomic Force Microscope (AFM)

An atomic force microscope was used to study and characterize the surface roughness and surface morphologies of the coated samples. The method used to generate the three dimensional (3-D) images via atomic force microscope was tapping mode at room temperature under normal air pressure. In this mode, a swing silicon probe (Nanosensors™) design an image in the topography of the surface (e.g. in the scan size of 20x20 μm^2 in this study). 3-D surface topography was mapped by lightly tapping the surface with an oscillating probe and thus imaged with monitoring of the changes in the cantilever's oscillation amplitude while scanning the surface. Atomic force microscopy gives various information of the surfaces features. For instance, the dimension of the nanoscale features of the surfaces including the z-height and surface roughness. Tip radius is less than 10-15 nm and height 10-15 μm set on a cantilever of length 220-230 μm and width 35-45 μm , respectively.

2) Scanning Electron Microscopy (SEM/EDX)

SEM measurements produce a two dimensional images of the morphological features of the surface in addition to providing the atomic composition of the material by means of energy dispersive X-ray spectroscopy (Hitachi S-4700 Field-Emission SEM with accelerating voltages from 500 V to 25 kV). Before each measurement, samples with low surface conductivity were covered with a very thin film of platinum or carbon to lessen charge build-up during the scanning.

3.2.2 Wettability Tests

3.2.2.1 Contact Angle Measurement at Room Temperature

The wetting behaviour of the prepared coatings was assessed on a contact-angle goniometer following standard procedures (Fig. 3.3) by measuring the water contact angle. The system used for contact angle measurements is a drop shape analyzer system (DSA 100 from Krüss GmbH Co.). Contact angles were measured using the sessile-drop method: small water droplets (4 μL in volume) were quietly placed on the surface by injection mechanism with several convenient syringes. Then, their shape was evaluated with the goniometer optics and software using a light source to light the sample surface and a camera connected to a computer where the drop shape can be recorded and analyzed. Using the associated software also can select any of the syringes and manage its situation and inoculation rate. Another important advantage of the software is to calculate the contact angles by using appropriate techniques. The static contact angle data were obtained by fitting the symmetric water drops using the Laplace-Young equation and the advancing (θ_a) and receding (θ_r) contact angles to calculate contact angle hysteresis (in case of super-hydrophobic samples) were measured on the asymmetric water drops using the tangent-2 method (Fig. 3.4). After injection a water droplet on the sample, the droplet was held in contact with the sample surface with stationary needle in it. Then, the advancing and receding contact angles to evaluate the value of contact angle hysteresis were measured while moving the sample in one direction. After settling the water droplet on the sample surface, it is necessary to

wait for 10 s prior to each measurement to be sure that the droplet is stabilized. The contact angle values reported here were the averages of at least five measurements on various parts of each sample.

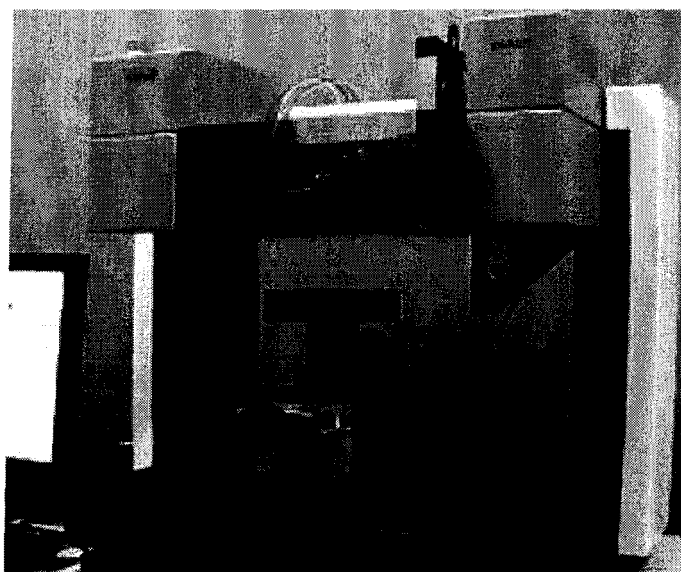


Fig. 3.3. Kruss DSA100 contact-angle goniometer.

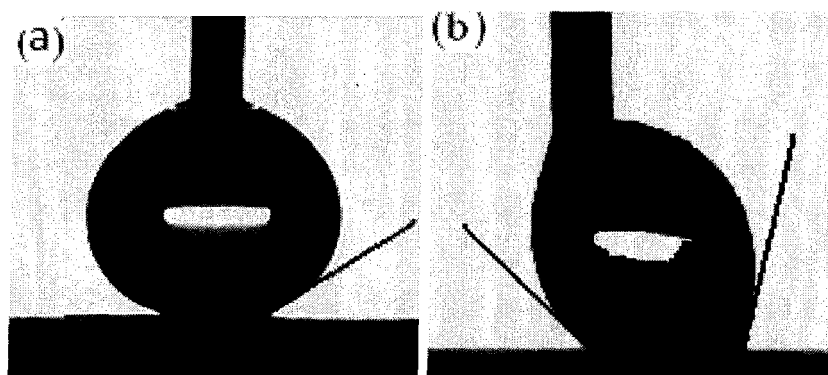


Fig. 3.4. Measuring the advancing and receding contact angles on a sample with (a) a low hysteresis (static CA), and (b) a high hysteresis (advancing (θ_A) and receding (θ_R) CAs).

3.2.2.2 Contact Angle (CA) Measurement at Low Temperature

Hydrophobic properties of the prepared coatings were also investigated by measuring water contact angles at sub-zero temperature ($-15\text{ }^{\circ}\text{C}$). For this purpose, some coated aluminum samples were placed in a cooling unit (Peltier device) with a specially designed chamber that can be replaced on the goniometer stage. It has sealed walls and windows, and a thermoelectric heating/cooling part at the bottom filled with ethylene glycol (EG), it is possible to adjust the temperature of Peltier element over a wide temperature range of $-30\text{ }^{\circ}\text{C}$ to $+120\text{ }^{\circ}\text{C}$. The cooling unit is shown in Fig. 3.5.

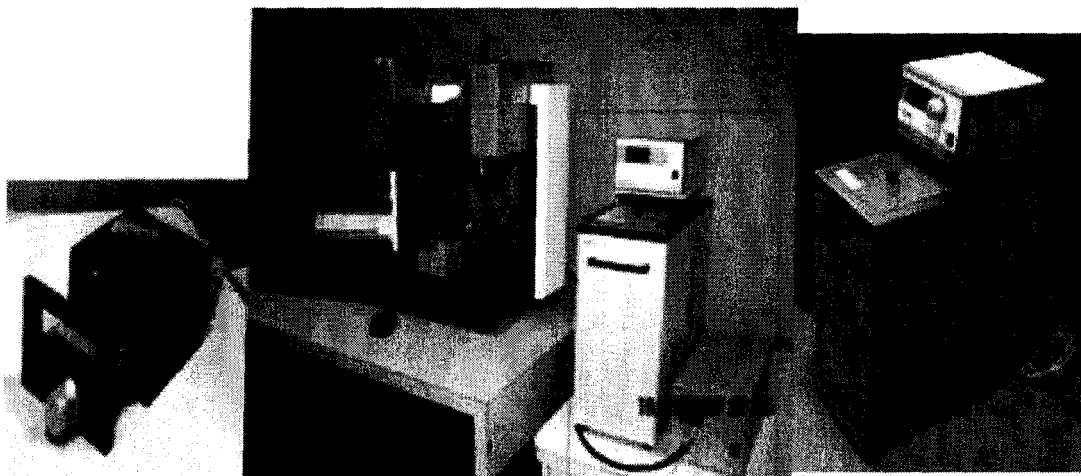


Fig. 3.5. Contact-angle goniometer and cooling unit for measuring CA at low temperature (centre), enlarged Peltier device (left) and cooling/heating system (right).

The experiment was carried out as follows: a sample was located in the Peltier device with the set point of its controller (TC40) at $-15\text{ }^{\circ}\text{C}$. Then a water drop of $\sim 4\text{ }\mu\text{L}$ was placed on the cold sample and the needle was removed and the process of contact

angle measurement started. By cooling down of the samples the placed water droplet on the sample was frozen completely in few minutes. However, the freezing time varied depending on the different prepared coated samples. The reasons of these observations will be explained in the next chapter.

3.2.2.3 Ice Adhesion Test

Different methods have been developed to measure ice adhesion; but, some of them are not applicable for the atmospheric ice formed by the freezing of the super-cooled water drops in contact with structures. Ice adhesion strength depends on the techniques used to ice adhesion measurement. In these series of experiments, the ice accumulation conditions were generated in the CIGELE laboratories. The ice-adhesion evaluation tests were conducted on aluminum beams with samples spun in a home-made centrifuge apparatus (see Fig. 3.6). The samples, attached to the beams, were iced in a wind tunnel at a wind speed of 10 m s^{-1} , temperature $-10 \text{ }^\circ\text{C}$, water feed rate of 2.5 g m^{-3} , and average droplet size of $\sim 80 \text{ }\mu\text{m}$ to prepare glaze ice of $\sim 1 \text{ cm}$ thick over the area of $\sim 5.1 \times 3.2 \text{ cm}^2$ [80]. This ice geometry was found to be optimal to provide adhesive failure of the ice and provide well reproducible results during de-icing. The samples investigated were placed in a wind tunnel at subzero temperature to accumulate glaze ice because the subzero tests need to be performed in a cold environment in order to study how ice growth on prepared coated surfaces. The wind tunnel used was adjusted thoroughly under conditions similar to those in nature leading to accretion of glaze ice during freezing rain.

Ice mass and area were carefully evaluated both after icing and de-icing. To balance the beam in the centrifuge, a counter-weight was used on the opposite side (Fig. 3.6b). The centrifuge test machine can increase rotation speed of the beam from 0 to 10000 rpm with an acceleration of approximately 300 rpm s^{-1} . Rotation generates a centrifugal force and when this force is larger than adhesion force of ice, the ice detaches from the sample. The artificially iced samples were spun in the centrifuge placed in a climatic chamber at -10°C to determine the rotational speed at which ice detachment from the sample surface occurs. At the moment of detachment (detected with sensors embedded into the centrifuge wall), the adhesion strength of ice is assumed to be equal to the centrifugal force, $F = mr\omega^2$, where m is the ice mass, r is the beam radius and ω is the rotational speed in rad s^{-1} . The shear stress, correspondingly, was calculated as $\tau = F/A$, where A is the de-iced area. Bare mirror-polished aluminum was used as a standard reference sample, demonstrating the shear stress of ice detachment on its surface of $350 \pm 19 \text{ kPa}$ and agreeing with values found in the literature [81].

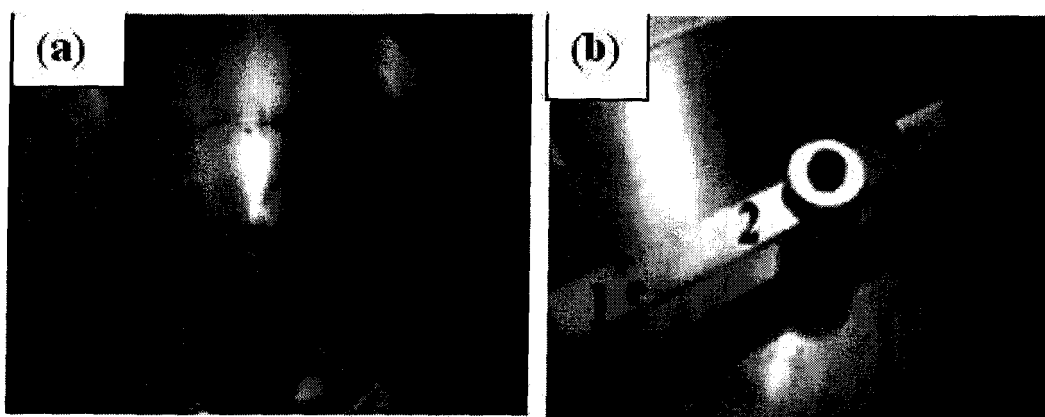


Fig. 3.6. (a) Centrifuge system. (b) sample with coating (1) in centrifuge set-up evaluating ice adhesion strength. (1) sample, (2) aluminum beam, (3) counter-weight.

The effect of controllable wind tunnel parameters such as temperature, air speed and liquid water content were considered. The atmospheric icing wind tunnel used was based on room temperature water injection through warm nozzles into a cold air stream provided by three nozzles on the spray line.

Figure 3.7 shows the samples during ice accumulation in a wind tunnel. The distance between the nozzles and the samples was chosen long enough to reach thermodynamic equilibrium for all sprayed droplets in the wind tunnel [82-84]. After ice accumulation was completed, the samples were removed, weighed and kept in a climatic chamber at -10 °C. The weight of accumulated ice on the coated samples and the sample surface area covered with the ice were measured before and after each icing/de-icing for all samples. It should be noted that all samples were placed in the tunnel for roughly about 8 to 15 min to be cooled down prior to each icing test. The time period needed to have about 4-6 g (up to ~1 cm thick) of ice on each sample was also traced.

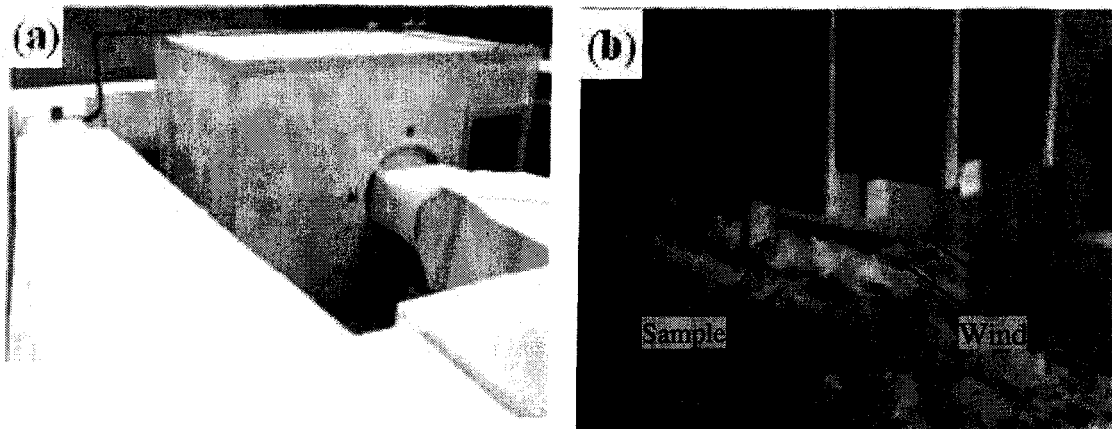


Fig. 3.7. (a) Top view of atmospheric icing wind tunnel used, and (b) a view of ice accumulation procedure on coated samples in wind tunnel.

CHAPTER 4

EXPERIMENTAL RESULTS AND DISCUSSION: HYDROPHOBIC AND SUPER-HYDROPHOBIC PROPERTIES OF FLAT AND ROUGH SAMPLES WITH COATINGS ALUMINUM SUBSTRATE

CHAPTER 4

EXPERIMENTAL RESULTS AND DISCUSSION: HYDROPHOBIC AND SUPER-HYDROPHOBIC PROPERTIES OF FLAT AND ROUGH SAMPLES WITH COATINGS ALUMINUM SUBSTRATE

In this chapter the water droplets behaviour on RTV SR coatings incorporated with carbon-black (CB), TiO₂ and CeO₂ nanopowders and prepared by spin-coating RTV SR/hexane solutions with volume ratios of 1:1, 1:2, 1:3 and 1:4 on the flat and rough aluminum substrates is described and discussed. It should be noted that RTV SR coatings (prepared from a RTV SR / hexane mixture with the ratio of 1:4) on flat and rough aluminum substrates were used as reference samples demonstrating contact angle of ~110° and ~143°, respectively.

4.1 Water Droplet Contact Angle on Flat Al Substrates

4.1.1 Carbon-Black Nanoparticle-Incorporated RTV SR Coatings

The contact angle of RTV SR coated samples as a function of volume percent of carbon-black nanoparticles incorporated is shown in Fig. 4.1c. Figures 4.1a and 4.1b compare water droplets on the non-doped and doped RTV SR surfaces. Compared to

the non-doped coating, an increase (by $\sim 7-8^\circ$) of contact angle is observed on the doped samples as the carbon-black concentration is raised (see Fig. 4.1c). This increase is believed to be associated with greater surface roughness of the coatings incorporated with carbon-black nanoparticles, as showed in Fig. 4.2. The results presented in Fig.4.1c therefore lead to the conclusion that, in agreement with the previous report of Liao et al. [77], no significant effect of carbon-black incorporation on the wetting properties of the coatings was observed.

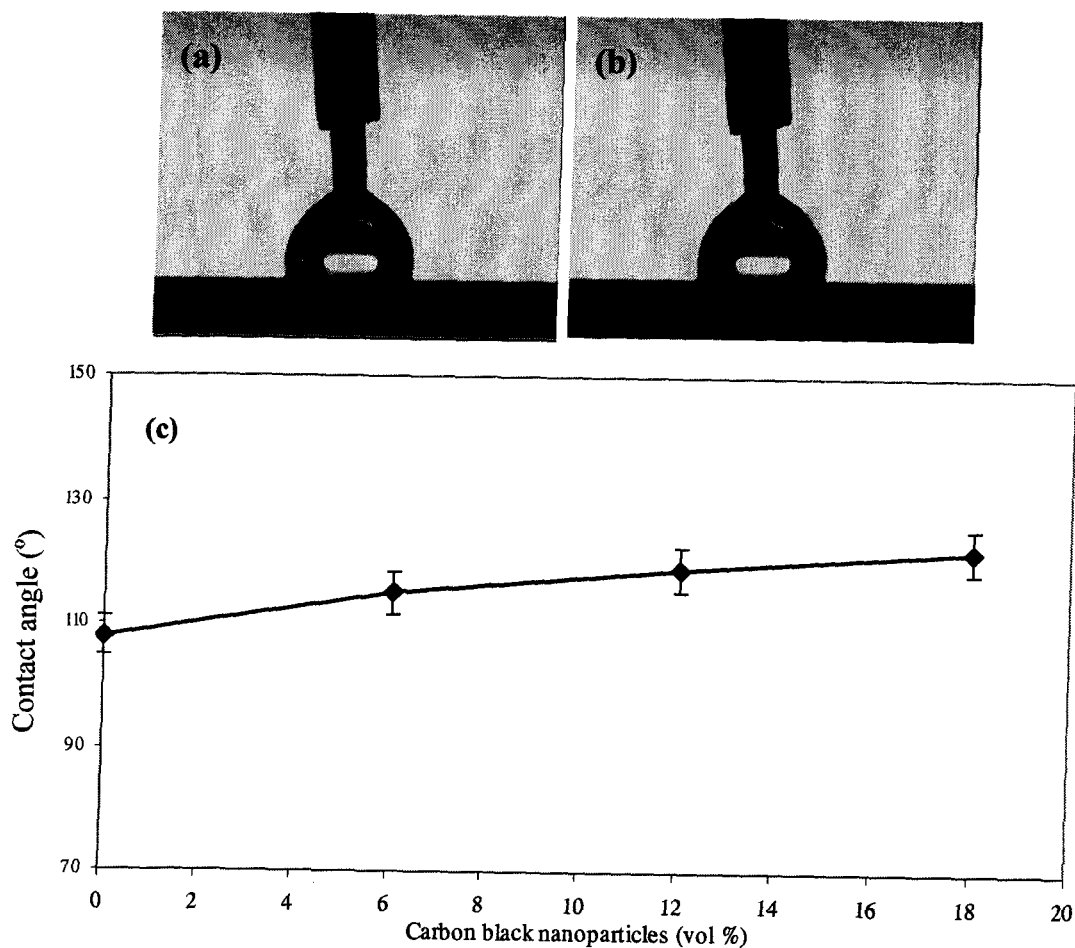


Fig. 4.1. (a) Water drop on pure (non-doped) RTV SR coating, (b) water drop on RTV SR/hexane (1:1 v/v) coating with 6 vol. % of carbon-black nanoparticles incorporated, (c) contact angle vs. vol. % of carbon-black incorporated into coatings.

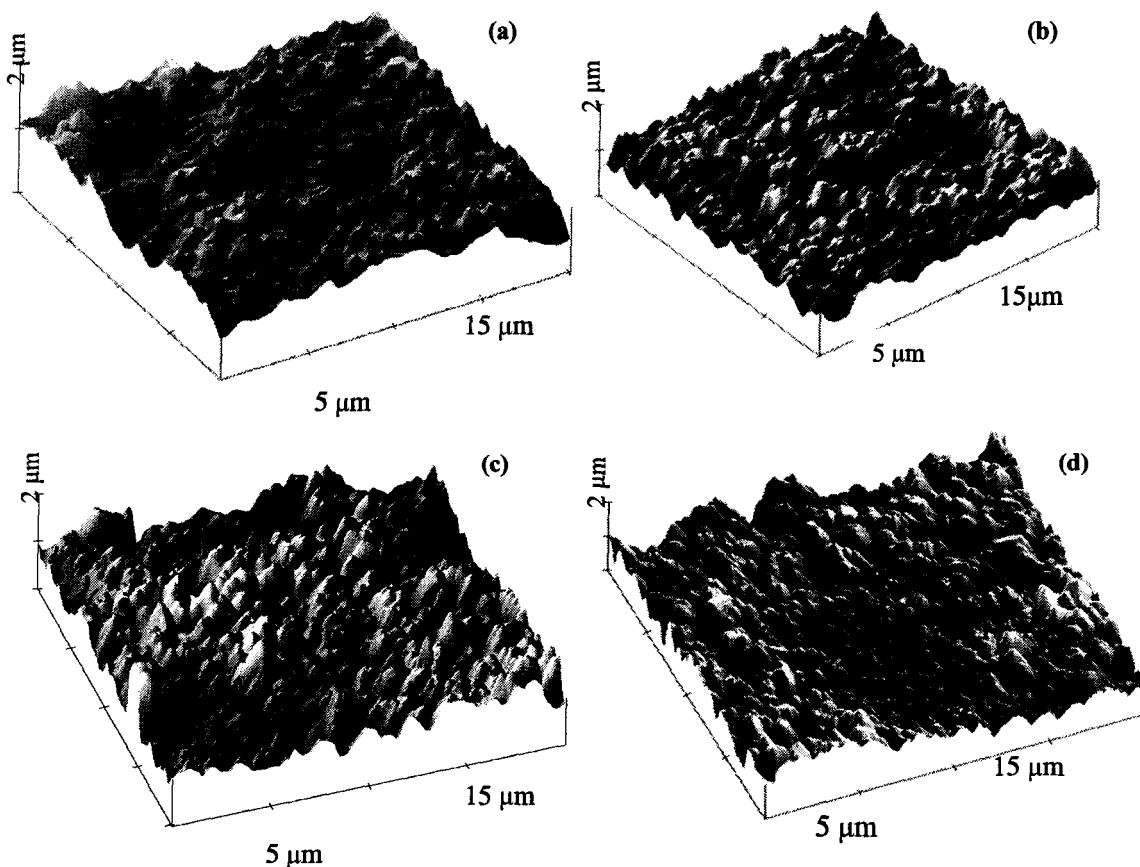


Fig. 4.2. AFM surface images of RTV SR coatings doped with 0 (a), 6 (b), 12 (c), and 18 vol. % (d) of carbon-black.

Figure 4.2 shows AFM surface images of the samples. Figure 4.2a shows that the surface topography of the non-doped RTV SR coating is mainly dictated by alumina micro-powder (which is a common filler in commercial silicone rubbers). Such particles (with size of $\sim 3 \mu\text{m}$) are seen in Fig. 4.2a to form a relatively flat coating with a hydrophobic top layer. It is clear from the images in Figure 4.2 that, as the volume percentage of carbon-black dopant in the RTV SR rises, the surface roughness also

increases slightly, resulting in enhanced root-mean-square roughness (R_q) values of the surfaces. The root-mean-square roughness values were calculated to be 128.2, 178.11, 261.93, and 295.81 nm for the samples doped with 0, 6, 12, and 18 vol. % of carbon-black, respectively. This increase in surface roughness is related to the incorporation of carbon-black nanopowder.

4.1.2 TiO₂ Nanoparticles-Incorporated RTV SR Coatings

Flat Al substrates (aluminum alloy AA 6061) were coated by spin-coating an RTV SR/hexane solution (1:3 v/v) with different concentration of TiO₂ nanoparticles-incorporated (2, 4, 8 wt. %). Fig.4.3 shows the CA and CAH of coatings prepared from the RTV SR/hexane (1:3 v/v) suspension spin-coated on flat Al as a function of different percentage of TiO₂ nanopowder incorporated. It can be also concluded in Fig. 4.3 that even though the as-supplied RTV SR was loaded by micro sized alumina powder, doping it with nano-sized TiO₂ powders does change the hydrophobic properties of the prepared coatings. It is evident from Figure 4.3 that by changing TiO₂ concentration, RTV SR coatings with improved hydrophobicity could be prepared. The contact angle values are seen to increase from $\sim 135^\circ$ to $\sim 138^\circ$ while the values of CAH decreased from $\sim 35^\circ$ to $\sim 25^\circ$. Similar results were obtained with CeO₂ powder as a dopant. It was difficult to prepare super-hydrophobic coatings on flat substrates. Therefore, further attempts were mainly focused on rough etched aluminum substrates.

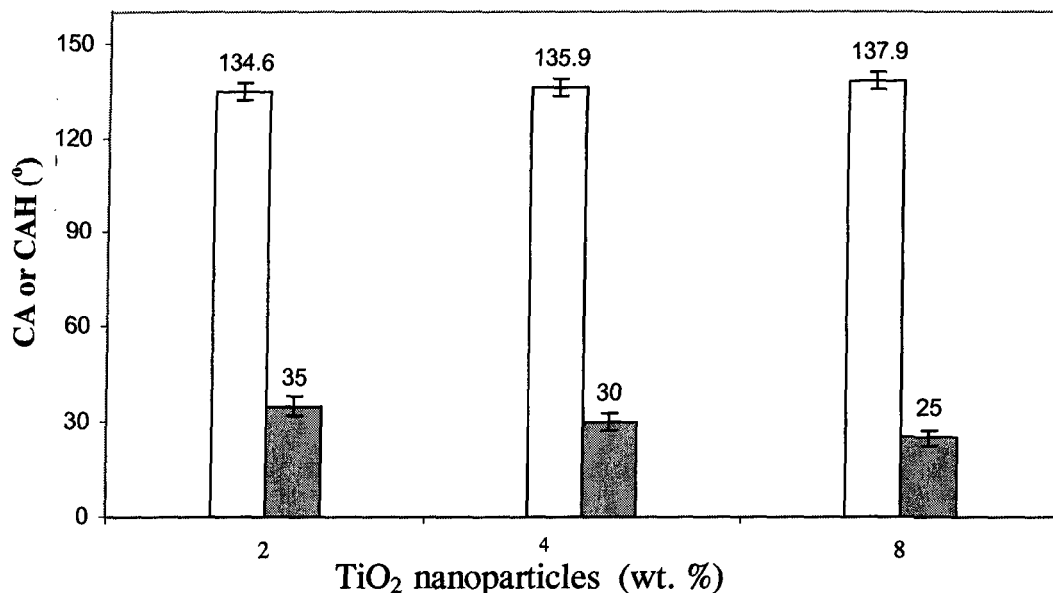


Fig. 4.3. Contact angle (white) and CAH (gray) as a function of TiO₂ concentration in coatings prepared by spin-coatings RTV SR/hexane ratio (1:3 v/v) suspension on flat Al.

4.2 Water Droplet Contact Angle on Rough Aluminum Substrates

The same experiments and investigations were carried out on rough etched aluminum substrates by applying different concentration of carbon black nanoparticles incorporated (1.5 and 3 wt. %), TiO₂ (1 and 2 wt. %) and CeO₂ (1 and 2 wt. %). The contact angle and CAH values of the above mentioned coated Al samples as a function of dilution of RTV SR with hexane were measured showing similar behaviour and tendency in decrease/increase of the contact angle (CA) and contact angle hysteresis (CAH) values on the prepared samples surfaces.

4.2.1 TiO₂ Nanoparticles-Incorporated RTV SR Coatings

Fig. 4.4 and Fig. 4.5 demonstrate CA and CAH values of RTV SR coated samples with 2 wt. % of TiO₂ incorporated as a function of etching time (min) of the Al substrate. From these figures, it is evidently clear that CA values of these coated samples increase while the etching time rises from 1 to 5 min. On the other hand, their CAH values decrease gradually. This can be explained by gradually increased substrate roughness. As the etching is well known to lead to increased roughness of the substrates, the suspension used for spin-coating covered the rough surface resulting in high values of CA ranging from $\sim 115^\circ$ (1 min etching) to $\sim 140^\circ$ (5 min etching). It is believed that the samples with shorter etching time were wetted in the Wenzel regime (high CAH) while only the samples etched for longer times were likely to gradually switch to the Cassie-Baxter wetting mode.

This assumption agrees with the gradually decreasing CAH values observed in Fig. 4.5. As the lowest value of CAH obtained in this series was still relatively high ($\sim 15^\circ$, see Fig. 4.5), we conclude that the RTV SR/hexane solution with the volume ratio 1:1 was too viscous and filled in the rough valleys between substrate asperities, leading to relatively shallower rough coatings. This is also confirmed by the results presented in Fig. 4.6-Fig. 4.11, where further dilution of RTV silicone rubber with hexane leads to both increased contact angle and decreased contact angle hysteresis values of coating incorporated with different nanoparticles.

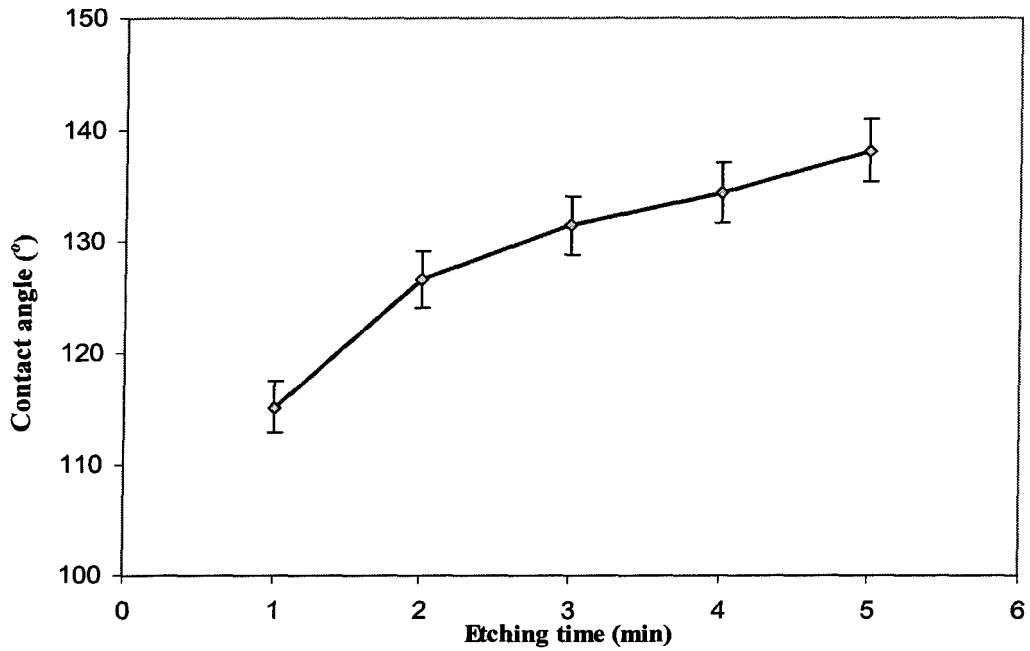


Fig. 4.4. Contact angle of samples prepared by spin-coating RTV SR/hexane (1:1 v/v) suspension with 2 wt. % of TiO₂ nanoparticles incorporated as a function of etching time of the substrate used.

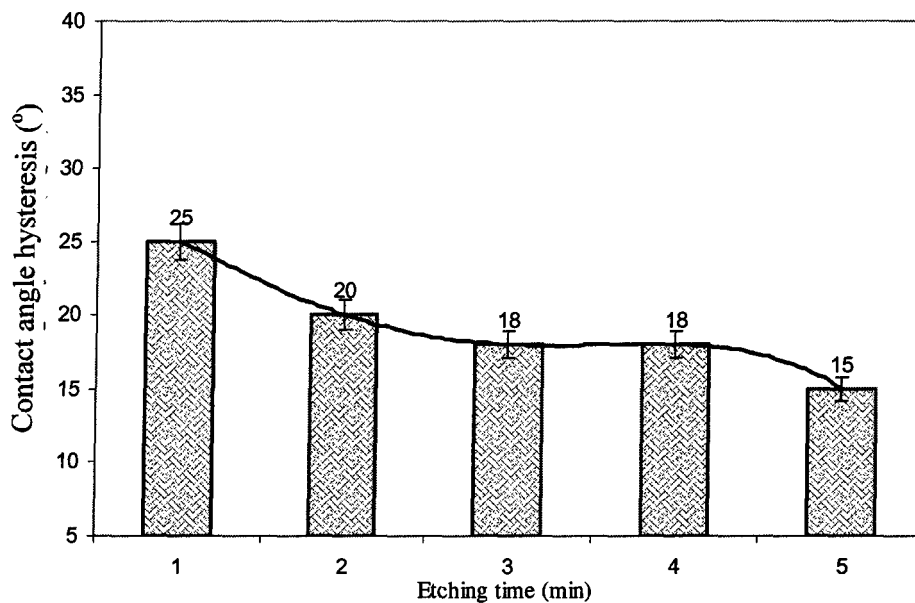


Fig. 4.5. Contact angle hysteresis of coatings prepared from (1:1 v/v) RTV SR/hexane solution with 2 wt. % of TiO₂ nanoparticles incorporated as a function of etching time of the substrate (Al alloy in diluted HCl).

4.2.2 Carbon-Black Nanoparticles-Incorporated RTV SR Coatings

The contact angle values of RTV SR coated samples as a function of dilution of RTV SR with hexane mixed with 3 wt. % of carbon black nanoparticles incorporated are shown in Fig.4.6. The rough Al substrates used were etched in 14% HCl for 5 min prior to spin-coating the carbon black-RTV SR suspension.

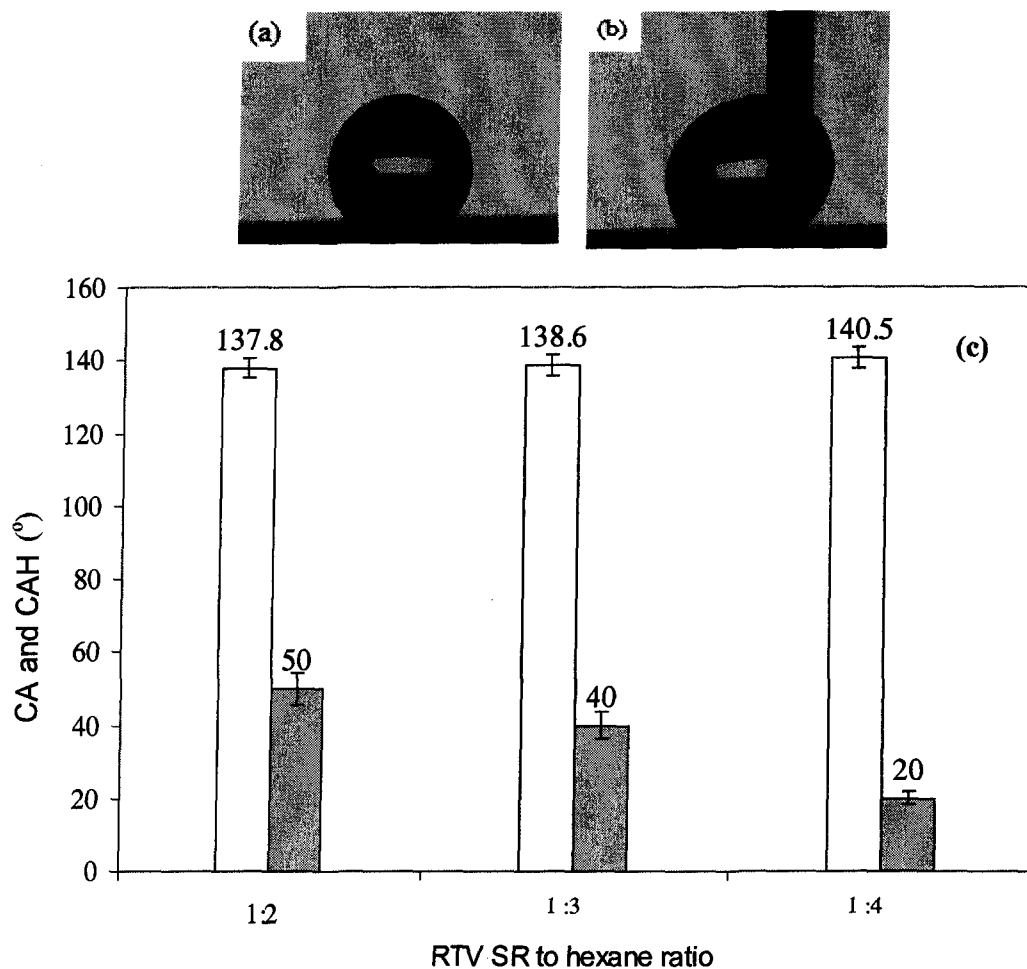


Fig. 4.6. (a) Water contact angle (CA) and (b) water contact angle hysteresis (CAH) of coating prepared by spin-coating hexane dilution of RTV SR (1:4) with 3 wt.% carbon black nanoparticles incorporated, (c) contact angle (white) and CAH (gray) as a function of different concentration of RTV SR with 3 wt.% of carbon black nanoparticles incorporated.

It is seen in Fig. 4.6 and Fig. 4.7 that surfaces with CA $\sim 140^\circ$ could be prepared by spin-coating carbon black-RTV SR suspension (with both 1.5 and 3 wt. % of carbon black) on etched Al substrates. While CA values are almost unchanged for all six samples, their wetting hysteresis could be varied by changing both carbon black concentration and RTV SR dilution. The lowest value of contact angle hysteresis (CAH) of $\sim 20^\circ$ was achieved for the sample with 3 wt. % of carbon black and RTV SR in hexane; 1:4 (v/v).

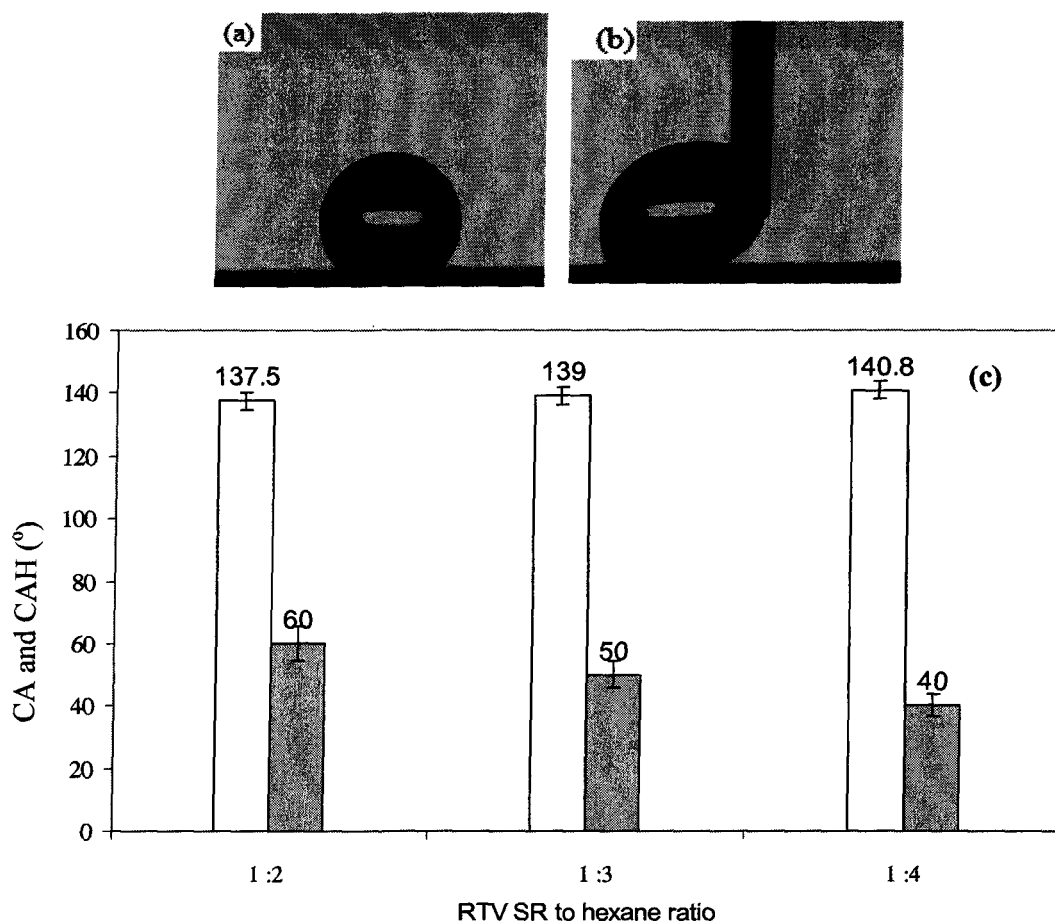


Fig. 4.7. (a) Water contact angle (CA) and (b) water contact angle hysteresis (CAH) of coating spin-coated from hexane dilution of RTV SR (1:4) with 1.5 wt.% carbon black nanoparticles incorporated, (c) contact angle (white) and CAH (gray) as a function of hexane dilution of RTV SR with 1.5 wt.% of carbon black nanoparticles incorporated.

4.2.3 TiO₂ Nanoparticles-Incorporated RTV SR Coatings

The same studies were carried out by applying different concentration of TiO₂ (1 and 2 wt. %) and RTV SR/hexane solutions with different ratios. Fig. 4.8 and Fig. 4.9 presents the contact angle values of RTV SR coated samples as a function of dilution of RTV SR with hexane mixed with 1 and 2 wt. % of TiO₂ nanoparticles.

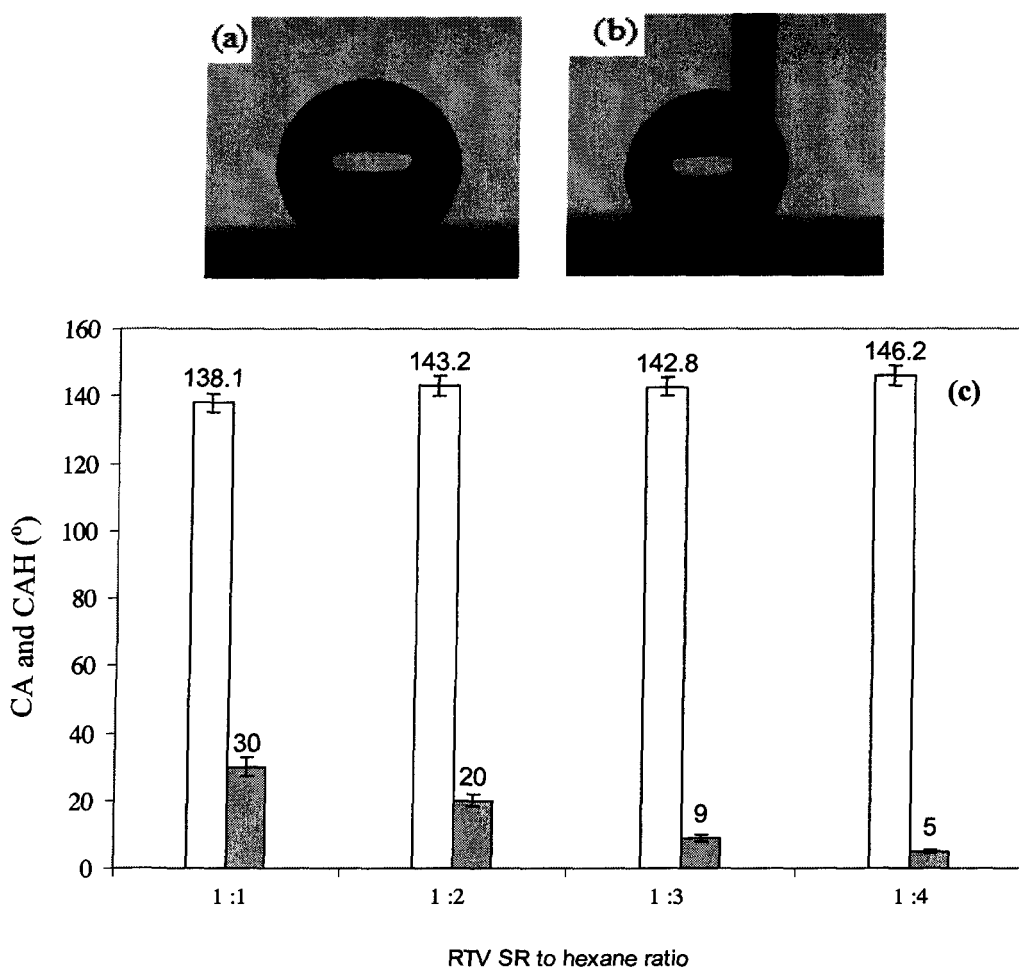


Fig. 4.8. (a) Water contact angle (CA) and (b) water contact angle hysteresis (CAH) of coating prepared by spin-coating hexane dilution of RTV SR (1:4) with 1 wt.% TiO₂ nanoparticles incorporated, (c) contact angle (white) and CAH (gray) as a function of RTV SR/hexane ratio with 1 wt.% of TiO₂ nanoparticles incorporated.

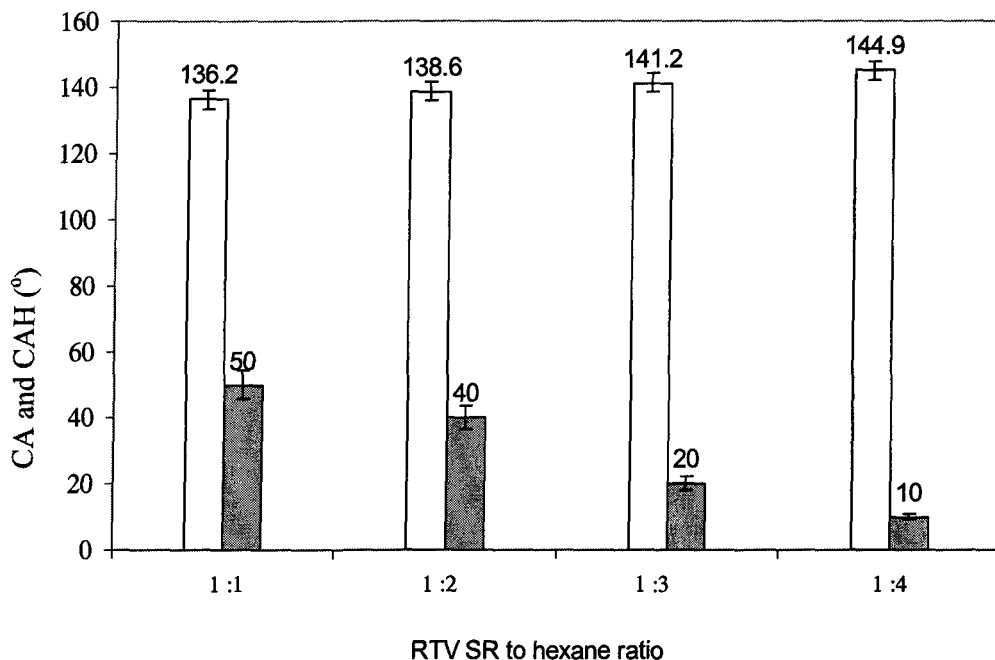


Fig. 4.9. Contact angle (white) and CAH (gray) as a function RTV SR/hexane volume ratio with 2 wt. % of TiO_2 nanoparticles incorporated.

Fig. 4.8 and Fig. 4.9 demonstrate that by changing RTV silicone rubber/hexane ratio from 1:1 to 1:4, the samples prepared by spin-coating RTV silicone rubber suspensions with both 1 and 2 wt. % of TiO_2 showed contact angle values gradually increasing with the RTV silicone rubber dilution degree. At the same time contact angle hysteresis values of the samples decreased and could reach as low as $\sim 5\text{-}10^\circ$, which is characteristic of super-hydrophobic state. Thus, super-hydrophobic samples with $\text{CA} > 145^\circ$ and $\text{CAH} \sim 5\text{-}10^\circ$ could be prepared by spin-coating TiO_2 -loaded RTV silicone rubber suspensions on etched substrates. Fig. 4.8b shows that water droplets could move on such surfaces without any significant distortion (i.e. demonstrating low CAH values).

4.2.4 CeO₂ Nanoparticles-Incorporated RTV SR Coatings

Fig. 4.10 and Fig. 4.11 show that similar results were obtained when CeO₂ incorporated RTV SR coatings were spin-coated on rough etched Al substrates.

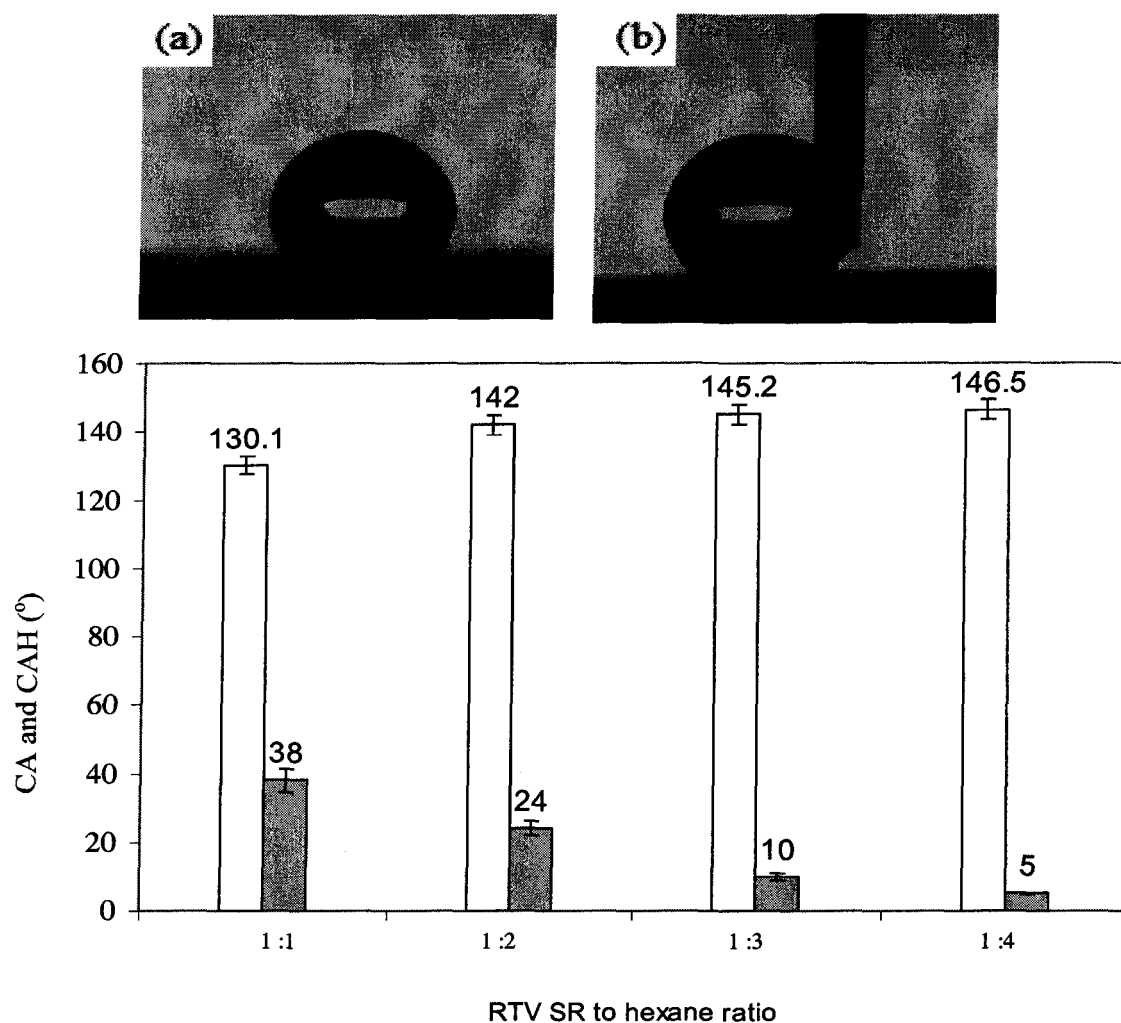


Fig. 4.10. (a) Water contact angle (CA) and (b) water contact angle hysteresis (CAH) of coating prepared by spin-coating hexane-diluted RTV SR mixture (1:4) with 1 wt.% CeO₂ nanoparticles incorporated, (c) contact angle (white) and CAH (gray) as a function of RTV SR/hexane ratio with 1 wt.% of CeO₂ nanoparticles incorporated.

Again, as RTV silicone rubber in the spin-coated suspension is more diluted with hexane, the coatings (both with 1 and 2 wt. % CeO₂) demonstrate higher values of CA (as high as ~147°) and lower values of CAH (as low as ~5-6°), which is characteristic of super-hydrophobic surfaces. Thus, similar to the above discussed RTV SR coatings with TiO₂ nanopowder, their counterparts incorporated with CeO₂ could also be prepared with super-hydrophobic properties.

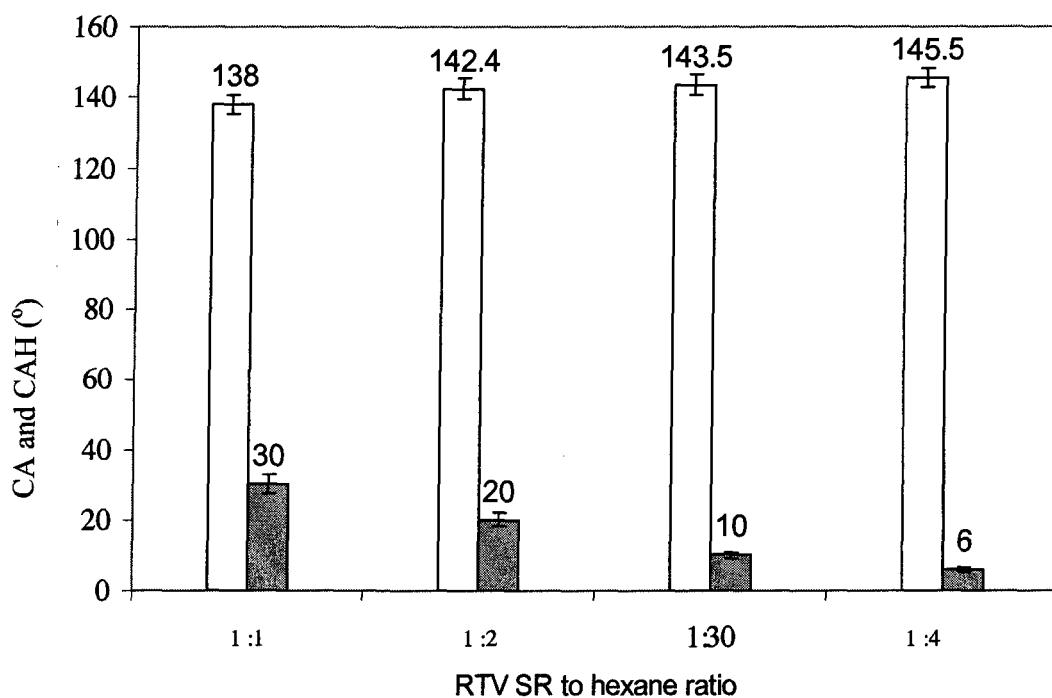


Fig. 4.11. Contact angle (white) and CAH (gray) as a function of RTV SR/hexane volume ratio with 2 wt. % CeO₂ nanoparticles incorporated.

Water droplets could move along such surfaces with only slight distortion (see Fig. 4.10b). Though all rough RTV SR coatings doped with carbon-black, CeO₂ and TiO₂ powders were believed to have silicone rubber layers atop (covering dopant particles), the surface topographies in case of TiO₂ and CeO₂ doped coatings were more favourable for super-hydrophobicity. Further optimisation of coating parameters is

likely to lead to super-hydrophobic surfaces in case of carbon-black doped coatings as well. As it is evident in all previous figures, obvious significant increase in the contact angle values of the samples was obtained when the prepared suspensions were diluted three or four times. Significant decrease by 10 to 20° was also observed in the obtained contact angle hysteresis values. This can be explained by better filling of valleys between surface asperities (on rough substrates) by thinner suspensions during spin-coating. As a result, rough surfaces with asperities well covered with RTV silicon rubber and deeper valleys were produced, which are wetted in the Cassie-Baxter mode (i.e. with high contact angle and low contact angle hysteresis values).

4.3 Surface Characterization

4.3.1 Scanning Electron Microscopy (SEM)

Figure 4.12 to Figure 4.14 show the scanning electron microscopy (SEM) images, as well as the corresponding EDS spectra of etched substrate and rough samples coated with RTV SR/TiO₂, RTV SR/CeO₂. These series of experiments were conducted to investigate surface morphology and chemical composition of surfaces. The peaks of O, Fe, Mn, Si and C refer to the second-phase particles on aluminum surface and surface contaminations as well. The peaks corresponding to Ce and Ti elements can be observed in Figs. 4.13 and 4.14 which imply existing RTV silicon rubber coating layer with TiO₂ or CeO₂ particles incorporated on Al surface. The strong Si peaks in Figs. 4.13 and 4.14 belong to the RTV silicon rubber coatings (there is no similar peak in Fig. 4.12).

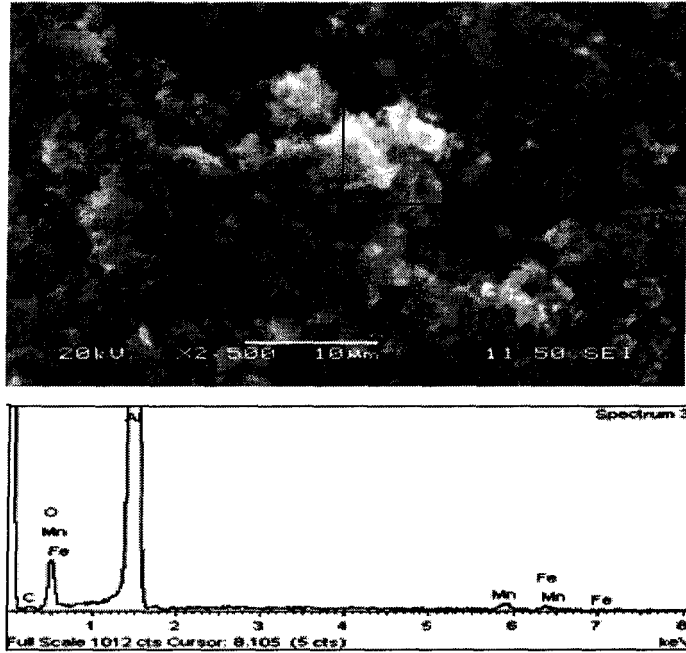


Fig. 4.12. SEM surface image and EDS spectrum of etched aluminum sample.

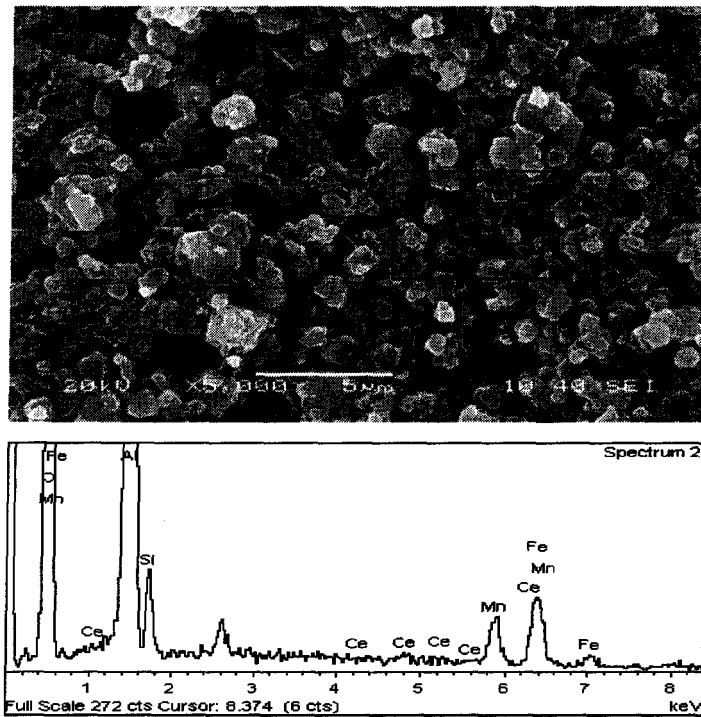


Fig. 4.13. SEM surface image and EDS spectrum of aluminum sample coated with RTV (1:4 v/v) / CeO_2 (2 wt. %).

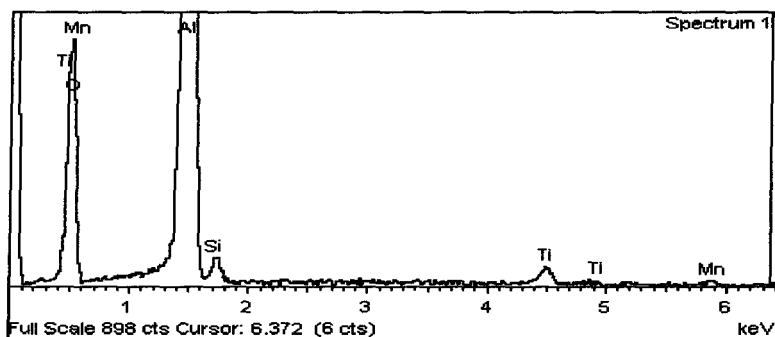
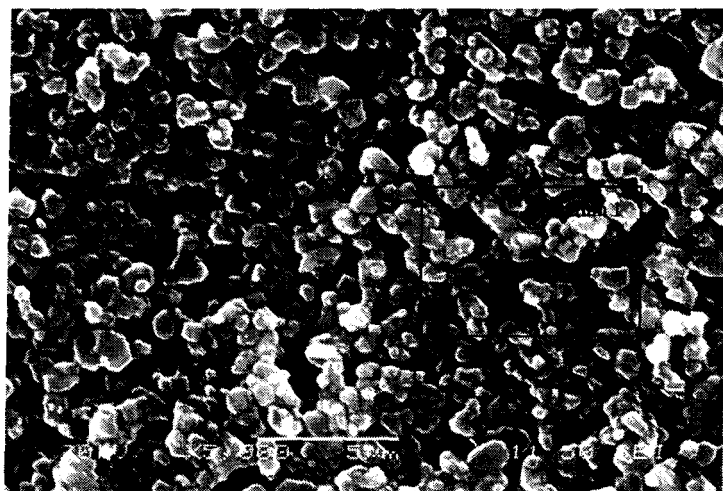


Fig. 4.14. SEM surface image and EDS spectrum of aluminum sample coated with RTV (1:4 v/v) /TiO₂ (2wt. %).

Also scanning electron microscopy (SEM) images from flat aluminum sample coated with RTV silicon rubber/hexane (1:4 v/v), etched aluminum sample coated with RTV silicon rubber/hexane (1:4 v/v) and as-received aluminum sample are shown in Figs. 4.14 - 4.17. Based on the SEM images obtained from different prepared coatings in this study, dissimilar surface topographies were observed. This variation in surface topography caused different coating properties, which will be described and discussed in the following chapters. It is well seen in figures 4.15 and 4.16 that the alumina filler particles (which are a part of the as-supplied silicone rubber product used in this study)

contributed to the topographies of the prepared coatings. Such micro-sized particles are seen in both Figs. 4.15 and 4.16. However, on the rough substrate (Fig. 4.16), the prepared coating is rougher, while it is relatively flat on a flat substrate (see Fig. 4.15 and Fig. 4.2a for comparison). Though both TiO_2 and CeO_2 nanoparticles are relatively small, and therefore difficult to be seen in Figs. 4.14 and 4.13, they definitely contributed to both surface roughness and water-repellent properties of rough titania-doped RTV SR coatings. More specifically, while the non-doped rough sample in Fig. 4.16 demonstrated $\text{CAH} \sim 15^\circ$, its titania and ceria doped counterparts (in Figs. 4.14 and 4.13) exhibited improved CA values of $\sim 145^\circ$ and 145.5° and decreased CAH values of $\sim 10^\circ$ and 6° , respectively (see Figs. 4.9 and 4.11).

This effect can be easily explained by the nano-roughness added by nano-sized TiO_2 or CeO_2 particles, which could further improve the water repellency of the doped RTV SR coatings compared with that of the non-doped rough sample in Fig. 4.16.

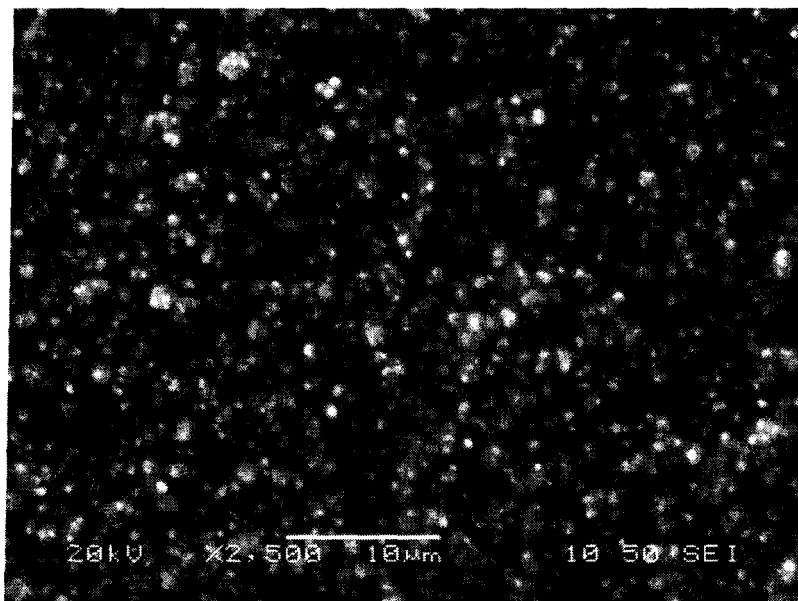


Fig. 4.15. SEM surface image of flat Al sample coated with RTV (1:4 v/v).

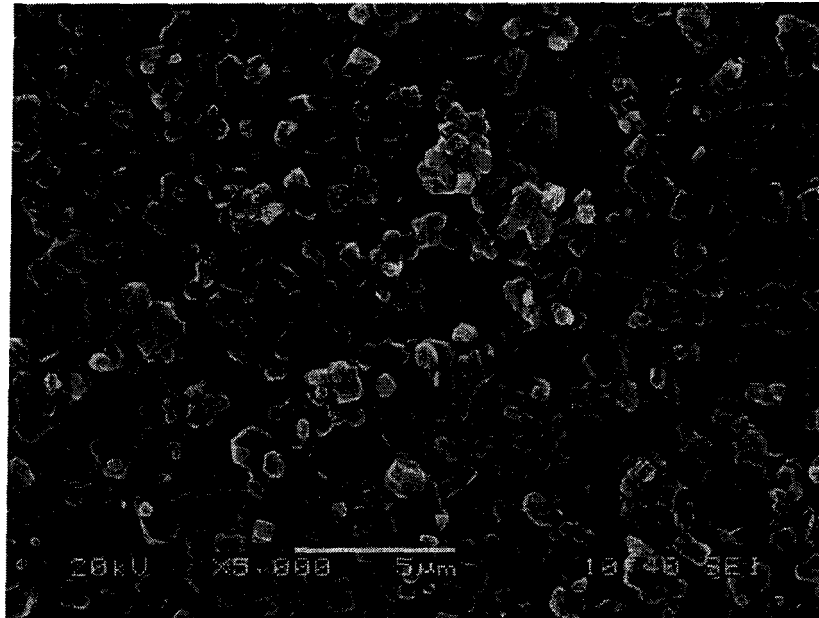


Fig. 4.16. SEM surface image of etched Al sample coated with RTV (1:4 v/v).

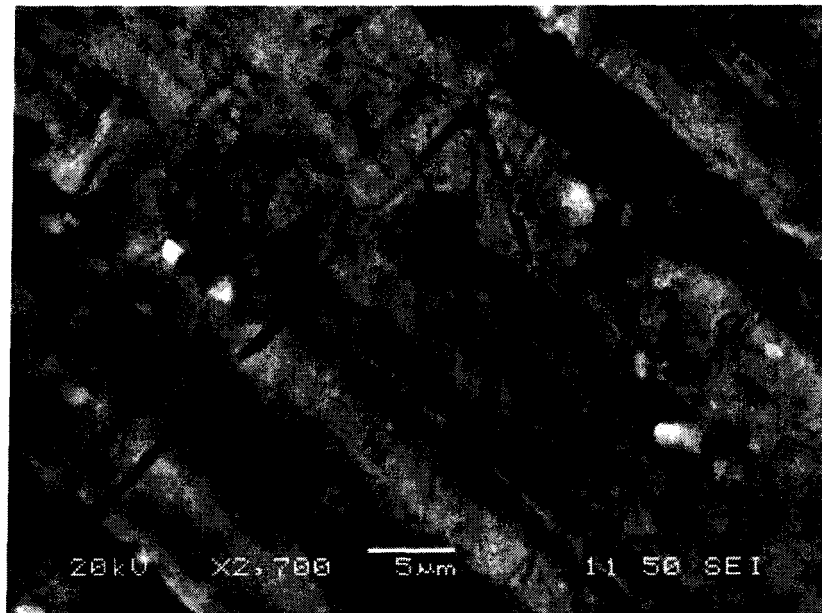


Fig. 4.17. SEM surface image of as-received aluminum sample.

4.4 Summary and Conclusions

The effect of incorporation of carbon-black nanoparticles as a dopant into the RTV silicone rubber coatings prepared from RTV silicone rubber/hexane solution 1:1 (v/v) on the flat substrates was studied. It was shown that the nanoparticles have no significant effect on the water contact angle on the coatings, although some slight increase was seen in the values of these parameters for the concentration from 6 to 18 vol. % of carbon-black. This small increase in water contact angle is believed to be related to the roughness of the coatings, which grew up slightly along with the carbon-black concentration (Fig. 4.2). Also the same results were seen on TiO₂ and CeO₂ nanoparticles as dopants into the RTV silicone rubber coatings on the flat aluminum substrate. Therefore, for preparation super-hydrophobic coatings, most efforts were mainly concentrated on rough etched Al substrates. On rough (etched) substrates, coatings with both high values of contact angle and low values of contact angle hysteresis were prepared in case of all nanopowders used. The SEM investigations of the sample surfaces revealed that the alumina filler (loaded into the as-supplied silicone rubber product) had some influence on the surface topographies of the prepared coatings. It was also found that the nanopowders used as dopants further increased the surface roughness (and correspondingly - water repellency) of the coatings.

CHAPTER 5

EXPERIMENTAL RESULTS AND DISCUSSION: ICE ADHESION STRENGTH ON SAMPLE SURFACE

CHAPTER 5

EXPERIMENTAL RESULTS AND DISCUSSION: ICE ADHESION STRENGTH ON SAMPLE SURFACE

The shear stress of ice detachment and the adhesion reduction factor (*ARF*) values of RTV SR coated samples doped with carbon-black (CB), TiO₂ or CeO₂ as a function of icing/de-icing cycles were tested. Ice adhesion on as-received and mirror polished aluminum was measured under the same conditions. Therefore, in this chapter, an attempt was in reducing the strength of adhesion of ice to the surfaces by applying ice-phobic coatings. The contact angle values as function of icing/de-icing number were measured after each icing/de-icing cycle on the coated samples.

5.1 Ice Adhesion Strength of Flat Aluminum Substrate Coated with RTV SR Incorporated with Carbon-Black (CB) Nanoparticles

The shear stress (of ice detachment) values for both mirror-polished aluminum surface and carbon-black doped RTV silicon rubber coatings are shown in Fig. 5.1. A similar value on a mirror-polished (bare) aluminum surface is given as a horizontal line

at ~350 kPa. A relatively small increase in ice adhesion strength is seen when the vol. % of carbon-black doped is raised from 0 to 18. Even the coating heavily loaded with carbon-black (18 vol. %) demonstrates a shear stress of ice detachment value equal to ~ 233 kPa (~33 % increase compared to the non-doped coating), which is ~1.5 times lower than on mirror-polished aluminum. The increase in ice adhesion strength with dopant concentration observed in Fig. 5.1 can be also explained by somewhat increased surface roughness of the doped coatings, which is in agreement with Fig. 4.1c in chapter 4.

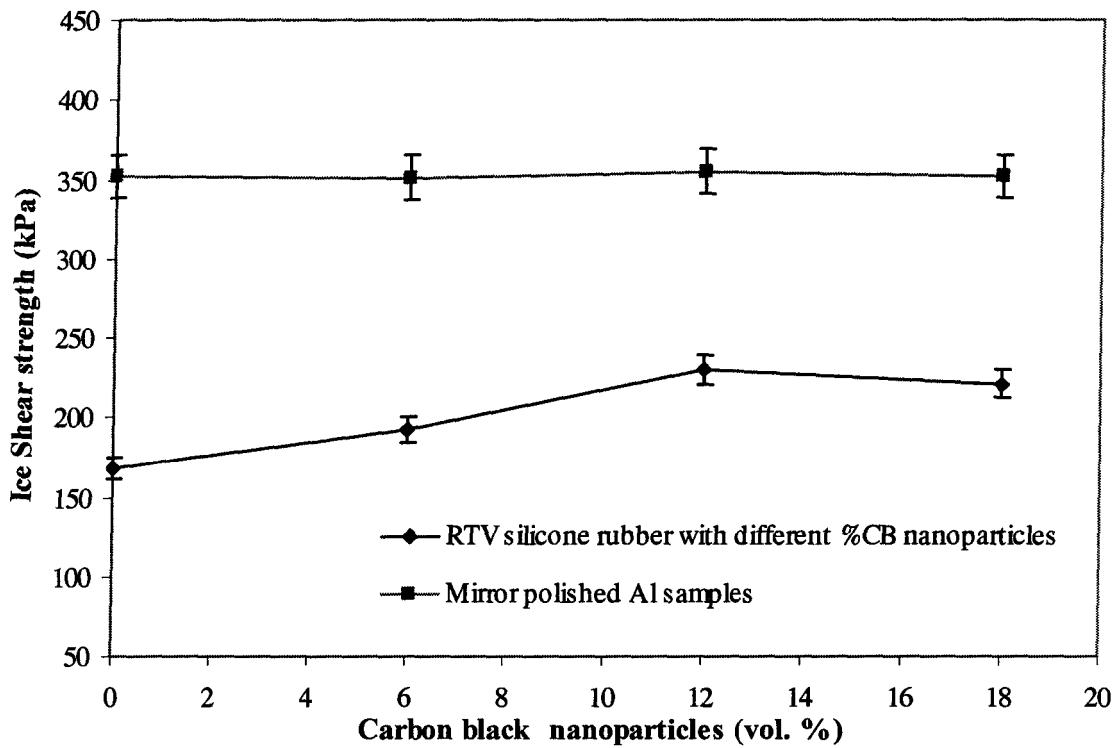


Fig. 5.1. Ice Shear stress (kPa) vs. vol % of carbon-black nanoparticles incorporated in RTV SR/hexane (1:1 v/v) coated samples.

5.2 Ice Adhesion Strength on Rough Al Substrate Coated with RTV SR Incorporated with TiO₂ or CeO₂ Nanoparticles

The shear stress of ice detachment values of RTV SR coated samples with different nanoparticles incorporated as a function of icing/de-icing cycles are shown in Figs. 5.2 and 5.3. Only super-hydrophobic samples (i.e. doped with TiO₂ or CeO₂) were tested. Ice adhesion on as-received and mirror-polished aluminum was measured under the same conditions, and the results are also presented in Figs. 5.2 and 5.3. For each coating studied, one sample was subjected to 10 successive icing/de-icing operations.

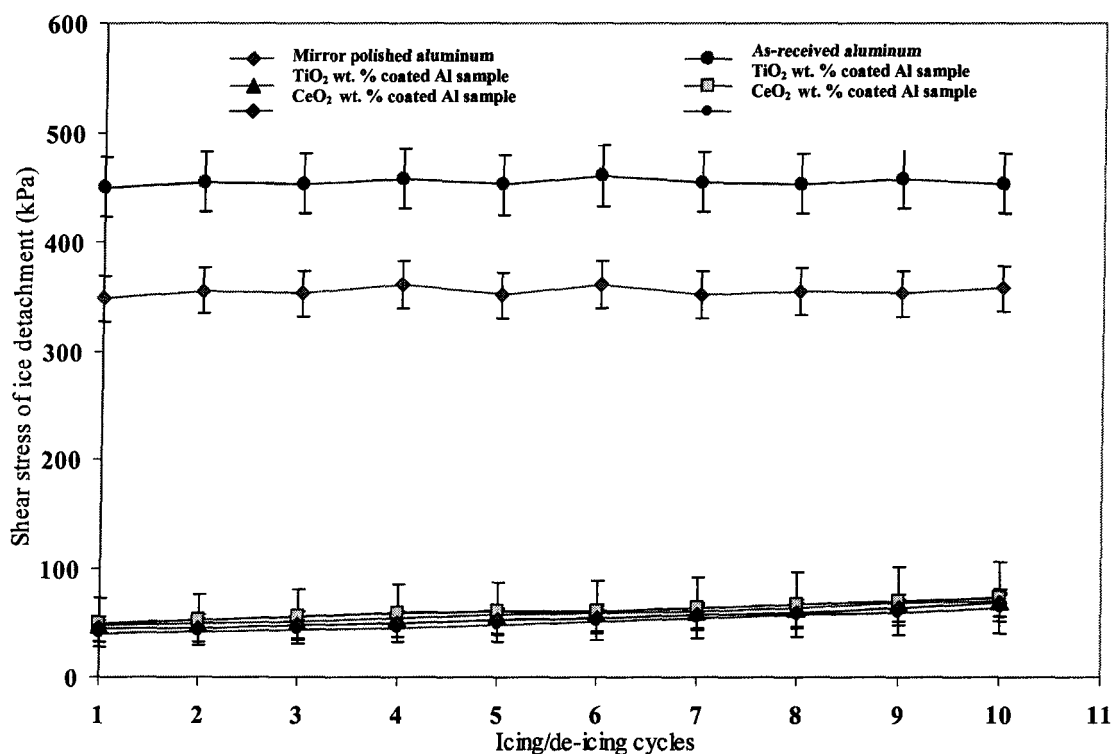


Fig. 5.2. Shear stress of ice detachment vs. icing/de-icing cycle number for coatings spin-coated from RTV SR/hexane solutions (1:4 v/v) with (1, 2 wt. %) TiO₂ and (1, 2 wt. %) CeO₂ nanoparticles incorporated, respectively.

As-received uncoated flat aluminum was used as a standard showing shear stress of ice detachment of 445 ± 20 kPa. The value of the mirror-polished aluminum surface (350 ± 19 kPa) is also shown in Fig. 5.2. Shear stress of ice detachment on different coated surfaces varied from 47 to 70, 50 to 72, 44 to 67 and 40 to 63 kPa for the coatings spin-coated from RTV SR (1:4 v/v) solution (in hexane) with 1, 2 wt. % of CeO_2 and 1, 2 wt. % of TiO_2 nanoparticles incorporated respectively. Reduced ice adhesion can be related to the low surface energy coatings on the samples and air incorporation into rough surface structures. It is observed that all samples values of ice adhesion strength were at least ~ 7 times lower than those obtained on the mirror-polished Al sample and ~ 9 times lower than those on the as-received aluminum sample. The hydrophobic properties of those surfaces were examined after ice removal.

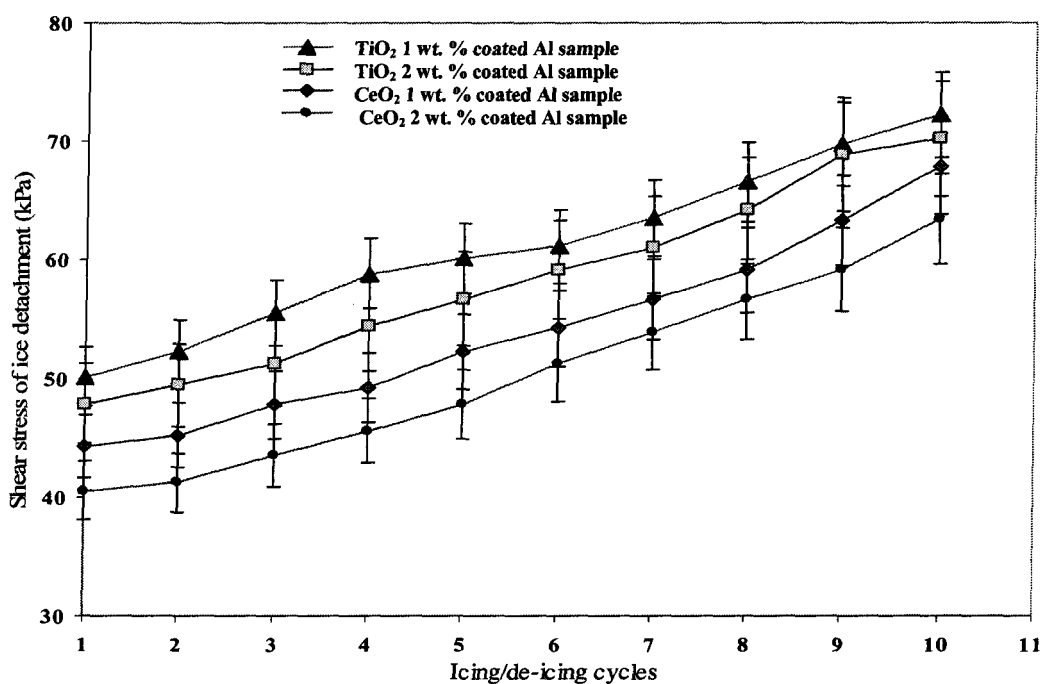


Fig. 5.3. Shear stress of ice detachment vs. icing/de-icing cycle number for coatings spin-coated from RTV SR/hexane solutions (1:4 v/v) with (1, 2 wt. %) TiO_2 and (1, 2 wt. %) CeO_2 nanoparticles incorporated, respectively.

It is also seen in Fig. 5.3 that the ice-releasing performance of the coated samples somewhat deteriorated after as many as 10 icing/de-icing cycles. This can be explained by some damage to the coatings caused by icing/de-icing. The nature of this damage is not fully known yet and needs more detailed investigations. It is believed that some asperities of the rough surfaces were partially damaged during icing/de-icing.

5.3 Adhesion Reduction Factor (*ARF*) Values of the Coated Samples

The adhesion reduction factor (*ARF*) values of the coated samples as a function of icing/de-icing cycles are presented in Figs. 5.4, 5.5, 5.6 and 5.7. The *ARF* values of the coatings spin-coated from RTV SR/hexane (1:4 v/v) solution with 1 wt. % of CeO₂ nanoparticles incorporated decreased from 7.89 to 5.27 as it is illustrated in Fig. 5.4. These results show that the initial ice adhesion was at least 7 times lower on this coating in comparison with bare aluminum (Fig. 5.4). However, a decrease in *ARF* values was observed after as many as 10 icing/de-icing events. This can be attributed to the gradual damage of the rough coatings during icing/de-icing. Additional investigations are needed to better understand the reasons for the deterioration of the rough samples and their anti-ice performance during icing/de-icing observed in Figs. 5.4-5.7.

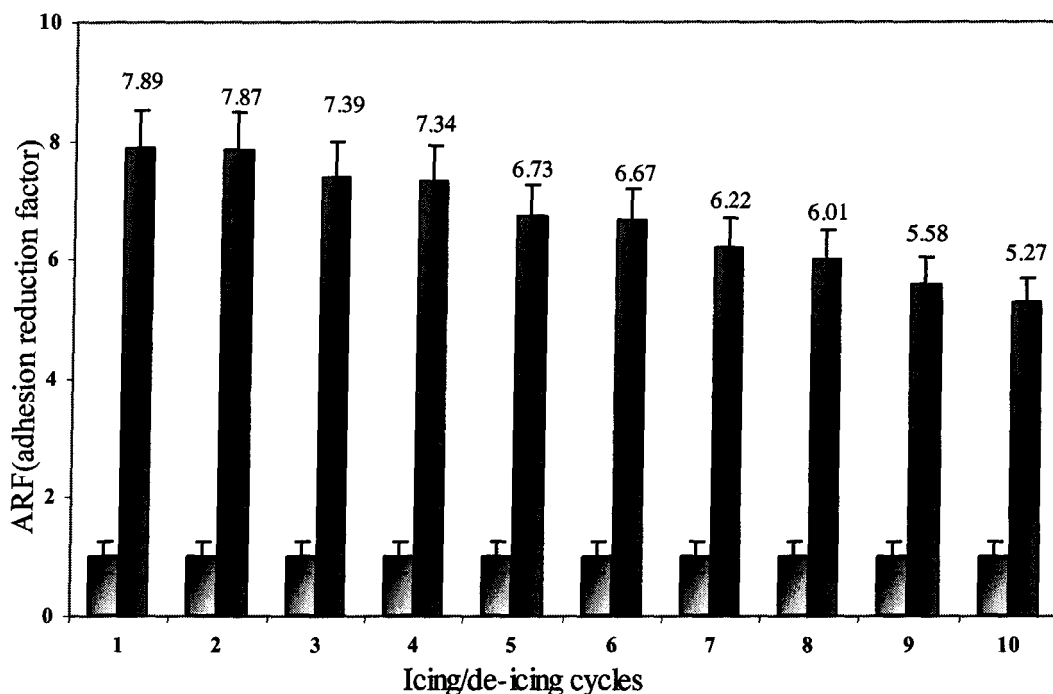


Fig. 5.4. Ice adhesion reduction factor (*ARF*) as a function of icing/de-icing cycles on mirror-polished Al and a coating prepared from RTV SR/hexane (1:4 v/v) solution with 1 wt. % of CeO₂ nanoparticle incorporated.

Similar behaviour in ice-repellent properties was also observed for the samples coated with RTV SR incorporated with different percentage of CeO₂ or TiO₂ nanoparticles (Figs.5.4, 5.5, 5.6 and 5.7 respectively). The *ARF* values of the samples with 1 and 2 wt. % of CeO₂ nanoparticles incorporated decreased from 7.89 to 5.27 and 8.61 to 5.64, respectively, by increasing the number of icing/de-icing cycles to 10 times (Figs. 5.4, 5.5). It is likely due to partial damage of the super-hydrophobic coatings during icing/de-icing cycles which caused the decrease of super-hydrophobic properties of the coated aluminum surfaces.

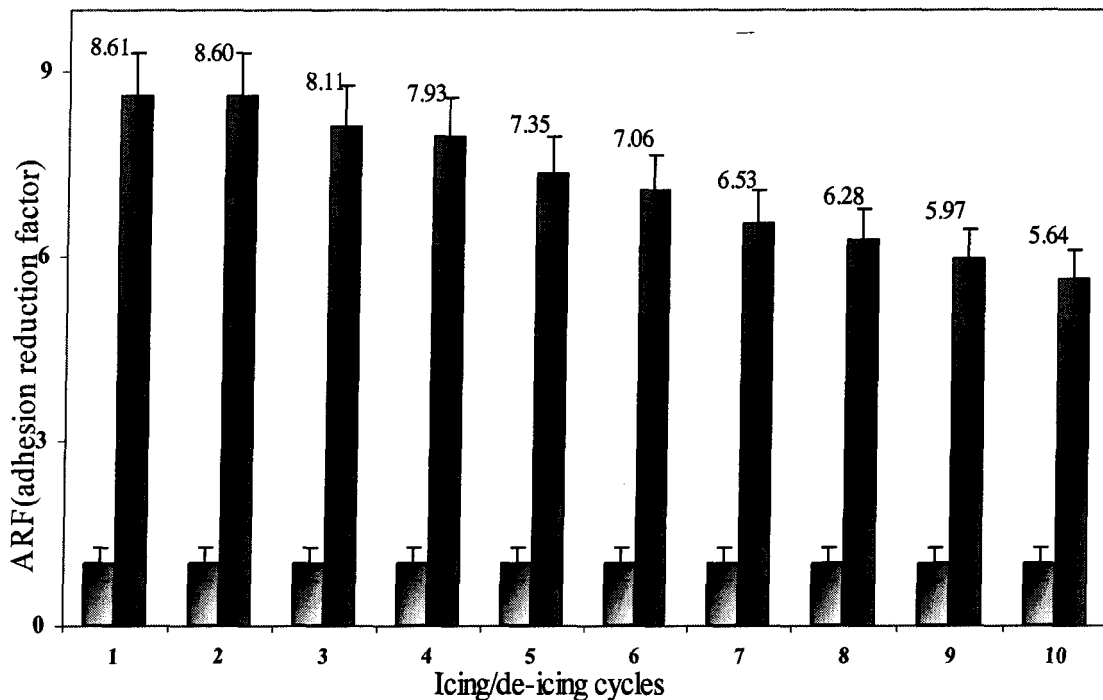


Fig. 5.5. Ice adhesion reduction factor (ARF) as a function of icing/de-icing cycles on mirror-polished Al and a coating prepared from RTV SR/hexane solution (1:4 v/v) with 2 wt. % of CeO_2 nanoparticle incorporated.

As it can be seen in Figs. 5.6, 5.7, the ARF values of the RTV SR coated aluminum samples with 1 and 2 wt. % of TiO_2 nanoparticles incorporated decreased from 6.96 to 4.95 and 7.29 to 5.09, respectively, by increasing the number of icing/de-icing cycles to 10 times. This observed decrease of ARF values is probably due to partial/fractional damage of the super-hydrophobic coatings during icing/de-icing events which result in decreasing of super-hydrophobic properties of the coated aluminum substrates.

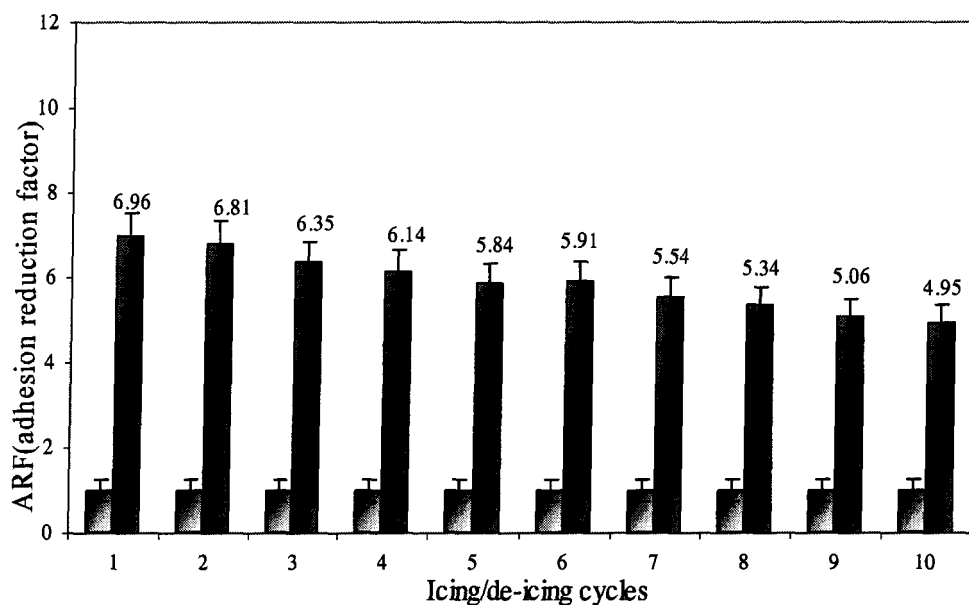


Fig. 5.6. Ice adhesion reduction factor (*ARF*) as a function of icing/de-icing cycles on mirror-polished Al and RTV SR/hexane solutions (1:4 v/v) coating with 1 wt. % of TiO₂ nanoparticles incorporated.

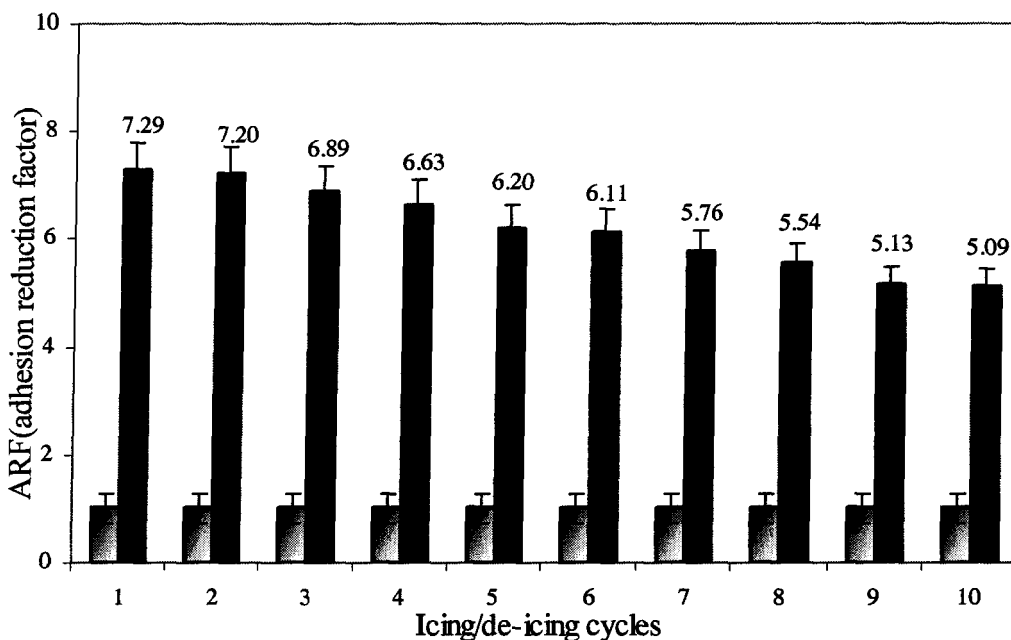


Fig. 5.7. Ice adhesion reduction factor (*ARF*) as a function of icing/de-icing cycles on mirror-polished Al and RTV SR/hexane solutions (1:4 v/v) coating with 2 wt. % of TiO₂ nanoparticles incorporated.

5.4 Contact Angle as a Function of Icing/de-Icing Cycles

It is important to know how such anti-ice coatings perform in time and how their hydrophobic properties change. This was investigated by performing contact angle measurements on the samples after icing/de-icing events. Figs. 5.8 and 5.9 illustrate contact angle values as function of icing/de-icing events obtained after each icing/de-icing cycle on the coated samples. All coated samples showed a gradual decrease in CA values after each icing/de-icing event. This confirms that the rough surfaces were gradually damaged and removed during each icing/de-icing event. This led to gradually decreased surface roughness, which can explain why the CA values in Figs. 5.8 and 5.9 decreased from $\sim 145^\circ$ to $\sim 125^\circ$ after the samples were iced/de-iced 10 times.

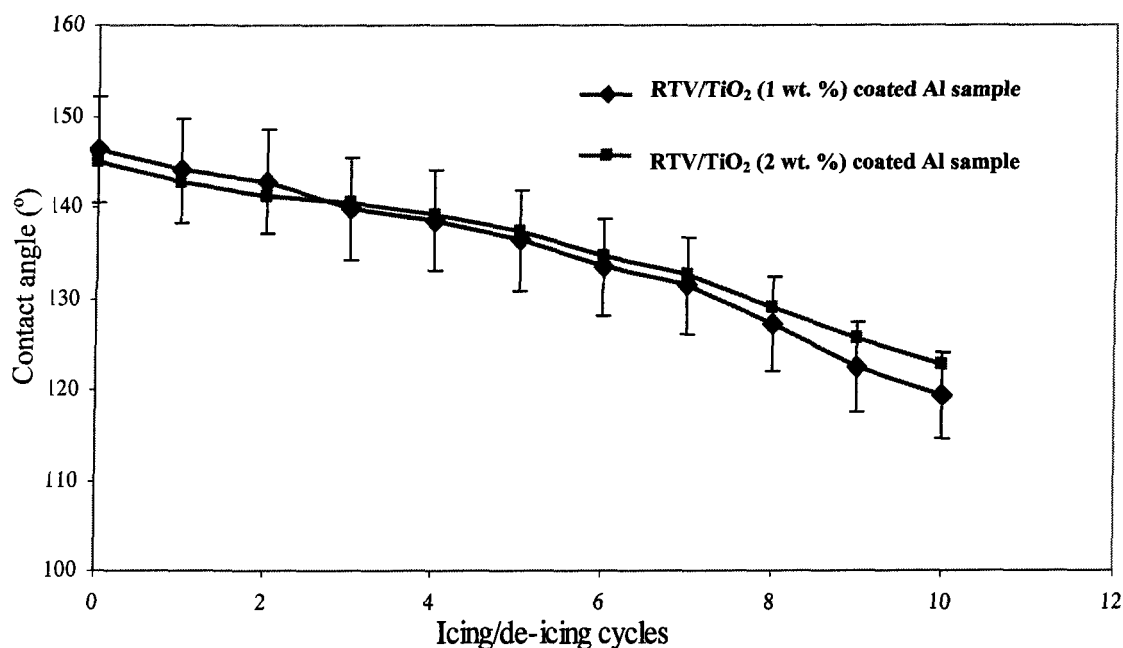


Fig. 5.8. Contact angle vs. icing/de-icing cycles number for the RTV SR coatings prepared from RTV SR/hexane mixtures (1:4 v/v) and doped with TiO₂ (1 and 2 wt. %) coated aluminum samples.

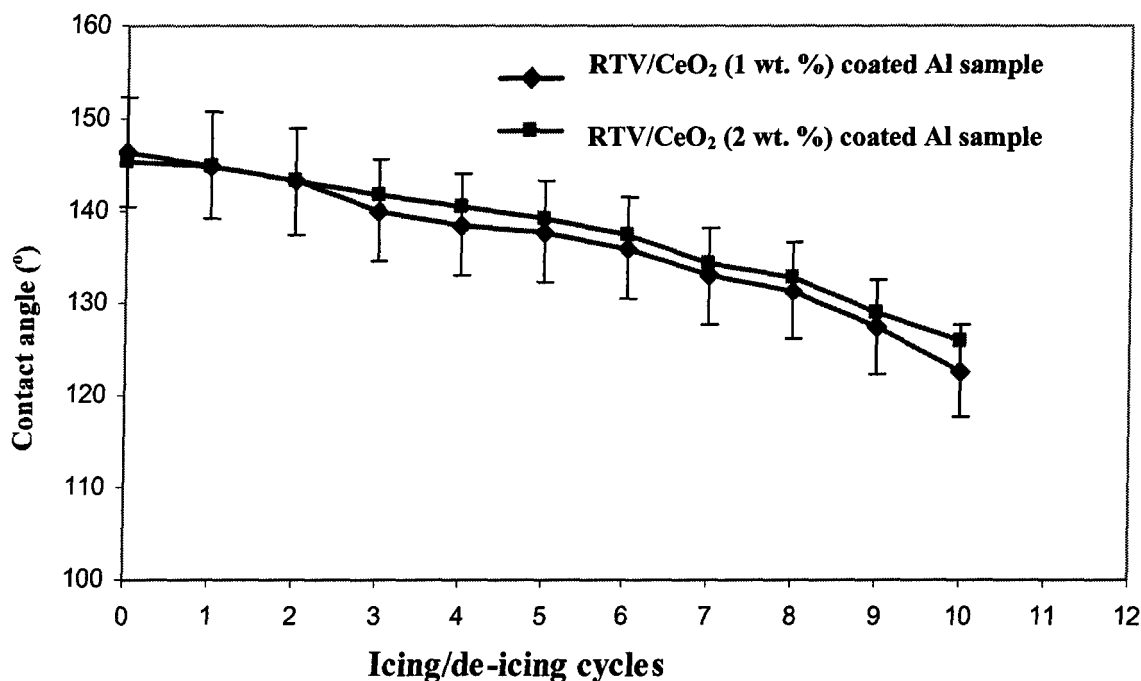


Fig. 5.9. Contact angle *vs.* icing/de-icing cycles number for the RTV SR coatings prepared from RTV SR/hexane mixtures (1:4 v/v) and doped with CeO₂ (1 and 2 wt. %) coated aluminum samples.

This decrease in CA could be associated with loss of hydrophobic properties of the RTV SR/TiO₂ (1 and 2 wt. %) coated aluminum samples after 10 icing/de-icing cycles. The shear stress of ice detachment values on such coated samples were shown to gradually increase as the samples were iced/de-iced repeatedly (see section 5.2). Therefore, both the increasing ice adhesion strength and decreasing contact angle values confirm the assumption that the super-hydrophobic coatings in study gradually deteriorated during icing/de-icing as a result of gradually decreasing surface roughness.

5.5 Summary and Conclusions

These results show that initially, ice adhesion was at least 7, 8 and 6, 7, (1, 2 wt. % of CeO₂) and (1, 2 wt. % of TiO₂) times lower on the coatings in comparison to mirror-polished aluminum, which can lead to easier removal of accumulated ice from those surfaces. The highest *ARF* value of 8.61 was obtained in case of 2 wt. % of CeO₂ nanoparticle treated surface in comparison to 7.89 found for the sample with 1 wt. % of CeO₂ incorporated. However, *ARF* values were somewhat lower on the TiO₂-doped RTV SR coatings, being initially 7.89 and 6.96 for the samples with 2 wt. % and 1 wt. % TiO₂, respectively. This finding can be explained by somewhat lower hydrophobic properties observed for the TiO₂-doped RTV SR coatings. As lower water-solid contact area are expected on super-hydrophobic surfaces with higher CA and lower CAH values (i.e. with CeO₂ dopant), this must have led to smaller ice-solid contact areas on such surfaces, and that is why the ice adhesion strength on such samples was found to be smaller. The reason of these differences in previous mentioned obtained results could be the different surface topography of the samples prepared with different nanopowders and their concentration in RTV SR/hexane solution.

The results obtained in this work on RTV SR coatings incorporated with different types of nanoparticles (i.e. carbon black, TiO₂, CeO₂) suggest that no obvious effect of dopant nature (and thus dielectric properties) on ice adhesion strength was observed. The difference in ice adhesion strength evaluated on different (flat and rough) samples suggests that it is the surface topography (and thus, the ice-solid contact area as a result of the latter) that plays the crucial role in governing the ice adhesion strength on

nanoparticle-incorporated RTV SR coatings (rather than the particle nature). This could be explained by **(i)** relatively low concentrations of the particles used ($\sim 1 - 3$ wt. %), **(ii)** good coverage of the particles by RTV SR material (which interacted with water and/or ice) and **(iii)** very small contact areas (ice-solid) on the super-hydrophobic samples studied. Therefore, the previously proposed hypothesis on the effect of the dielectric constant of the material coating [85] on the strength of ice adhesion on its surface was not confirmed in this work and may need further experimental tests to be verified.

CHAPTER 6

EXPERIMENTAL RESULTS AND DISCUSSION:

**STABILITY OF SAMPLES IMMERSED IN DI-
WATER AND FREEZING OF WATER DROPLETS
ON SAMPLE SURFACES**

CHAPTER 6

EXPERIMENTAL RESULTS AND DISCUSSION: STABILITY OF SAMPLES IMMERSSED IN DI-WATER AND FREEZING OF WATER DROPLETS ON SAMPLE SURFACES

In this chapter, freezing of water droplet on the surfaces prepared was investigated. The small water droplets freeze on different surfaces over time at surface temperature $\sim -15^{\circ}\text{C}$. The results obtained of freezing time (s) as a function of contact angle hysteresis (CAH) are presented below. Also the stability of three super-hydrophobic RTV SR coatings (doped with carbon-black, TiO_2 or CeO_2) by immersion in de-ionized water were studied.

6.1 Stability of Samples Immersed in DI Water

Figs. 6.1-6.3 show how contact angle evolves on surface of three super-hydrophobic RTV SR coatings (doped with carbon-black, TiO_2 or CeO_2) as a function of immersion time in de-ionized water. From time to time, the samples were removed from water, blown with nitrogen, and their CA values were evaluated. These series of

experiments were carried out by dipping samples under de-ionized water with water conductivity of $\sim 0.32 \mu\text{s. Cm}^{-1}$. All the coatings studied are demonstrated to gradually lose their hydrophobic properties over time. For instance, this is observed for Al samples coated with RTV/TiO₂ (2 wt. %) and RTV/CB (3 wt. %) by ~ 700 h of immersion in de-ionized water and ~ 1200 h of immersion in de-ionized water for coated Al samples with RTV/CeO₂ (2 wt. %), which is associated with significant decrease of water contact angles. Moreover, all coated samples immersed/tested in de-ionized water were from time to time removed from water and annealed over-night to get rid of any water (if any) that might penetrate into the rough structure between asperities.

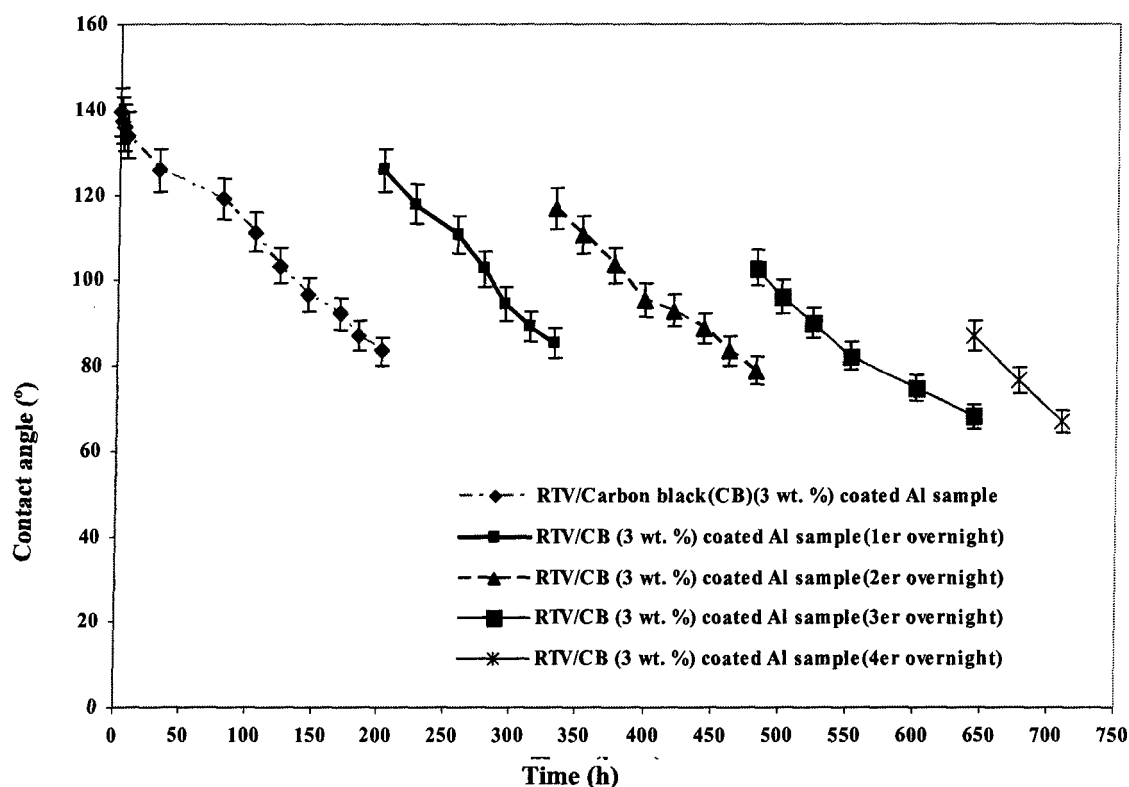


Fig. 6.1. Contact angle vs. immersion time in de-ionized water for RTV SR/CB (3 wt. % of carbon-black) coating.

The results (Figs. 6.1 - 6.3) show that after each annealing event, the samples' contact angle values could be regained only partially, which means that the coatings degraded during continuous contact with DI water. Any possible effect of different nanoparticle size and/or nature on coating stability was also investigated showing all coatings degrade slowly within several days of immersion in de-ionized water, which is seen as a decrease of CA values over time. The nature of this deterioration (or chemistry of coating-water reactions, if any) is not clear yet.

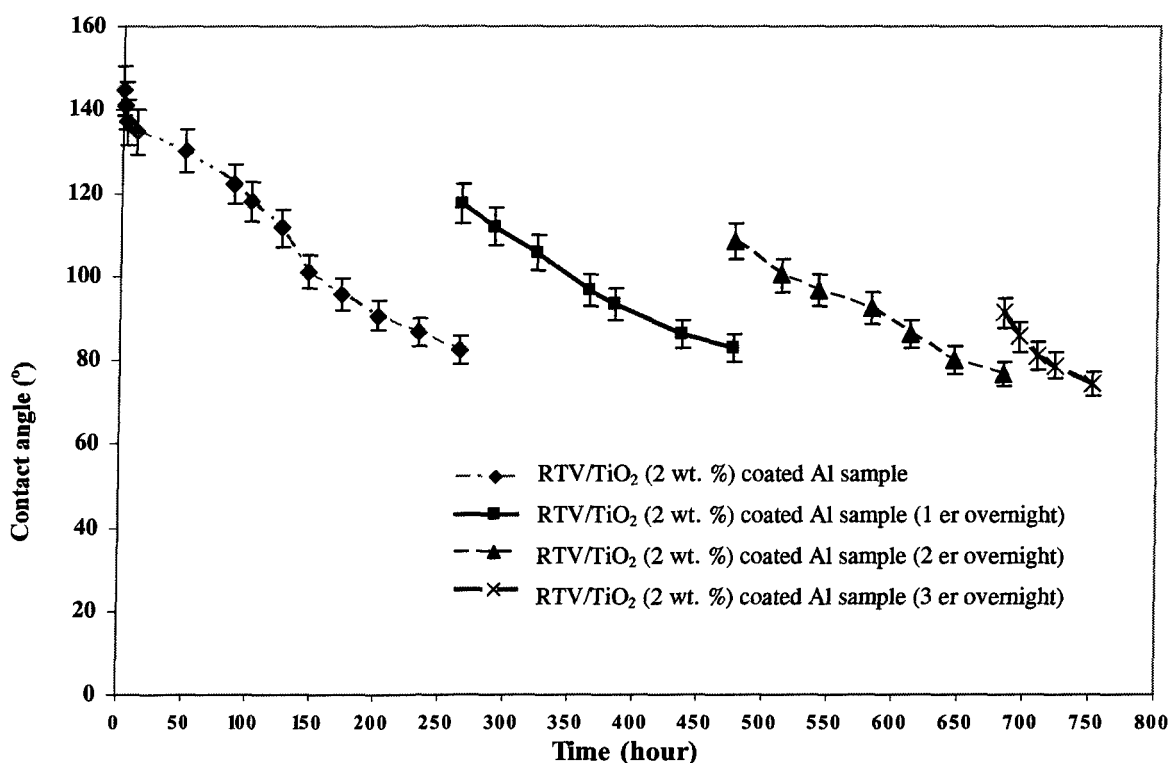


Fig. 6.2. Contact angle vs. immersion time in de-ionized water for Al sample coated with RTV (1:4) / TiO₂ (2 wt. %).

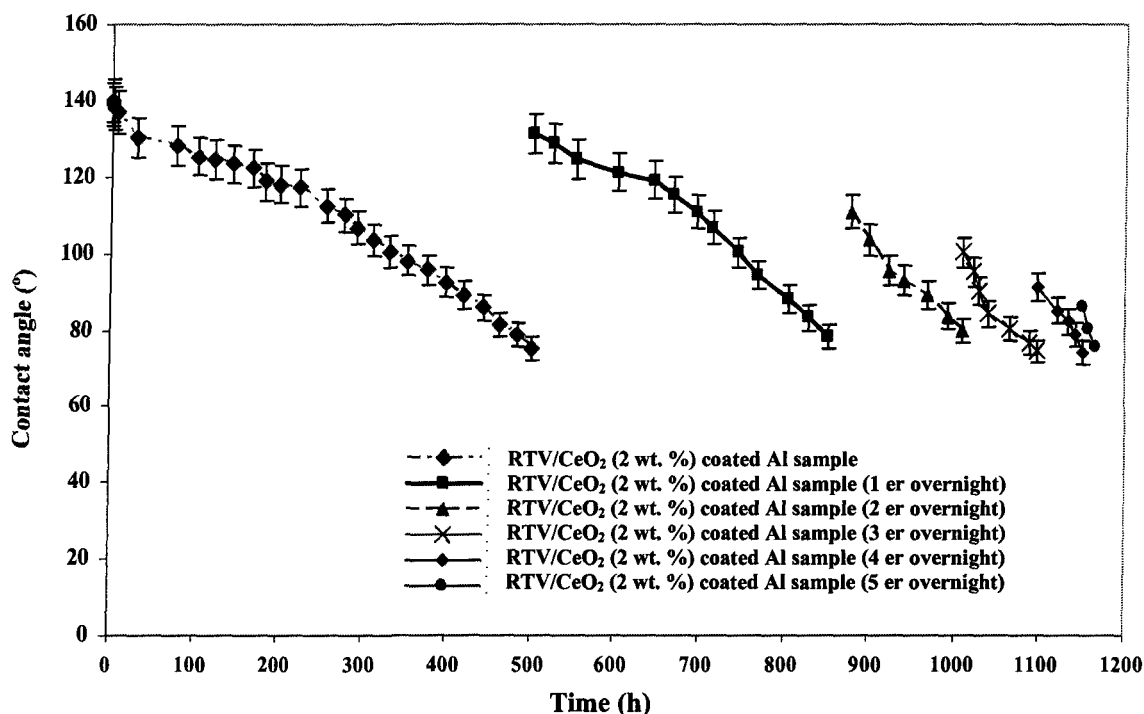


Fig. 6.3. Contact angle vs. immersion time in de-ionized water for Al sample coated with RTV (1:4) / CeO₂ (2 wt. %).

6.2 Freezing of Water Droplets on Sample Surfaces

A series of experiments were conducted to investigate water freezing on the surfaces prepared. Figure 6.4 demonstrates how small water droplets freeze on two different surfaces (uncoated Al, Fig. 6.4a, and CeO₂-doped super-hydrophobic RTV SR coatings, Fig. 6.4b) over time at surface temperature $\sim -15^{\circ}\text{C}$. The results obtained of freezing time as a function of contact angle hysteresis (CAH) are presented in Fig. 6.5. During the experiments, water droplets (4 μL) were placed on a Peltier cooling stage unit (at -15°C), and their images were regularly taken by using the goniometer's optics and software. It was observed that the maximum freezing time for water droplet on the

samples' surface refers to the surfaces covered with RTV SR/CeO₂ and RTV SR/TiO₂. All concluded freezing steps (from 22 °C to -15 °C) can be seen in Figs. 6.4a and 6.5b from left to right, respectively. Fig. 6.4 shows representative images for droplets freezing on flat (uncoated) Al (a) and on CeO₂- incorporated RTV SR super-hydrophobic coating (b). The images show droplet shapes and times (i) immediately after the droplets were placed on the cold surfaces, (ii) immediately after water-solid interface ice nucleation, (iii) after complete drop crystallization. The ice nucleation at the solid-water interface was observed and determined as the time when light reflection (inside the droplet) drastically changed (see Fig. 6.4). This occurred, e.g., after ~3s on the flat uncoated Al and after ~720 s on the CeO₂/RTV SR super-hydrophobic samples (see Figs. 6.4a, 6.4b)

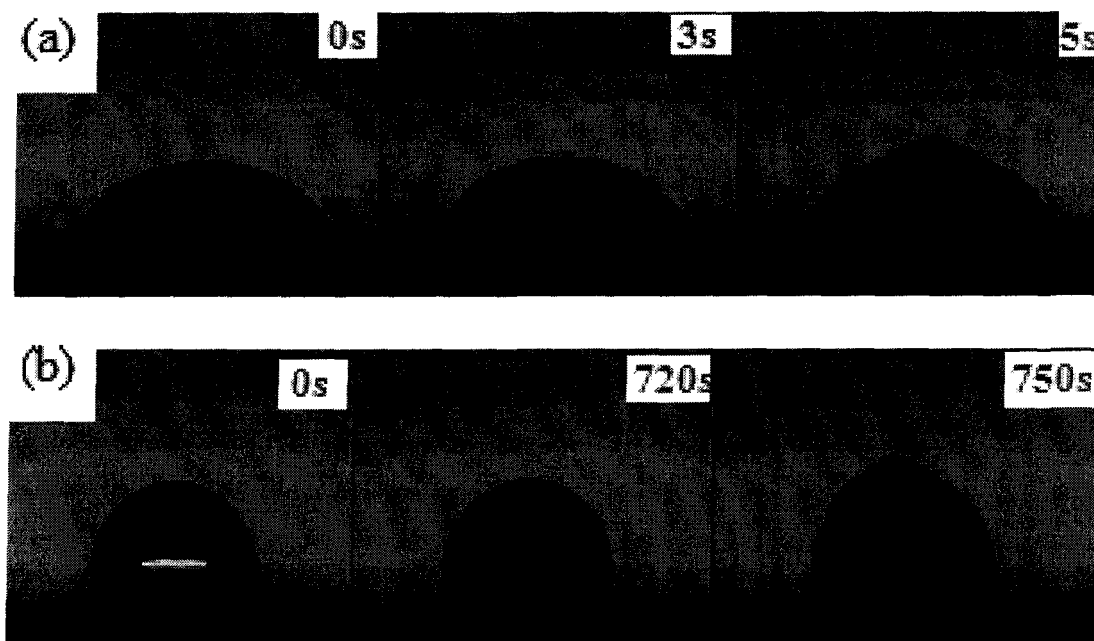


Fig. 6.4. Images of small water droplets on cold (-15 °C) surfaces: (a) flat Al, (b) rough super-hydrophobic RTV/CeO₂ surface.

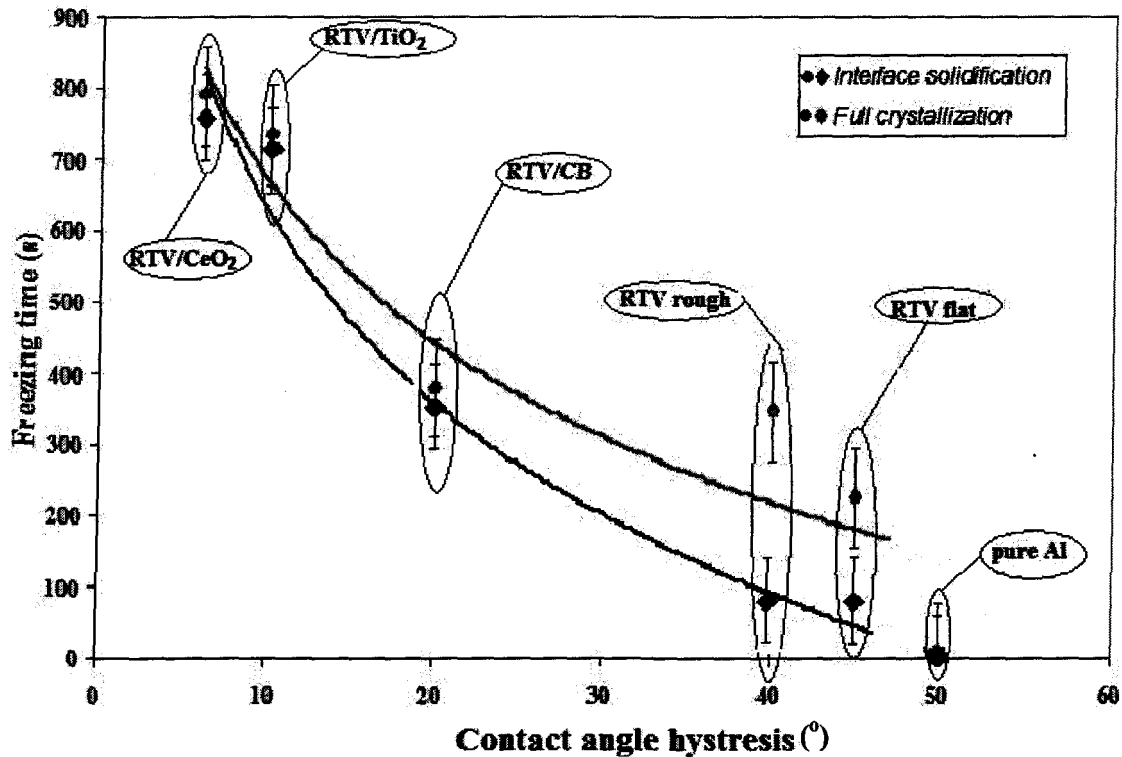


Fig. 6.5. Water droplet freezing times vs. contact angle hysteresis of coated samples. Data for uncoated flat Al are also given. The lines are simply guide to the eye.

Figure 6.5 demonstrates the water droplet freezing time for the flat uncoated Al surface was very short, and water froze just within a few seconds (Fig. 6.4a). However, the water droplet freezing time for rough Al surfaces coated with RTV SR/CeO₂ nanoparticles or TiO₂ nanoparticles incorporated was significantly longer (on the order of ~12 - 13 min). The reason for such different behaviour was the different surface topography of the samples. The water-solid contact area on the super-hydrophobic samples was very small (see Fig. 6.6). When the water-solid contact area increases, heat transfer between the surface and water droplet will be increased as well. This well explains the trend clearly observed in Fig. 6.5. The CAH values on rough hydrophobic

surfaces with same chemistry (RTV SR) are directly related to water-solid contact areas on the samples.

Table 6.1 gives a brief description of the samples. The samples prepared in this study were: polished aluminum (sample 1), RTV SR coated polished aluminum (sample 2), HCl etched (rough) RTV SR coated aluminum (sample 3) and rough RTV SR coated samples doped with carbon-black, CeO₂ and TiO₂ nanopowders (samples 4, 5 and 6, respectively). In all the cases, the RTV SR to hexane ratio was 1:4.

Table 6.1. Contact angle, contact angle hysteresis and freezing times of different samples.

Sample	1	2	3	4	5	6
Topography	<i>Polished Al</i>	<i>RTV SR flat</i>	<i>RTV SR rough</i>	<i>RTV SR rough</i>	<i>RTV SR rough</i>	<i>RTV SR rough</i>
Dopant	-	-	-	CB	CeO ₂	TiO ₂
CA (deg.)	55 ± 5	110 ± 2	143 ± 1.5	145 ± 1	147 ± 1	146 ± 1
CAH (deg.)	≥ 50	45	40	20	5	9
Freezing Times (s)	3/5	85/218	37/347	353/380	755/780	705/735

Figure 6.6 illustrates how heat is transferred through the water-solid interface area of a water droplet residing on a super-hydrophobic surface (Cassie-Baxter regime). It is evident from this schematic model that the more surface roughness is, the less water-solid contact area, and thus, the more entrapped air between water-solid. Therefore, the heat exchange process between water droplet and solid will be reduced due to the entrapped air (as insulator) leading to postponed freezing time of water

droplets. Therefore, as seen in Fig. 6.5, water drops were frozen with such a big delay on super-hydrophobic samples (~12-13 min) compared to their flat or uncoated counterparts. Note that the rough hydrophobic surface coated with RTV SR did not delay water freezing on its surface much. This could be related to a larger water-solid contact area on this surface. This agrees well with the relatively large value of CAH observed on this surface (~40°).

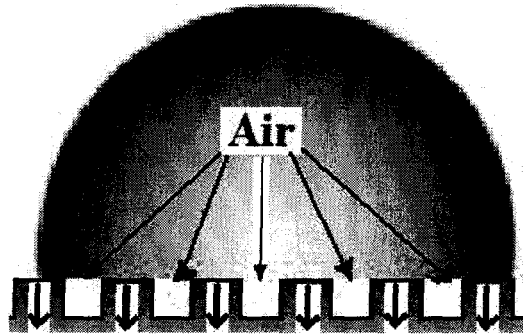


Fig. 6.6 Water drop on a super-hydrophobic surface. Heat transfer at surface/ water drop interface is shown by short arrows.

Table 6.2 presents thermal conductivities for all materials involved into the samples in Fig. 6.5. Uncoated Al is seen to have the highest thermal conductivity, and this is in agreement with the fast freezing observed in Fig. 6.4a.

Table 6.2. Thermal conductivity values of different material.

Material	Air	Ice	Aluminum	RTV SR	Carbon black	TiO ₂	CeO ₂
Thermal conductivity (WmK ⁻¹)	0.024 [86]	2.18 [86]	167 [87]	1.1 [88]	0.2-0.3 [89]	8.5 [90]	12 [91]

Carbon-black demonstrates a relatively low thermal conductivity, and this could contribute to the delay in freezing observed on the super-hydrophobic carbon-black -incorporated RTV SR coating in Fig.6.5. . Both CeO_2 and TiO_2 have quite low thermal conductivities (almost as low as that of RTV SR). This could also contribute to the longest freezing delay on the coatings doped with TiO_2 and CeO_2 . However, the major factor is believed to be the low water-solid contact area on these surfaces.

6.3 Summary and Conclusions

It was shown that all coatings slowly degrade after several days of immersion in de-ionized water, which is seen as a reduction of CA values over time. For example, via ~700 h of immersion in de-ionized water in case of coated Al samples with RTV SR/ TiO_2 (2 wt. %) and RTV SR/CB (3 wt. %) coatings and ~1200 h of immersion in de-ionized water for coated Al samples with RTV SR/ CeO_2 (2 wt. %). But the nature of this deterioration is not clear yet.

The combination of both the low CAH value and delayed freezing observed on the super-hydrophobic coatings prepared show promise for anti-ice applications. First, as shown above, water droplets freeze with a significant delay on such surfaces. Second, low CAH values provide high mobility of the droplets on such surfaces. Therefore, water droplets can roll off such surfaces before getting frozen. This is believed to lead to significantly reduced ice accumulation on such surfaces. Finally, significantly lower values of ice adhesion strength were also found for such surfaces

(compared to uncoated Al), thus clearly making them attractive candidates for anti-ice applications on various high-voltage equipment (both conductors and insulators).

CHAPTER 7

CONCLUSIONS AND RECOMMENDATION FOR FUTURE WORKS

CHAPTER 7

CONCLUSIONS AND RECOMMENDATION FOR FUTURE WORKS

7.1 Conclusions

In this study, hydrophobic and ice-repellent behaviour of silicone rubber coatings doped with nanopowders was studied and compared with that of uncoated metal surface. For this purpose, various flat and rough coatings were prepared, using a number of nanopowders as dopants. Carbon-black, TiO₂ and CeO₂ nanopowders were used, being materials which are (or can be) used to modify both mechanical and electrical properties of silicone rubber layers for application to outdoor power network equipment, including insulators. It was shown that the hydrophobic and ice-releasing properties of flat composite (i.e. doped) coatings are not influenced by nanopowder incorporation significantly, implying that all nanopowders were well dispersed in silicone rubber material, and the latter constituted the topmost layer of the coatings. By optimizing spin-coating parameters, coatings with super-hydrophobic properties could be prepared. Such coatings demonstrated high values of contact angle with water and

low values of contact angle hysteresis for all the nanopowders used. The achieved super-hydrophobicity is shown to be a result of the combination of a low-surface-energy layer and both micro- and nano-roughnesses which are provided by the alumina filler (present in the silicone rubber product) and dopant particles, respectively.

Use of rough (etched) substrates facilitated the preparation of super-hydrophobic surfaces. More diluted nanopowder-silicone rubber (with hexane) suspensions were found to lead to coatings with improved water repellency when composite coatings with various dopants were prepared on rough substrates. Moreover, when the substrate etching time was increased from 1 min to 5 min, contact angle of the coated doped samples normally increased and contact angle hysteresis decreased. This tendency in hydrophobic properties was observed by applying different concentrations of carbon black nanoparticles (1.5 and 3 wt. %), TiO_2 (1 and 2 wt. %) or CeO_2 (1 and 2 wt. %) incorporated. These observations are believed to be related to the coatings roughness, which grew up slightly along with increasing weight percentage of carbon-black (1.5 to 3 wt. %), TiO_2 , or CeO_2 (1 to 2 wt. %) concentration incorporated into the coatings.

The ice-releasing properties of super-hydrophobic coatings were shown to be enhanced, if compared to those of flat coatings with same composition, which is explained by the reduced ice-solid contact areas on such micro-/nano-rough surfaces. However, the icephobic performance of such super-hydrophobic surfaces somewhat degraded during successive icing/de-icing cycles, implying the occurrence of some mechanical damage to the rough surfaces. The ice-releasing performance of the coated samples showed some deterioration after 10 icing/de-icing cycles. All super-hydrophobic samples demonstrated initial ice adhesion strength values at least ~ 7 times lower than

those obtained on a mirror-polished aluminum and ~ 9 times lower than those on an as-received uncoated Al sample. This decrease in ice adhesion strength can lead to easier removal of accumulated ice from such coated surfaces.

All the coatings studied were demonstrated to gradually lose their hydrophobic properties after ~ 700 h of immersion in de-ionized water for the samples coated with TiO_2 or carbon-black incorporated silicone rubber and ~ 1200 h for samples coated with CeO_2 doped silicone rubber, which was seen as a significant decrease of their water contact angle.

The freezing of water droplets on various samples was investigated by placing droplets on surfaces at -15 °C. While on flat uncoated Al small droplets froze after ~ 3 -5 seconds, their freezing was significantly delayed on rough CeO_2 and TiO_2 incorporated silicone rubber coatings, taking place at ~ 12 -13 min. The delayed freezing of water droplets on the nanocomposite super-hydrophobic surfaces examined is explained by the reduced water-solid contact areas on such rough surfaces. As the water-surface interface on such samples is to a large extent air, this slows down any heat exchange between water droplets and cold surfaces, leading to significantly delayed water freezing. Taking into account the high water mobility observed on such surfaces (i.e. low wetting hysteresis), this shows promise, as water can be removed from such super-hydrophobic surfaces before getting frozen. Thus, the silicone rubber coatings (doped with nanopowders) prepared in this study show promise as anti-ice materials that can reduce accumulation of ice on outdoor power network equipment. Provided that such rough doped coatings with similar topographies are prepared on other substrates (e.g., porcelain or glass), similar behaviour is expected in all cases. That is, even though this study was

focused on aluminum (metal) as substrate, its results can equally be applied to any other materials which are subjected to outdoor icing.

7.2 Recommendations for Future Work

(i) Various nanoparticle-incorporated silicone rubber coatings are to be carefully studied on different substrates (non-metallic substrates, with properties close to those of insulators). And both optimal parameters for enhanced super-hydrophobicity and adhesion of the coatings to the substrates are to be sought.

(ii) Different types of as-supplied RTV silicones, ranging from heavily loaded with fillers to filler-free silicones are recommended to be tested. Doping such different silicone rubbers with different nanopowders will give more information on how different fillers, modifying both mechanical and electrical properties of silicone rubber coatings, influence their wetting and ice-repellent properties.

(iii) The electrical properties (e.g. dielectric constant) of such composite coatings are to be studied as a function of nanopowder/dopant concentration and nature, as well as coatings, thickness and topography (in case of rough coatings).

(iv) Preparation of rough coatings can be further optimized on different (including flat) substrates, so that super-hydrophobic coatings can be reached on both rough and flat substrates.

(v) Flashover voltage is to be measured on surfaces of such nanopowder-modified silicone rubber coatings on insulators, which is expected to be higher than on nanoparticle-free silicone rubber coatings.

(vi) Further studies should be conducted in order to improve anti-ice performance of such coatings during icing/de-icing. In this context, coatings ranging from heavily-doped with various nanopowders as fillers (i.e., harder coatings) to those based on filler-free silicone rubber (i.e., most elastic coatings) are recommended to be tested.

References

- [1] M. Farzaneh, Ed., "Atmospheric icing of power networks", Springer, Berlin, (2008) 381 p.
- [2] M. Farzaneh and W.A. Chisholm, "Insulators for icing and polluted environments", IEEE Press series on Power Engineering, IEEE/John Wiley, New York, (2009) 680 p.
- [3] M. Farzaneh and O. T. Melo, "Flashover performance of insulators in the presence of short icicles", *Int. J. Offshore Polar Eng.* **4** (1994) 112.
- [4] M. Farzaneh (Chair), "IEEE standard 1783 – guide for test methods and procedures to evaluate the electrical performance of insulators in freezing conditions". IEEE Press, New York, October 2009.
- [5] M. Farzaneh, "Ice accretion on H.V. conductors and insulators and related phenomena", *Philos. Trans. R. Soc. London, Ser. A.* **358** (2000) 1.
- [6] M. Farzaneh, "Rapport sur la tempête de verglas de Janvier 1998, comité d'experts d'Hydro- Quebec (Comité Varennes)" 1998.
- [7] V. F. Petrenko and S. Peng, "Reduction of ice adhesion to metal by using self-assembling monolayers (SAMs)", *Can. J. Phys.* **81** (2003) 387.
- [8] J. L. Laforte, M. A. Allaire and J. Laflamme, "State-of-the-art on power line de-icing", *Atm. Res.* **46** (1998) 143.
- [9] C. Laforte and A. Beisswenger, "Icephobic material centrifuge adhesion test", in international workshop on atmospheric icing on structures (IWAIS), Montreal, Canada, 2005.
- [10] V. K. Croutch and R. A. Hartley, "Adhesion of ice to coatings and the performance of ice release coatings", *J. Coat. Technol.* **64** (1992)41.
- [11] B. Y. Yang and R. Montgomery, "De-icers derived from corn steep water", *Bio. Technol.* **90** (2003) 265.
- [12] V. F. Petrenko and S. G. Qi, "Reduction of ice adhesion to stainless steel by ice electrolysis", *J. Appl. Phys.* **86** (1999) 5450.
- [13] D. Kuroiwa, "Icing and snow accretion on electric wires", CRREL Res. Report 123,1965.

- [14] R. Cattin, S. Kunz, A. Heimo, R. Oechslin, M. Russi, “An improved approach for the determination of in-cloud icing at wind turbine sites”, Federal Office of Meteorology and Climatology Meteo-Swiss COST Action 727.
- [15] W. D. Macklin, “The density and structure of ice formed by accretion”, *Q. J. Roy. Meteorol. Soc.* **88** (375)(1962)30.
- [16] <http://amsglossary.allenpress.com/glossary/search?icNglaze>: Glaze in the glossary of meteorology.
- [17] F. Kiessling, P. Nefzger, J. F. Nolasco and U. Kaintzyk, “Overhead power lines: planning, design, construction”, Springer 2003.
- [18] C. Ryerson, “Assessment of superstructure ice protection as applied to offshore oil operations safety”, ERDC/CRRELTR-08-14, September 2008.
- [19] E. R. LaChapelle, “Field guide to snow crystals”, Seattle, Wash.: University of Washington Press. (1969) 101.
- [20] N. D. Mulherin, “Atmospheric icing on communication masts in New England”, CRREL Res. Report , **86-17** (1986) 46.
- [21] L. D. Minsk, “Icing on structures”, CRREL Res. Report, **80-31** (1980) 18.
- [22] D. Kuroiwa, “Icing and snow accretion on electric wires”, U.S. Army Cold Regions Research and Engineering Laboratory, Res. Report, **123** (1965) 10.
- [23] H. W. Berndt and W. B. Fowler, “Rime and hoarfrost in upper-slope forests of eastern Washington”, *J. Forest.* **67** (1969) 92.
- [24] S. Baranowski and J. Liebersbach, “The intensity of different kinds of rime on the upper tree line in the Sudety Mountains”, *J. Glaciol.* **19**(1977)489.
- [25] L. Makkonen, “Estimating intensity of atmospheric ice accretion on stationary structures”, *J. Appl. Meteorol.* **20** (1981) 595.
- [26] L. Makkonen and K. Ahti, “The effect of meteorological parameters on rime formation in Finland”, U.S. Army Cold Regions Research and Engineering Laboratory Special Report, **83-17** (1983) 167-174.
- [27] N. N. Khusnatdinov and V. F. Petrenko, “experimental study of ice electrolysis under UV irradiation”, *J. Phys. Chem.* **101** (1997) 6208.
- [28] V.F. Petrenko and C.R. Sullivan, “Methods and systems for removing ice from surfaces,” U.S. Patent 6653598, **2003**.
- [29] I. A. Ryzhkin and V. F. Petrenko. “Physical mechanisms responsible for ice adhesion”. *J. Phys. Chem.* **101** (1997) 6267.

- [30] V. F. Petrenko and R. W. Whitworth, "Physics of ice", Oxford university press, Oxford, 1999.
- [31] V. F. Petrenko and S. Qi, "Reduction of ice adhesion to stainless steel by ice electrolysis", *J. Appl. Phys.* **86** (1999) 10.
- [32] V. F. Petrenko, "Effect of electric fields on adhesion of ice to mercury", *J. Appl. Phys.* **84** (1998) 261.
- [33] N. Dalili, A. Edrisy and R. Carriveau, "A review of surface engineering issues critical to wind turbine performance", *Renewable and Sustainable Energy Reviews.* **13** (2009) 428.
- [34] V. K. Croutch and R. A. Hartley, "Adhesion of ice to coatings and the performance of ice release coatings", *J. Coat. Technol.* **64** (1992) 41.
- [35] M. Amin, M. Akbar and S. Amin, "Hydrophobicity of silicone rubber used for out door insulation", *Rev. Adv. Mater. Sci.* **16** (2007) 10.
- [36] V. K. Croutch and R. A. Hartley, "Adhesion of ice to coatings and the performance of ice release coatings", *J. Coat. Technol.*, **64** (1992) 41.
- [37] A.V. Adamson, "Physical chemistry of surfaces", New York: Wiley; 1990.
- [38] J. N. Israelachvili, "Intermolecular and surface forces", 2nd ed. London: Academic Press; 1992.
- [39] B. Bhushan, "Principles and applications of tribology", New York: Wiley; 1999.
- [40] M. Nosonovsky and B. Bhushan, "Roughness optimization for biomimetic superhydrophobic surfaces", *Microsyst. Technol.* **11** (2005) 49.
- [41] M. Nosonovsky, B. Bhushan, "Multiscale dissipative mechanisms and hierarchical surfaces", friction, super-hydrophobicity, and biomimetics. Heidelberg, Germany: Springer-Verlag; 2008.
- [42] T. S. Lin, C. F. Wu and C. T. Hsieh, "Enhancement of water-repellent performance on functional coating by using the Taguchi method", *Surf. Coat. Technol.* **200** (2006) 5253.
- [43] B. S. Hong, J. H. Han, S. Kim, Y. J. Cho, M. S. Park, T. Dolukhanyan and C. Sung, "Antireflective Silica Thin Films with Super Water Repellence via a Solgel Process", *Thin Solid Films.* **351** (1999) 274.
- [44] B. Bhushan Biomimetics, "lessons from nature—an overview". *Phil. Trans. R. Soc. A.* **367** (2009) 86.

- [45] B. Bhushan, Y. C. Jung and K. Koch, "Micro-, nano- and hierarchical structures for super-hydrophobicity, self-cleaning and low adhesion", *Phil. Trans. R. Soc. A.* **367** (2009) 72.
- [46] K. Koch, B. Bhushan, Y. C. Jung and W. Barthlott, "Fabrication of artificial lotus leaves and significance of hierarchical structure for super-hydrophobicity and low adhesion", *Soft Matter.* **5** (2009) 93.
- [47] C. Neinhuis and W. Barthlott, "Characterization and distribution of water-repellent, self-cleaning plant surfaces", *Ann. Bot.* **79** (1997) 77.
- [48] W. Barthlott and C. Neinhuis, "Purity of the sacred lotus, or escape from contamination in biological surfaces", *Planta.* **202** (1997) 1.
- [49] P. Wagner, R. Furstner, W. Barthlott and C. Neinhuis, "Quantitative assessment to the structural basis of water repellency in natural and technical surfaces", *J. Exp. Bot.* **54** (2003) 303.
- [50] Z. Burton and B. Bhushan, "Surface characterization and adhesion and friction properties of hydrophobic leaf surfaces", *Ultramicroscopy.* **106** (2006) 19.
- [51] B. Bhushan and Y. C. Jung, "Micro and nanoscale characterization of hydrophobic and hydrophilic leaf surface", *Nanotechnology.* **17** (2006) 72.
- [52] K. Koch, B. Bhushan and W. Barthlott, "Diversity of structure, morphology, and wetting of plant surfaces (invited)", *Soft Matter.* **4** (2008) 63.
- [53] K. Koch, B. Bhushan and W. Barthlott, "Multifunctional surface structures of plants: an inspiration for biomimetics (invited)", *Prog. Mater. Sci.* **54** (2009) 78.
- [54] X. F. Gao and L. Jiang, "Biophysics: water-repellent legs of water striders", *Nature.* **432** (2004) 36.
- [55] X. Zhang, F. Shi, J. Niu, Y. Jiang and Z. Wang, "Super-hydrophobic surfaces: from structural control to functional Application", *J. Mater. Chem.* **18** (2008) 621.
- [56] R. N. Wenzel, "resistance of solid Surfaces to wetting by water", *Ind. Eng. Chem.* **28** (1936) 988.
- [57] A. Cassie and S. Baxter, "Wettability of porous surfaces", *Trans. Faraday Soc.*, **40** (1944) 546.
- [58] T. S. Lin, C. F. Wu and C. T. Hsieh, "Enhancement of water-repellent performance on functional coating by using the Taguchi method", *Surf. Coat. Technol.* **200** (2006) 5253.
- [59] R. N. Wenzel, "Resistance of solid surfaces to wetting by water", *Indust. Eng. Chem.* **28** (1936) 94.

- [60] A. Cassie and S. Baxter, "Wettability of porous surfaces", *Trans. Faraday. Soc.* **40** (1944) 51.
- [61] R. E. Johnson and R. H. Dettre, "Contact angle hysteresis", In: Fowkes FM, editor. *Contact angle, wettability, and adhesion. Adv. Chem. Ser., Chem. Soc.* **43** (1964) 35.
- [62] Y. C. Jung and B. Bhushan, "Contact angle, adhesion, and friction properties of micro- and nanopatterned polymers for super-hydrophobicity", *Nanotechnology.* **17** (2006) 80.
- [63] M. Nosonovsky and B. Bhushan, "Patterned non-adhesive surfaces: super-hydrophobicity and wetting regime transitions", *Langmuir* **24** (2008) 33.
- [64] P. G. de Gennes, W. F. Brochard and D. Quéré, "Capillarity and wetting phenomena", Berlin, Springer; 2003.
- [65] S. Shibuichi, T. Onda, N. Satoh and K. Tsujii, "Super water-repellent surfaces resulting from fractal structure", *J. Phys. Chem.* **100** (1996) 19512.
- [66] K. Tadanaga, N. Katata, and T. Minami, "Super-water-repellent Al₂O₃ coating films with high transparency", *J. Am. Ceram. Soc.*, **80** (1997) 1040.
- [67] K. Geunjae, L. Mikyung, S. Karuppanan and Y. Kijung, "Wettability control and water droplet dynamics on SiC-SiO₂ core-shell nanowires", *Langmuir*, **26** (2010) 12273.
- [68] E.A. Cherney, "Silicone rubber dielectrics modified by inorganic fillers for outdoor high voltage insulation applications", *IEEE Trans. Dielect. El. Ins.* **12** (2005) 1108.
- [69] S. Jana, A.S. Khojin, W.H. Zhong, H. Chen, X. Liu and Q. Huo, "Effect of gold nanoparticles and lithium hexafluorophosphate on the electrical conductivity of PMMA", *Solid State Ionics.* **178** (2007) 1180.
- [70] P.C. Ma, B.Z. Tang and J.K. Kim, "Effect of GNT decoration with silver nanoparticles on electrical conductivity of GNT-polymer composites", *Carbon* **46** (2008) 1497.
- [71] S.H. Choi, I.D. Kim, J.M. Hong, K.H. Park and S.G. Oh, "Effect of the dispersibility of BaTiO₃ nanoparticles in BaTiO₃/polyimide composites on the dielectric properties", *Mater Lett.* **61** (2007) 2478.
- [72] Y. Kobayashi, T. Tanase, T. Tabata, T. Miwa and M. Konno, "Fabrication and dielectric properties of the BaTiO₃-polymer nano-composite thin films", *J. Europ. Cer. Soc.* **28** (2008) 117.
- [73] C. Li, Y. Gu, L. Xiaobo, Z. Yaobang and T. Anbing, "Synthesis and dielectric property of polyarylene ether nitriles/titania films", *Thin Solid Films* **515** (2006) 1872.

- [74] F. Su, J. Zhidong, G. Haifeng and G. Zhicheng, "Influence of fillers on silicone rubber for outdoor insulation", Annual report conference on electrical insulation and dielectric phenomena, (2007).
- [75] U. Chatterjee and S.K. Jewrajka, "Synthesis of block copolymer-stabilized Au-Ag alloy nanoparticles and fabrication of poly (methyl methacrylate)/Au-Ag nanocomposite film", *J. Colloid Sci. Interface* **313** (2007) 717.
- [76] L. Luo, Z. Zhang and L. Hou, "Development of a gold nanoparticles based chemiluminescence imaging assay and its application", *Anal. Chim. Acta* **584** (2007) 106.
- [77] W. Y. Liao, Z. C. Guan, L. M. Wang, J. Yang, J. B. Fan, Z. Su and J. Zhou, "Reducing ice accumulation on insulators by applying semiconducting RTV silicone coating", *IEEE Trans. Dielect. El. Ins.* **14** (2007) 1446.
- [78] K. Siderakis and P. Agoris, "Performance of RTV silicone rubber coatings installed in coastal systems", *El. Pow. Syst. Res.* **78** (2008) 248.
- [79] S. Rastegar and Z. Ranjbar, "DC and AC electrical conductivity of electro-deposited carbon-black-epoxy composite films", *Prog. Org. Coat.* **63** (2008) 1.
- [80] M. Kermani, "Ice shedding from cables and conductors - A cracking model of atmospheric ice", Ph.D. thesis, UQAC, 2007.
- [81] C. Laforte and A. Beisswenger, "Icephobic material centrifuge adhesion test", *Proceedings of the International Workshop on Atmospheric Icing of Structures (IWAIS XI)*, Montréal, (2005) 357.
- [82] L.E. Kollar and M. Farzaneh, "Wind-tunnel Investigation of icing of an inclined cylinder", *Int. J. Heat. Mass. Tran.*, **53** (2010) 849.
- [83] L. Kollar and M. Farzaneh, "Spray Characteristics of Artificial Aerosol Clouds in a Low-Speed Icing Wind Tunnel", *Atomization Spray*, **19** (2009) 389.
- [84] L. Kollar, M. Farzaneh and A. Karev, "Modeling Droplet-Size Distribution near a Nozzle Outlet in an Icing Wind Tunnel", *Atomization Spray*, **16** (2006) 673.
- [85] S. Noormohammed, "Nanostructured Thin Films for Icephobic Applications", Ph.D. thesis, UQAC, 2009.
- [86] http://www.engineeringtoolbox.com/thermal-conductivity-d_429.html
- [87] <http://asm.matweb.com/search/SpecificMaterial.asp?bassnum=MA6061t6>
- [88] <http://www.dowcorning.com/applications/search/products/details.aspx>

- [89] P. E. Khizhnyak, A. V. Chechetkin and A. P. Glybin, “ Thermal conductivity of carbon black” , J. Eng. Phys. Thermophys. **37** (1979) 1073.
- [90] T. Maekawa, K. Kurosaki, T. Tanaka and S. Yamanaka, “Thermal conductivity of titanium dioxide films grown by metal-organic chemical vapor deposition”, Surf.Coat.Technol. **202** (2008) 3067.
- [91] M. Mogensena , N. M. Sammesb, G. A. Tompsett, Y. Z. T. Cheng, Q. Hu, Z. Fang and K. Han, “Physical, chemical and electrochemical properties of pure and doped ceria”, Solid State Ionics. **129** (2000) 63.